Design and Optimization of Microwave Ablation Tools and Techniques

by

Jason Chiang

A dissertation submitted in partial fulfillment of
the requirements for the degree of

Doctor of Philosophy

(Biomedical Engineering)

at the

UNIVERSITY OF WISCONSIN–MADISON

2014

Date of final oral examination: 05/15/2014

The dissertation is approved by the following members of the Final Oral Committee:

Christopher L. Brace, Assistant Professor, Biomedical Engineering
James L. Hinshaw, Associate Professor, Radiology
Tomy Varghese, Professor, Medical Physics
Willis Tompkins, Professor, Biomedical Engineering
Deane Mosher, Professor, Biomolecular Chemistry

To my loving parents, thank you for always believing in me. Words cannot express my gratitude.

ACKNOWLEDGMENTS

From the beginning of graduate school, I have been honored to be given the opportunity to work with **Chris Brace, PhD**. Despite his obvious professional accomplishments, he has remained approachable and continues to exude a welcoming personality. His open-door policy has been the most important resource I have enjoyed during my time in graduate school. A true academic at heart, he has encouraged me to pursue exploratory projects that may not have been immediately applicable to my current research projects. Above all else, Chris has always had the unique capability of leading discussions on any topic, from coaching grade-school soccer to the role of Snuggle House on world economic policy. His role in my personal and professional development has easily gone above and beyond that of a graduate student advisor.

Throughout my graduate school years, I have received a tremendous amount of help with my experimental studies. **Lisa Sampson's** presence was usually the common link that made a study come to fruition. She performed much of the background preparation to ensure an animal study would be successful, from the ordering of the supplies to the anesthesia of the animals to the organization of the scanning time. It is likely that I spent more time with Lisa than any other individual in our lab. She was critical to the success of my own experimental studies and to a large extent, the successful execution of all the projects related to Tumor Ablation Lab itself. Without a doubt, she is the glue that holds the lab together as it has transitioned from its humble origins on a portable cart to the dominating presence in the WIMR 1 hallway. I'd like to thank **Bridgett Willey** for her invaluable help in ultrasound imaging and her assistance in helping develop my ultrasound imaging skills. **Alejandro Munoz del Rio, PhD** provided valuable insight into the statistical

work related to my thesis. Despite coming to him exclusively for statistical help, our conversations usually started and ended with updates on our competitive road racing results. **Alice Minx**, who runs the CT studies, was very helpful in assisting with CT protocols, no matter how ambitious or silly they appear. Lisa, Bridgett, Alice and Alejandro have invaluably contributed to my experience in WIMR.

On the clinical side, I have been fortunate to work with **Fred Lee, MD, Louis Hinshaw MD, Tim Ziemlewicz, MD and Meg Lubner, MD**. Their clinical work translated much of my laboratory and computational studies to have clinical implications. In addition, their presence at conferences and lab meetings added a unique dimension to our work that has played a major competitive advantage when submitting publications and applying for research grants. Most importantly, the team-like atmosphere they nurtured in the ablation clinic carried over into the ablation laboratories and encouraged a collaborative atmosphere across a variety of projects.

I have had the pleasure of working many students over the years. Within the ablation lab, the contributions of graduate students **Mariajose Bedoya, Po-Hung Wu¸ Dong Liu** and **Alex Johnson** have pushed the frontiers of ablation research forward. Although our projects did not overlap, their insight in group meetings and laboratory projects have directly influenced my own projects. There have been multiple undergraduate and visiting graduate students who have brought their energy and unique skills into our lab, in particular **Kieran Hynes, Colin Harari, Billy Greisch, Jeff Wu, Michelle Magagna, and Luke Juckett**. Additionally, I'd like to thank post-doctoral researchers **Peng Wang and Zheng Ji**, who had assisted in many of the technical aspects of ablation. Their assistance in getting me started during my first two years of graduate school was critical in developing my research skills.

Outside of our lab, there have been multiple individuals who have allowed me to bounce ideas off of them before making critical decisions. Plasma physicist **Jim Reardon, PhD** of the Department of Physiccs, when not coaching me through the Wisconsin Track Club, was always available to assist me in looking at research problems from a more intuitive standpoint. Within our MD/PhD program, my colleagues **Brendan Floyd** and **Farshid Moussavi-Harami** provided valuable feedback and insight, generously donating countless hours to keeping me grounded in reality. Their guidance has been remarkably refreshing and I have always looked forward to conversing with them.

I'd like to express my gratitude toward my research collaborators **Joshua Martin** and **Randy Kimple, MD, PhD** in the Department of Oncology, who generously provided assistance with wet lab protocols and equipment when we decided to pursue exploratory studies in our vessel studies. I was truly humbled by their knowledge and technical expertise each time I stepped into their lab. I'd like to thank my preliminary and defense committee, which includes **Tomy Vargheese, PhD, Deane Mosher, MD, Louis Hinshaw, MD, Willis Tompkins, PhD and Chris Brace, PhD**.

Most of all, I'd like to thank my parents for their support. Originally from Taiwan, they had worked tirelessly to scrounge up the resources needed to immigrate to the United States. Once arrived, they never stopped putting in extra hours at work to ensure that my brother and I had every resource available to excel in our educational endeavors. Despite not living under their roof for over a decade, their interest and enthusiasm toward my education has not been diminished, as evidenced by their requests for NIH-styled monthly progress reports.

I would not be where I am today without their sacrifice.

CONTENTS

LIST OF TABLES

LIST OF FIGURES

DESIGN AND OPTIMIZATION OF MICROWAVE ABLATION TOOLS AND TECHNIQUES

Jason Chiang

Under the supervision of Professor Christopher L. Brace
At the University of Wisconsin-Madison

Thermal ablation is a minimally-invasive procedure that is used as an alternative to surgical resection in treating early-stage solid tumors. Due to its percutaneous route of administration, thermal ablations have been shown to be associated with less bleeding, fewer complications and quicker recovery compared to surgery. While radiofrequency ablation (RFA) is currently the most common heating modality used for ablation, microwave ablations have rapidly gained traction in academic centers in recent years due to its improved heating physics. Microwave offers substantial benefits over radiofrequency ablation through faster heat generation, leading to larger and more homogenous ablation zones in highly-perfused tissue. These qualities can lead to better margins during tumor ablation and a smaller chance for tumor recurrence.

Controlling the high power and temperatures associated with microwave has remained a formidable barrier toward widespread clinical adoption. The tools used in microwave ablation, especially the antenna itself, require modification in order to decrease shaft heating. The physics of microwave heating, which now incorporate water vaporization, needs to be accounted for in the tissue heating process. Lastly, the role of hotter ablation zones in thrombosing larger blood vessels is becoming a growing concern for physicians.

By leveraging advances in computational modeling and validation techniques, more accurate models of microwave ablation zones can be created. These models offer unique insight into safer antenna designs and improved intra-operative place-

ment of microwave antennas in the vicinity of larger blood vessels. This information gives physicians a more precise view of how an ablation zone forms in a clinial setting, providing valuable insight that can optimize patient outcome. The outline of this dissertation is as follows:

Chapter 1 reviews the background on hepatocellular carcinoma and colorectal metastasis to the liver, comprising the majority of malignancies where thermal ablations are warranted. This chapter also compares patient outcomes between surgery and ablation and the current controversies behind thermal ablations today, specifically with microwave ablation systems.

Chapter 2 outlines the basics of computational modeling of microwave ablations. Included in this discussion are recent advances in coupling water and temperature information to input variables associated with thermal and electrical properties of liver tissue. Special emphasis is given into the current trends and future works in validating these increasingly accurate computational models.

Chapter 3 describes the design of a novel dual-slot antenna that incorporates a cooling component and ceramic heating element to the overall antenna design. Eliminating backwards heating along the shaft of the microwave antenna prevents accidental thermal damage to delicate anatomy near the antenna insertion track. This microwave antenna is capable of minimizing backwards heating while maintaining energy delivery efficiency.

Chapter 4 describes the validation of a novel dual-slot antenna capable of minimizing backwards heating while maintaining energy delivery efficiency. The validation studies were performed in ex-vivo and in-vivo liver models and underwent intra-procedural CT imaging.

Chapter 5 discusses the computational modeling and model validation of heat transfer of a microwave antenna in the vicinity of a phantom vessel. A 3D computational

model is presented and demonstrates the role of velocity in heat accumulation during microwave ablation. Experimental measurements of temperature-dependent blood viscosity was performed to predict the change in blood velocity during a microwave ablation procedure.

Chapter 6 is an extension of Chapter 5, where thrombus formation during a microwave ablation zone is correlated with vessel size, vessel blood velocity and vessel-antenna spacing. The study was performed in an in-vivo porcine liver model and utilized ultrasound to visualize the thrombus formation. Uni-variate and multivariate predictors were correlated to the risk for thrombus formation using logistic functions.

Chapter 7 investigates the role of heat transfer in thrombosis and vascular damage in an in-vivo model of the liver. Heat transfer was evaluated during microwave ablation by placing fiber-optic temperature and pressure sensors inside larger hepatic vasculatures. This study was augmented by a study looking at the gene expression profile of thrombotic proteins associated with the individual hepatic vessels.

Chapter 8 explores the potential of using single-energy and dual-energy computed tomography (CT) to observe changes in tissue water content. Phase decomposition with regards to liquid water and vaporized water was also investigated under dual-energy CT.

Chapter 9 outlines about the numerical modeling and validation of water vapor formation and movement inside a homogenized liver solution during a microwave ablation. The water vapor in this study was tracked under intra-procedural CT imaging and compared with the modeling results. Temperature points in this porous media model were also experimentally validated in the homogenized liver solution.

Chapter 10 summarizes the contributions of this dissertation and future direction

on the field of thermal ablations. Strategies and potential resources required to carry out future work will be addressed.

Chapter 1

Liver Malignancies and Current Trends in Microwave Ablation Research

This introductory chapter is divided into three sections. The first section will provide background information about current trends in hepatocellular carcinoma and secondary hepatic malignancies, including incidence, risks, staging tools and treatment options. The second section will focus on how the advantages of thermal ablation became an attractive alternative to surgical resection, with a brief comparison between the two curative treatments based on clinical trials. From there, a presentation will be given on the drawbacks of conventional ablation systems in clinical practice that led to the rapid rise of microwave ablation systems. Lastly, the current weaknesses and gaps in knowledge of microwave ablation system design and implementation will be addressed.

1.1 Hepatocellular Carcinoma

Hepatocellular carcinoma is the third leading cause of cancer-related deaths worldwide, with more than 700,000 new cases diagnosed each year and approximately 600,000 deaths [1]. The majority of the disease burden is found in developing countries such as Southeast Asia and sub-Saharan Africa, where there is widespread incidence of the hepatitis B virus (HBV). In the United States, where the incidence the hepatitis C virus (HCV) has become the leading cause of cancer-related death in the last 20 years, the incidence of HCC has tripled, with over 20,000 new cases each year **(Figure 1.1)**[2].

Worldwide, there are some notable trends with regards to the incidence of HCC. In Asian countries such as China and Korea, there has been a decreasing rate of HCC incidence, potentially due to the increase rates of HBV vaccination along with preventive measures against aflatoxin. In contrast, the developing world has actually experienced an increase in HCC incidence due to young adults being

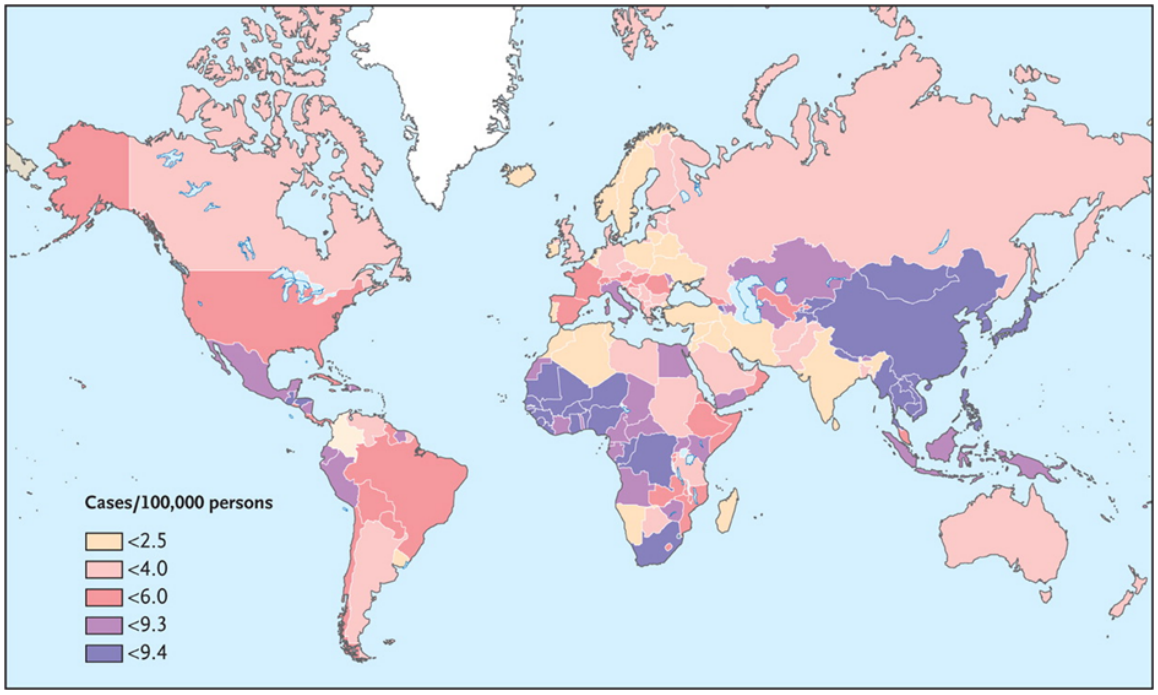

Figure 1.1: Epidemiology of HCC. Hepatocellular carcinoma rates have been jumped over the last two decades due to increasing rates of hepatitis B and C. *Adapted from El-Serag HB. N Engl J Med 2011;365:1118-1127*

infected though IV drug use and blood transfusions in the 1960s and 1970s [3]. A rising epidemic of obesity, diabetes and non-alcoholic steatohepatitis (NASH) in these countries has also played a contributory role towards this increasing incidence of HCC. Diabetes is an independent risk factor for HCC and mortality rates are up to 5 times higher in obese patients [2].

1.1.1 Risk Factors

The most widespread risk factor worldwide for hepatocellular carcinoma is chronic HBV infection, which accounts for greater than 50% of all HCC cases [4]. Hepatitis B is a DNA virus that is most commonly spread perinatally, but can also be passed on percutaneously and sexually. While only affecting approximately 1.25 million

people in the United States, the disease burden numbers 350-400 million worldwide [2]. The relative risk of HCC is about 100 times higher in HBV carriers versus non-carriers and is even higher in those with concurrent cirrhosis [5]. Chronic HBV infections account for nearly 50% of all HCC cases worldwide and nearly all cases involving children. In sub-Saharan Africa and parts of Asia, HBV is transmitted from mother to newborn, with 90% of the cases developing into chronic infections. Nearly 70% of HCC patients with latent HBV infections have cirrhosis [2].

The risk for HCC is 15-20 times higher in those with HCV, mostly focused among those with later stage HCV infections associated with cirrhosis and subsequent fibrosis [6]. Biomarkers of HCV are found in up to 30% of HCC patients in the United States and reaching up to 60% in Italy and 90% in Japan [2]. These numbers are expected to rise in the next century, as blood transfusions and intravenous drug use, which account for nearly 70% of all chronic HCV infections in developed countries, continue to grow. Meanwhile, in less industrialized countries, HCV infections are primarily caused by non-sterile surgical procedures.

The remainder of HCC patients does not have chronic infection of HBV or HCV, and are more likely to suffer from non-alcoholic fatty liver disease (NAFLD) as a result of obesity, diabetes mellitus type 2 or metabolic syndrome [7]. The key process in NAFLD that links patients to HCC is the development of non-alcoholic steatohepatitis (NASH), which is diagnosed with biopsy showing evidence of steatosis and hepatocellular injury such as ballooning, Mallory bodies and fibrosis.

1.1.2 Staging

While there are multiple staging systems for HCC, the most commonly used one is the Barcelona Clinic Liver Cancer (BCLC) guideline, which also provides framework that links tumor stage, cirrhosis stage and functional performance status to a

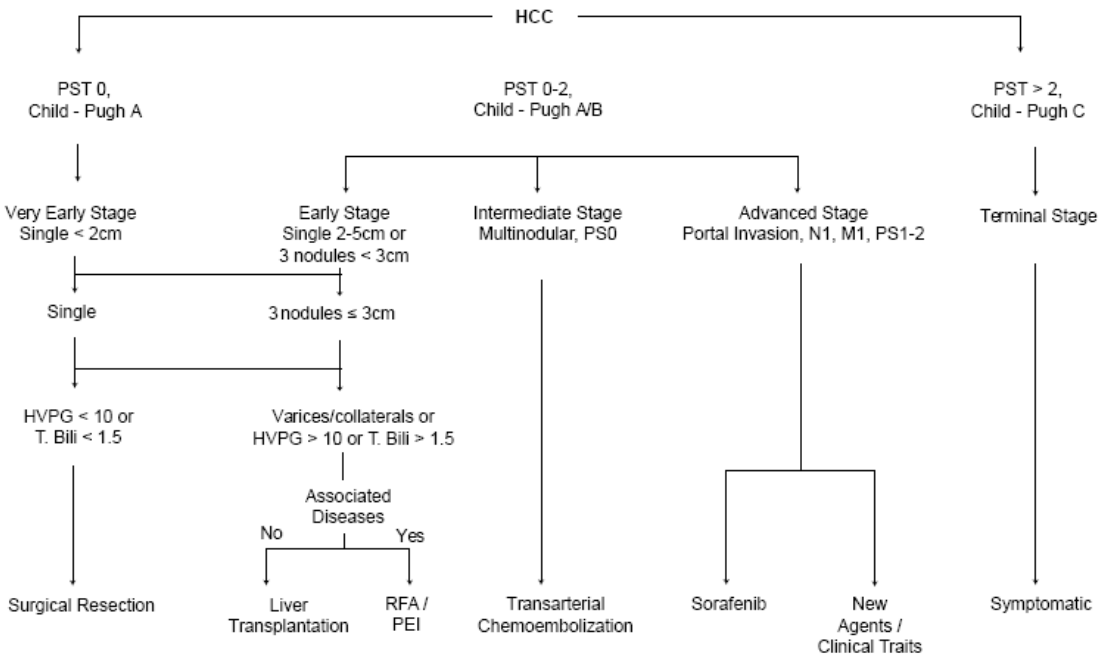

Figure 1.2: The BCLC Criteria provides a framework that links tumor stage, size, cirrhosis progression and liver function to a treatment algorithm.

treatment algorithm **(Figure 1.2)**. This staging system has been endorsed by both American and European societies and has been independently and validated in European and American cohorts. The BCLC guideline identifies several stages of HCC, each which is associated with a different prognosis and recommendations are given based on the impact of treatment on survival.

Very early stage HCC (stage 0) offers the best prognosis but is also the most difficult to diagnose, with patients presenting with a single lesion smaller than 2 cm in diameter. Patients presenting with this stage has stable cirrhosis (Child-Pugh class A) and no evidence of vascular invasion from the tumor. Patients with early-stage HCC (Stage A) have either a solitary lesion or up to three lesions that are each smaller than 3 cm in diameter. These patients also have preserved liver function (Child-Pugh class A or B) and a reasonable functional status (PS 0-2). Patients with

stage A HCC can expect a 5-year survival rate of 50-75% with a wide variety of treatment options, depending on the presence or absence of portal hypertension, the degree of liver dysfunction and other co-morbidities. Intermediate stage HCC (Stage B) presents with multi-nodular HCC but these patients continue to demonstrate preserved liver function (Child-Pugh class A or B) with good functional status (PS 0) and have no cancer-related symptoms or evidence of vascular invasion. Trans-arterial therapy has been shown to confer a survival benefit to patients with stage B HCC. Advanced stage HCC patients show vascular invasion or extrahepatic spread (Stage C). These patients have compromised functional status (PS 1 or 2) due to HCC and receive some survival benefit from targeted treatments such as sorafenib. Patients with terminal stage HCC (stage D) presents with decompensated cirrhosis (Child-Pugh class C), poor functional status (PS>2) and advanced tumor growth characterized by vascular invasion or extrahepatic spread. Treatment options are limited and used symptomatically.

1.1.3 Current Treatment Options

The BCLC system recommends multiple therapies for HCCs but the treatment choices depend on the stage of HCC, the degree of underlying liver function, medical comorbidities and the availability of treatment modality and local clinical expertise. These final decisions are usually made by a tumor board consisting of hepatologists, surgeons, diagnostic and interventional radiologists, oncologists and pathologists.

Surgical Resection

Surgical resection is the gold standard treatment for patients with very early-stage HCC absent of cirrhosis. In the presence of cirrhosis, resection produces better results when the tumor is small, there is no portal hypertension and the total

bilirubin level is normal [8]. The 5-year risk of recurrence of HCC after resection has been shown to be as high as 70% due to underlying chronic liver disease. However, in the United States, less than 5% of the patients are candidates for surgical resection [2]. Resection is typically more common in Asian countries where there are larger numbers of HBV-related HCC with minimal cirrhosis [1].

Liver Transplantation

For patients with underlying cirrhosis, liver transplantation is the treatment option of choice due to its associated decrease in risk of tumor recurrence. This is the only treatment that has a dramatic effect on chronic liver disease, one of the largest contributors to HCC progression [9]. However, due to the scarcity of organs available for transplant, strict criteria are used to ensure transplant patients have optimal outcomes.

Local Ablation

Local ablation is the best alternative treatment of patients with early-stage HCCs who are not eligible for surgical resection or transplantation. Radiofrequency ablation has historically been the most commonly used modality of local ablation therapy, although it has been rapidly being replaced with microwave ablation in recent years. To date there has been only three randomized control trials, demonstrating near-efficacy in both 5 year overall survival rates and recurrence rates compared to surgical resection [10]. Results from these studies will be discussed in section 1.3.1. A major advantage of thermal ablation is their significantly decreased risk of complications and hospitalization, leading to quicker recoveries and virtually no blood loss [11].

Radio- and Chemo-embolization

Trans-catheter arterial chemoembolization (TACE) and radioembolization has been demonstrated to improve survival among patients with preserved liver function, particularly those with Child-Pugh class A cirrhosis without metastasis, vascular invasion or cancer-related comorbidities [12]. TACE can also be used as a neoadjuvant therapy or as a way to downstage a patient's condition before liver transplantation [13]. In recent studies, the use of drug-eluting beads, which release drugs in a controlled manner in conjunction with TACE has been shown to reduce hepatic and systemic side effects while directly affecting tumor growth rates [14]. Yttrium-90 is a novel microsphere recently developed and used as a palliative treatment for Child-Pugh class A cirrhosis and intermediate-stage HCC [15].

Targeted Therapy

One recent development that has been adopted into clinical practice has been the usage of Sorafenib, a small-molecule multi-kinase inhibitor that is administered orally and exhibits anti-proliferative and anti-angiogenic properties. In recent RCTs, it has been shown to increase overall survival of 37% (2-3 months of life) as compared to placebo, in patients with advanced HCC and compensated cirrhosis [8]. Success with sorafenib has led to studies evaluating its use in combination therapy with other treatments during various stages of HCC progression.

1.2 Secondary Liver Malignancies

While hepatocellular carcinoma is the most common cause of primary liver malignancies, a large portion of patients undergoing the treatment options referenced in the previous section suffer from secondary liver malignancies. Due to the liver's rich

blood supply, secondary liver malignancies often arise from metastasis of breast, lung, esophagus, skin, pancreas and stomach tumors. One of the more significant contributors of secondary liver malignancies is colorectal cancer, the 3rd most common cancer in males and 2nd most commonly diagnosed cancer in females. In 2013, there were over 100,000 new cases of colon cancers and over 50,000 deaths (colon and rectal cancers combined) in the United States [16]. Worldwide, there are approximately 1.2 million new cases diagnosed each year and 600,000 deaths. The most common site of metastasis is the liver, of which 50% of patients suffer from [2]. Surgical resection is often considered the only curative treatment for patients with colorectal metastasis with resectable liver with no sign of extrahepatic disease [17]. Palliative therapy of colorectal metastasis has increased from 8% using passive chemotherapy to 25-40% used combination therapy of surgical resection and chemotherapy [18-20]. As with HCCs, liver resection of colorectal metastasis is possible in only 15% of the cases due to the location, size and number of liver metastasis, as well as the amount of healthy liver and extrahepatic disease [21]. Primary surgery alone is associated with a high rate of recurrence and has led to renewed interest in adjuvant therapy with chemotherapy [22].

1.3 Thermal Ablation Background

Liver transplantation is considered to be the only option that can treat the liver malignancies, but organ shortage limits the availability of this procedure. In patients without chronic liver disease, surgical resection is an excellent option. However, this case only appears in 5% of HCC cases in Western countries [1]. More often than not, the chronic liver disease or cirrhosis often associated with HCC can decrease the benefits of surgical resection and even make the patient ineligible for surgery. For this

reason, minimally invasive treatments such as percutaneous thermal ablations have been gaining traction among specialties that manage and treat HCCs and colorectal metastasis. In ablation procedures, an applicator is inserted percutaneously into the tumor region under the guidance of ultrasound or CT imaging. The applicator delivers heat-based energy into the tumor until cytotoxic temperatures are reached. Since there are no incisions, tumor ablation is an attractive option for those who are not eligible for surgery and patients experience quicker recoveries with less complications. Furthermore, patients who undergo ablation are able to maintain the majority of their liver function after the procedure [23].

1.3.1 Comparing Surgical Resection and Radiofrequency Ablation

Observational and meta-studies in the past have compared clinical outcomes between RFA and resection. RFA has attracted great interest because of its effectiveness in treating unresectable HCCs up to 5 cm in a single treatment session. In fact, overall survival rates and recurrence rates in treating early-stage HCC have started approaching that of surgical resection as RFA technology continues to improve [24,25]. Taking into consideration the fewer complications and maintenance of liver function after RFA, many ablation centers has begun using RFA procedures over surgical resection for early stage liver cancer.

There have been past literature reviews on comparing resection to RFA, mostly from outside of the United States, where there are higher incidences of hepatitis and HCCs. To date, there have only been three randomized controlled studies (RCTs) that have looked at differences in outcomes between surgical resection and ablation [26-28]. A brief meta-analysis (6 retrospective studies and 3 RCTs) looking at whether RFA provided equivalent outcomes to surgical resection in patients with

Childs-Pugh A/B early-stage HCC revealed the following information on overall survival, recurrence-free survival and complication rates [26-32].

There was no significant difference in overall survival at 1-year between RFA and resection [OR, 0.73(95% CI, 0.48-1.11); p=0.14]. However, patients undergoing RFA had a significantly smaller survival rate at 3-years compared to those undergoing surgical resection [OR, 0.47(95% CI, 0.31-0.72); p=0.0004]. The 5-year overall survival results showed similar trends, with patients undergoing RFA experiencing a significantly smaller survival rate at 5-years compared to those undergoing surgical resection [OR, 0.60(95% CI, 0.43-0.84); p=0.003].

In terms of recurrence-free survival, patients undergoing RFA had a significantly worsened survival rate at 1-year compared to those undergoing surgical resection [OR, 0.66(95% CI, 0.48-0.90); p=0.008]. At three years, patients undergoing RFA had a significantly worsened survival rate compared to those undergoing surgical resection [OR, 0.34(95% CI, 0.23-0.50); p=0.00001]. Similarly, at 5-years, patients undergoing RFA had a significantly worsened survival rate at compared to those undergoing surgical resection [OR, 0.47(95% CI, 0.34-0.67); p=0.0001]. In regards to complication rates, patients undergoing surgical resections had significantly more complications compared to those undergoing RFA [OR, 4.65(95% CI, 1.59-13.56); p=0.005].

There was strong statistical evidence showing that in early stage HCC with Childs-Pugh A/B, RFA is equivalent to resection in terms of 1-yr overall survival while resection lead to superior survival rates at later time points. Recurrence-free survival was significantly better in patients undergoing resection versus ablation at all time points. The lower rates of complications associated with RFA compared to those of resection is widely supported by both RCTs and cohort studies. RFA as a percutaneous procedure inherently predisposes the patient to less risk of infection

and bleeding than open surgery. Surgical resection puts the patient at risk for hepatic failure, bile leakage, refractory ascites and encapsulated effusion. RFA has risks such as hepatic infarction and malignant seeding, but occur at a smaller rate than the complications associated with surgery. For these reasons, RFA continues to be the primary treatment option for patients not eligible for surgery.

Drawbacks of Thermal Ablations

As mentioned in the previous section, clinical studies have reported slightly higher rates of recurrence with patients undergoing thermal ablation compared to surgical resection [26-28]. One potential reason for this effect is that thermal ablations are highly susceptible to the cooling effect of nearby blood vessels. Blood vessels tend to act as a cooling element, siphoning heat away from the ablation zone and changing the growth rate and shape of the final ablation zone. Many times, this can lead to incomplete treatment of the tumor, especially if the tumor is located near larger vasculature.

One way physicians have tried to combat this is to utilize higher powers, multiple probes and insertion of conducting fluid. These techniques can lead to higher temperatures and more homogenous heating, but have critical drawbacks. With radiofrequency ablation devices, higher power often leads to charring near the center of the ablation zone. Desiccated and charred tissue drives the impedance of the tissue upwards, preventing propagation of the electrical current. The rise in impedance is also a hurdle when performing ablations in heavily-aerated environments such as the lung. This self-limiting process often leads to smaller ablation zones and incomplete tissue heating near tumors, increasing the risk for recurrence. A solution that has been adapted into clinical practice is the insertion of ionic fluids, which can improve the conduction of electrical current into the tissue. One difficulty with

this solution is controlling the spread of the fluid inside the tissue, which is highly susceptible to gravitational effects. The current can flow to undesirable locations inside an organ and cause unnecessary damage to nearby organs. Utilizing multiple radiofrequency probes has also been presented as a solution, but has also been shown to run into the tissue charring impedance issue. Furthermore, multiple probes are not always feasible depending on the location of the tumor and whether or not they are located near more sensitive anatomy. Without a consistent solution to address these technical difficulties, there is a clear need for an improved method of heating tissue.

1.3.2 The Rise of Microwave Ablation Systems

The concept of using microwave tissue heating technology to heat biological tissue has existed for several decades, primarily with interstitial antennas and arrays for adjuvant hyperthermia and prostate cancer. It has only been in recent years that there has been newfound interest in using it for early-stage solid tumor. Microwave ablations utilize a process called dielectric heating, which uses an alternating electric field. Water molecules, which have its own dipole moment, will align itself to this electric field, which is changing directions at a specific frequency, usually between 300 MHz and 300 GHz. While the water molecules attempt to align itself to this rapidly changing electric field, the rotational movement generates heat within the tissue. The electric field associated with microwave ablations can penetrate a variety of tissue conditions, including desiccated and charred tissue. Microwave energy can continuously heat tissue throughout the duration of a procedure, resulting in larger, more homogenous ablation zones, even in the vicinity of larger vessels.

1.4 Current Hurdles associated with Microwave Ablation Systems

While there are clear benefits in using microwave energy versus radiofrequency or other predecessor technologies, there are also drawbacks to using such high-powered devices. The wavelength of a 2.45 GHz electromagnetic source inside liver is about 2-4 cm, depending on the temperature and water content. At these macroscopic levels, the precision of the heating zone can be fairly limited compared to more focused energy sources such as laser. Furthermore, the temperature of the heating zone can greatly exceed that of RF or laser, capable of exceeding 150 deg C. The rapid growth of these temperature levels are difficult to control in a limited area and require a level of supervision that may go beyond what is available in a clinic, such as temperature probes or MRI thermometry.

The next three sections of this subsection will outline some of the major issues that have affected the adoption and utilization of microwave technologies. The presentation and solutions to these issues will be the major themes of the thesis herein.

1.4.1 Antenna Design Issues

While the theoretical potential of microwave ablation has generated significant enthusiasm in the interventional oncology community, not all systems have met expectations. A microwave ablation system is composed of a generator, distributor and delivery components, all which require a level of optimization for clinically-acceptable performance in a hospital environment.

The generator, made up of solid-state devices or vacuum tubes such as a magnetron, produces the microwave power, which is then distributed through a flexible

coaxial cable. The delivery component of the system, the microwave antenna, consists of a rigid shaft and a radiating element where microwave energy is delivered. The antenna performance is evaluated based on its radiation pattern and reflected energy. In most cases, lower reflected energy translates to more energy forwarded into the tissue environment, indicative of more efficient antenna performance. In contrast, an antenna with a high reflected energy will have less energy delivered to tissue and more being sent back along the antenna shaft and coaxial cable. In some cases, ablation treatment times need to be shortened in order to prevent antenna damage from excess backwards heating [33].

One evaluation study used the Valleylab Evident 915 MHz microwave ablation system to perform 45 W ablations on renal cell carcinomas (RCCs) in a cohort of 10 patients [34]. The patients had tumors ranging from 2.0-5.5 cm in diameter with 50% of the tumors involving the collecting duct system. Within this cohort, there were 2 perioperative complications, including one hematoma from a patient taking anticoagulative therapy and one capsular tear that was resolved with Surgicel. Additionally, there were 9 post-operative complications found in 4 separate patients, including a case of urinoma that required exploratory laparoscopy, drain placement uretal stenting and nephrostomy tube placement. One other notable post-operative complication was a retained foreign body in the kidney, which was later found to be the needle sheath of the microwave antenna, which had melted during the procedure. The area around the needle sheath was necrosed from the excess heat generated around the shaft of the antenna and required laparoscopic nephrectomy to remove. On top of these complications, 38% of the patients experienced recurrence on follow-up, found between 3 and 21 months. The poor clinical outcomes, coupled with the 20% intra-operative and 40% post-operative complication rate was considered unacceptable and led to the stoppage of utilizing microwave ablation technology.

They attributed the high rate of complication to treating larger tumors, necessitating larger power delivery that led to poor control of the heating area. Furthermore, the large power delivery (45 W) led to excess heating along the antenna that resulted in the melting of the needle sheath.

Another clinical study showed poor microwave ablation performance in treating lung cancers [35]. The group used the Valleylab Vivawave Microwave Coagulation System, which delivered up to 60 W through a 14.5 gauge needle. There was a 39% (26/66) rate of pneumothorax, where 69% (18/26) of them were classified as mild and did not require chest tube placement. In the remaining eight, the pneumothorax was considered moderate to severe and required chest tube placement. In two patients, there was presence of intraprocedural skin burns. One skin burn was classified as a full-thickness 3 cm by 3 cm third degree burn superficial to the ablated tumor, requiring plastic surgery consult. The other patient was found to have a 2-cm second-degree burn that required topical treatments and home dressing changes. Post-ablation body-wall burns were also reported, requiring pain medications. The authors reported that the larger gauge of the microwave antennas coupled with the multiple antenna insertion sites made it difficult to prevent pneumothrorax complications in the more superficial tumors.

It is clear that simply using microwave ablation systems to treat tumors does not immediately translate to better outcomes. The antenna design, which is critical in delivering power efficiently into tissue based on its electrical properties, has space for significant improvement. From an engineering and usability standpoint, the final antenna design is a balance between energy delivery efficiency, ablation size and invasiveness. Improper antenna design can lead to a large percentage of reflected energy, resulting in excess heating along the shaft of the antenna. The shaft of the antenna is usually in direct contact with the organ and preceding anatomical parts

superficial to the tumor. Poorly designed antennas can lead to spikes of reflected power, causing unnecessary damage to body walls that lead to pneumothorax or pleural effusions, as seen in previous microwave studies.

There is an unmet need for a better microwave antenna that can deliver energy more efficiently into the tissue and actively prevent backwards heating. Localizing the heating zone to the antenna heating zone can lead to fewer complications and less risk for device breakdown during treatment. To this end, the optimization process and testing of a cooled microwave antenna that can reduce ablation zone length will be presented in Chapters 3 and 4.

1.4.2 Microwave Ablations near Blood Vessels

Microwave ablation has become a more attractive option over RFA for larger tumors that may be closer to nearby blood vessels because of their decreased susceptibility to the heat sink effect. This refers to the phenomena where nearby blood vessels draw away heat from the ablation zone, decreasing the efficacy of the thermal ablation. In a situation where there is already difficulty in heating around a tumor environment, depending on size, location, equipment and technique, this cooling effect can lead to incomplete ablations, leading to a higher rate of tumor recurrence. In recent years, there have been anecdotal reports of microwave ablations not only overcoming the heat-sink effect, but going so far as to damage nearby vessels themselves and causing both vascular and peri-vascular damage. These complications can be devastating for a patient with underlying liver disease such as cirrhosis and already suffering from decreased liver reserves. Unfortunately, there have been relatively few studies on predicting the affects of thermal ablation, both in RFA or microwave, on blood vessels.

The risk of thrombus formation during RFA had previously been correlated to

the size of the vessels in an in-vivo porcine liver model [36]. The research group concluded that hepatic vessels larger than 3 mm generally stayed patent during an ablation and could contribute to the heat-sink effect. Conversely, vessels smaller than 3 mm occluded at a much higher rate and thus did not interfere with the size and shape of the ablation zone. The same group performed a similar study with microwave ablations, with the implication that the higher heating rate would be overcome the heat sink effect and occlude even the larger vessels [37]. That component was validated, as larger vessels were shown to shown to be less susceptible to the heat-sink effect with microwave ablation compared to similar-sized vessels near RFA. There was a positive link established between the rate of occlusion and the size of vessel, with smaller vessels being occlude at a higher rate compared to larger vessels. However, the relationship between size and occlusion rate was not as clear-cut as the previous RFA study.

Recently, a more detailed relationship between hepatic vessel flow and its associated heat-sink effect in the vicinity of both RFA and microwave [38]. Performed in an ex-vivo perfusion model, he found that RF was susceptible to the heat sink effect, with the size of the ablation zone negatively correlated with increasing blood velocity. Thus, a slow flowing vessel would not siphon a lot of heat from the ablation zone, leaving the original ablation unchanged, but a fast flowing vessel would siphon a lot of heat from the ablation zone, significantly decreasing the size of the ablation. An ablation zone created from microwave ablation system, however, was not correlated with changes in velocity. Higher flow rates did not change the relative shape and size of a microwave ablation zone, suggesting that microwave was capable of overcoming the heat-sink effect.

The primary issue of ablating near vessels is the current lack of insight in how a blood vessel will respond to thermal ablations. Excessive vessel heating beyond

the appropriate margins of a tumor can lead to unnecessary destruction of healthy tissue and potential injury to delicate nearby anatomy such as biliary structures, diaphragms and bowels [39]. These complications require pain medication at the very least but can require surgical intervention if not detected in time. On the other side of the coin, an arguably more important danger is the risk of incompletely ablating the tumor and its associated vasculatures, which would be considered a technical failure in tumor control. This case would require immediate re-treatment. The inconsistency in how ablation zones form with respect to vessels of different physical parameters such as type, size and velocity, makes the complete treatment of solid tumors unpredictable, requiring extensive operator experience and real-time imaging resources to confirm tumor destruction.

1.4.3 Limited Validation Techniques

Numerical simulation of thermal ablation research has been an active area of research because of its potential to use computer-aided design to improve ablation systems and treatment planning. Computer simulation has been especially useful in recent years with modeling microwave ablation zones in a variety of tissue environment and antenna designs that may not be easily done experimentally. The computational nature of numerical simulations provides a highly-controlled environment to observe and delve into the effects of changing individual parameters associated with the ablation environment. These specific studies can lead to more efficient experimental studies, leading to fewer animals used and decreased laboratory costs. As a natural extension to these techniques, it is also possible to leverage computational modeling to improve microwave ablation procedures in a more patient-specific model.

But despite the rapid adoption of microwave ablation systems into the hospital

workflow and its success in replacing RFA in ablation clinics worldwide, there have been relatively few advances in translating the many computational research discoveries into clinical practice. One of the biggest hurdles in translating in-silico results into the clinic is the lack of experimental validation of these computational models. The most common validation technique for verifying antenna performance is visual inspection of an ablation zone in ex-vivo or in-vivo tissue. Areas that are blanched and desiccated inside the ablation zone are representative of cell death and can be correlated geometrically to a computationally-derived heating zone [40,41]. Other ways to evaluate cell death is to look apply histological techniques to separate different regions of cell death. A potential method of evaluating a numerical model outputting a temperature map in an ex-vivo, in-vivo and even clinical scenario is to use discrete temperature probes either utilizing thermocouples or fiber-optic material to measure temperature changes around the ablation zone. Temperature changes can be correlated with computational models to test the accuracy of the model [42].

There are significant strengths and weaknesses to each of the currently-accepted validation techniques. Using visual inspection gives excellent spatial resolution, as it is relatively straightforward to look for the boundary of the blanched region and identify the charred interior region next to the antenna. Histological analysis allows for a snapshot of specific cell processes are occurring at specific regions around the ablation zone. However, access to the tissue sample can only occur after the completion of the ablation zone. Thus, the time-dependent heating changes within the ablation zone is never captured and cannot be correlated with the time-dependent computational data. With the visual inspection, we are only getting a single snapshot of entire ablation process. A model may match up well with the beginning of the microwave ablation inside tissue but fall apart when temperatures exceed 100 deg C

and water vaporization phenomenon dominates. Conversely, the model might not match up with the experimental setup in the beginning but then correlate well at the single time point when the ablation zone is cut open, leading investigators to believe that the model is an excellent fit. Using individual temperature probes provides the reverse problem. Temperature probes give excellent temporal resolution to thermal information. However, we can insert a few temperature probes into an ablation zone at once, giving us only limited spatial information. To compound this problem, temperature sensors are not physically locked into place, making them sensitive to motion artifacts associated with tissue contraction. Temperature probes that started 1 cm away from the antenna may potentially end up only 0.5 cm away from the antenna toward the end of a 5 minute ablation. This spatial variability makes the accurate correlation of entire temperature maps to a single point very difficult.

The current state of computational model validation is not optimal for translational studies due to these limitations. Improving validation methods will be critical in confirming the efficacy of existing computational ablation models and assisting in the physicians' decision-making process. Treatment planning with the assistance of computational models would be helpful in letting physicians recognize how to create ablations with necessary margins while avoiding critical structures and associated complications.

Chapter 2

Computational Modeling of Microwave Tumor Ablations

2.1 Abstract

Microwave tissue heating is being increasingly utilized in several medical applications, including focal tumour ablation, cardiac ablation, hemostasis and resection assistance. Computational modeling of microwave ablations is a precise and repeatable technique that can assist with microwave system design, treatment planning and procedural analysis. Advances in coupling temperature and water content to electrical and thermal properties, along with tissue contraction, have led to increasingly accurate computational models. Developments in experimental validation have led to broader acceptability and applicability of these newer models. This chapter will review the basic theory, current trends and touch on the future direction of computational modeling of microwave ablations.

2.2 Introduction

Thermal ablation technology is a rapidly emerging alternative to surgical resection for many benign and malignant tumors of the liver, lung, kidney and bone [43-45]. Ablation is also being investigated for the treatment of other solid tumors in organs such as the breast, prostate, adrenal glands, pancreas and uterus [46-50]. Non-oncologic applications include treatment of cardiac arrhythmia, as well as a means for hemostasis during surgical resection [51,52]. Ablation may also be combined with adjuvant therapies such as radiation, chemotherapy and even nanoparticles to improve treatment efficacy [53-55].

Methods of inducing thermal ablation include lasers, high-intensity focused ultrasound, radiofrequency electrical current and microwaves. The applied energy heats the target tissue to cytotoxic temperatures, usually above 50-60°C, although microwave can heat tissue to over 150°C [56]. Due to its minimally-invasive nature,

thermal ablation is characterized by quicker recoveries and fewer complications compared to surgical resection [57]. Microwave ablation is gaining attention as an alternative to the more widely disseminated radiofrequency ablation, due to several advantages in tissue-heating physics. Microwave energy is capable of propagating through desiccated and charred tissue, which allows for continuous and rapid volumetric heating, potentially leading to a larger ablation zone compared to radiofrequency ablation [56]. The high heating rate produced by some microwave systems can overcome heat-sink effects from nearby vessels, creating more uniform ablation zones [38]. Microwave antennas can also be tuned to deliver energy more efficiently to specific organ systems such as the liver or lung [58,59].

Computational modeling of microwave ablation procedures plays a critical role in the development and implementation of clinical systems. Numerical simulations can rapidly predict the propagation of electromagnetic (EM) waves from antennas of arbitrary geometry and evaluate antenna performance metrics [59]. Energy deposition from the applied electromagnetic fields, heat generation, as well as the subsequent water and vapor mass transfer in tissue can then be used to predict the thermal dose or surviving fraction of cells [60]. Together, coupled electromagnetic-thermal solutions may improve predictions of how ablation zones form inside patients.

The in-silico nature of computational modeling of thermal ablations provides a highly-controlled environment to investigate and understand the effects of changing input variables [61]. Such specific insights can potentially lead to more focused experimental studies, fewer animal studies, decreased developmental costs and greater research efficiency. Faster and more powerful computational techniques can help predict and improve microwave heating in patient-specific models. Analysis of antenna geometry and materials can also be used to optimize device design and

implementation.

2.3 Theory

Microwave ablation is produced by EM fields radiating from an antenna inserted into the tissue. The EM field is described most generally by the source-free, time-harmonic form of Maxwell's equation in lossy media such as tissue:

$$\nabla \times \mathbf{E} = -j\omega\mu\mathbf{H} \tag{2.1}$$

$$\nabla \times \mathbf{H} = J + j\omega\epsilon\mathbf{E} \tag{2.2}$$

$$\nabla \cdot \mathbf{D} = 0 \tag{2.3}$$

$$\nabla \cdot \mathbf{E} = 0 \tag{2.4}$$

where **E** is the electric field intensity (V/m), **H** is the magnetic field intensity (A/m), ω is the angular frequency, μ is the permeability (H/m) and ϵ is the complex permittivity or dielectric constant (F/m), **B** is the magnetic flux density (Wb/m^2), **D** is the electric flux density (C/m^2), and **J** is the current density (A/m^2). In the case of coaxial microwave antennas in an approximately homogenous, isotropic medium, an axially-symmetric cylindrical coordinate system can often be used to reduce the three-dimensional problem to a two-dimensional domain, accelerating the solution computation.

A description of heat transfer in tissues can be realized using Pennes' formulation of the non-stationary heat equation [62]:

$$\rho C_\rho \frac{\partial T}{\partial t} = \nabla \cdot (k_t \nabla T) + Q_h + Q_p + Q_m \quad [W/m^3] \tag{2.5}$$

where C_ρ is the specific heat capacity of the tissue $(J/kg{\cdot}K)$, k_t is the thermal conductivity $(W/m{\cdot}K)$, T is the temperature (K). Q_m is the metabolic heat generated from the tissue (W/m^3) but usually ignored due to its minimal impact compared to the other heat terms. Q_p represents heat loss through blood perfusion,

$$Q_\rho = \omega_{bl} c_{bl} (T - T_{bl}) \quad [W/m^3] \tag{2.6}$$

where ω_b is the blood perfusion velocity $(kg/m^3{\cdot}s)$,c_{bl} is the specific heat capacity of blood $(J/kg{\cdot}K)$andT_{bl} is the blood temperature (K). The remaining term of equation (6) is the heat absorbed by the electromagnetic field into the tissue,

$$Q_h = \frac{\sigma}{2} \parallel \mathbf{E} \parallel^2 \quad [W/m^3] \tag{2.7}$$

where **E** is the electric field (V/m) solution found previously through solving Maxwell's equations, and σ is the tissue conductivity (S/m) [56]. Solving this set of equations provides a visual representation for how tissue temperature changes during a microwave ablation procedure (**Figure 2.1**). The equations can also be solved simultaneously or iteratively to account for changing tissue properties; for example, those that are dependent on temperature or water content.

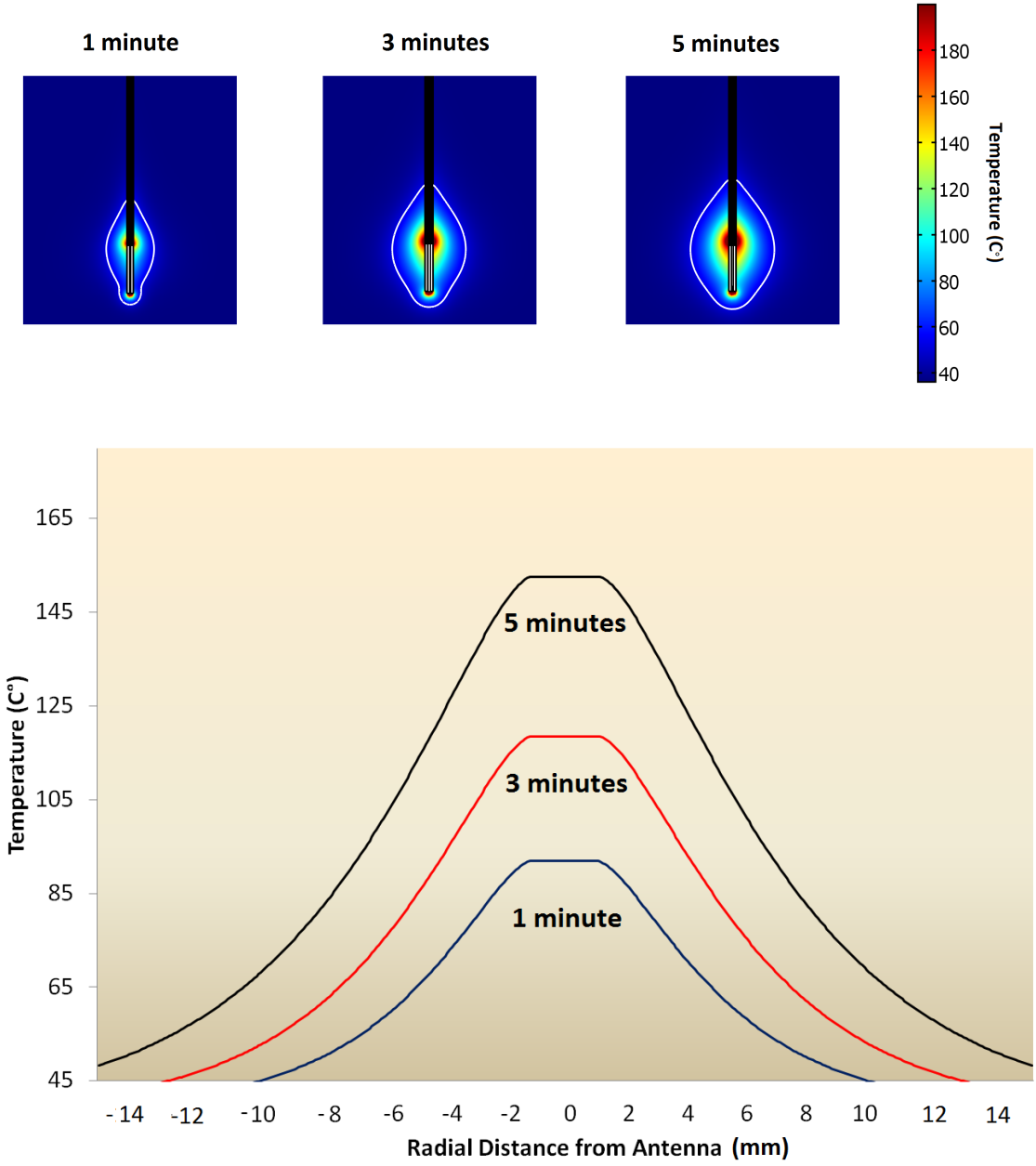

Figure 2.1: (Top) Numerical model of temperature profiles during microwave ablations in liver tissue at various time points. The ablation zone temperature boundary grows more in the first 3 min, compared to the last 2 minutes. (Bottom)Temperature elevation through the transverse cross section of ablation zone at various time points. Microwave ablation zones can reach temperatures as high as 150°C.

Although tissue damage is composed of many complex biological processes, there are two widely-accepted models that predict thermal damage as a single simplified process: the thermal iso-effective model and the Arrhenius damage model [63,64]. The thermal iso-effective model describes how cellular damage is related to cumulative thermal dose; that is, the relationship between temperature and exposure time. The cumulative equivalent minutes at 43°C (CEM43) is a common metric that equates the likelihood of cellular death to that of cells exposed to 43°C for a specified number of minutes [65]. The Arrhenius damage model, using similar assumptions as the CEM model, expresses the percentage of cells in a given volume that will survive at a given temperature and exposure time. However, there are limits in quantifying thermal damage, especially at the higher temperatures seen in thermal ablations compared to mild or moderate hyperthermia [63,66]. Models that describe thermal damage due to cellular or metabolic disruption have also been described but have not been as widely-utilized to date due to complex inputs and high computational costs [67,68].

Analytical solutions to equations 2.1-2.7 are available for only certain antenna geometries and assumptions about the medium, such as a homogenous tissue environment. For more general models, numerical methods are required. The most commonly-used techniques include the finite element method (FEM), the finite difference time domain method (FDTD) and the method of moments (MOM). The finite-element method has been used extensively due to its availability in commercial software such as COMSOL and ANSYS, which are capable of coupling electromagnetic field solutions to other physics models such as heat transfer and diffusion.

2.4 Use of Computational Modeling in Microwave Ablation

2.4.1 Antenna Evaluation

Common microwave ablation antenna performance metrics include those that describe how efficiently an antenna can deliver power into the tissue and the resulting heating pattern. Antenna efficiency can be described by the ratio of power output to power input, or reflection coefficient Γ,

$$\Gamma(f)_dB = 10 \cdot \log(\frac{Pr(f)}{P_{in}}) \tag{2.8}$$

where $Pr(f)$ is the reflected power and P_in is the input power (W). More efficient power delivery is characterized by lower reflection coefficients. Specific absorption rate (SAR), which represents the rate of power deposition in tissue, is given as

$$SAR = \frac{\sigma}{2\rho} \parallel \mathbf{E} \parallel \quad [W/kg] \tag{2.9}$$

where **E** is the electric field (V/m), σ is the tissue conductivity (S/m) and ρ is the liver tissue density (kg/m^3) (35,25). SAR can roughly estimate potential shape of an ablation zone created by a given antenna **(Figure 2.2)**.

With transient analysis of coupled EM-thermal problems, it is also possible to observe the changes in reflection coefficient and SAR occurring during the ablation process. Using these metrics, automated optimization techniques can be employed to find microwave antenna geometries that suit a specific clinical need. Due to the multiple factors involved in antenna design, the final design is usually the result of a trade-off between the objective heating pattern and reflection coefficient. Improving ablation antenna design remains an area of active research [59,69-74].

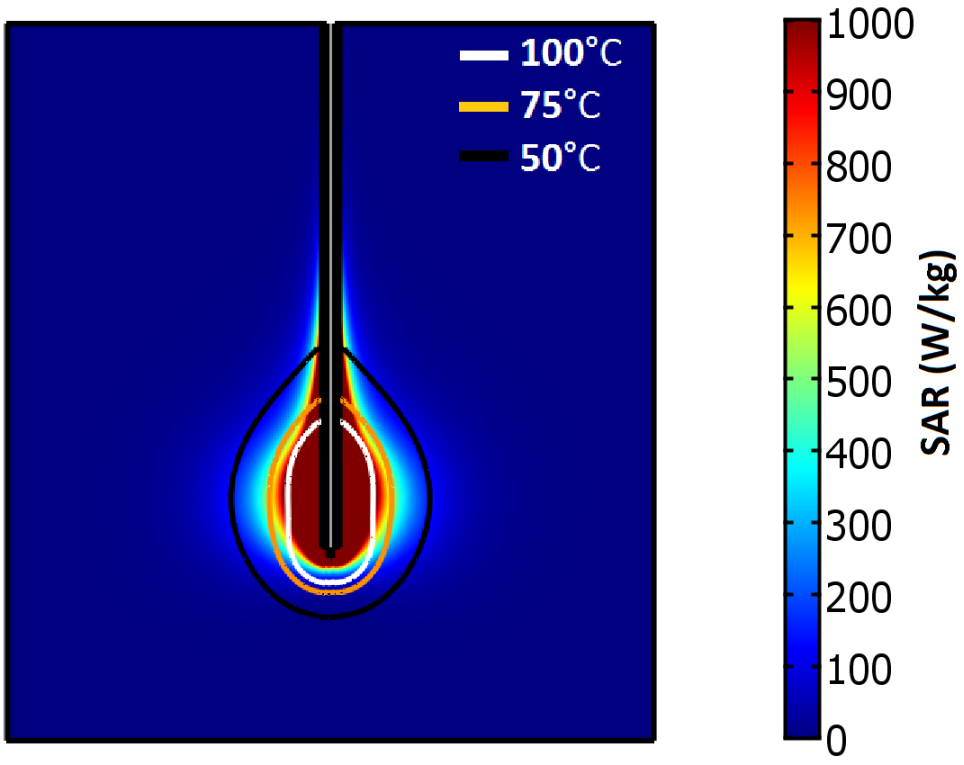

Figure 2.2: SAR mapping of a microwave ablation zone along with corresponding temperature isotherms at 5 min

2.4.2 Power Delivery Frequencies

In addition to facilitating computer-aided antenna design, computational modeling can also be used to evaluate the effect of the applied frequency during power delivery. Current microwave ablation generators provide continuous power, from 30 to 180 W at 915 MHz or 2.45 GHz, although higher and lower frequencies have been described [75-79]. While some previous studies suggested that lower frequencies are associated with greater penetration depth and larger ablation zones, power

output was not normalized to offset cable losses at each frequency [80,81]. When modeling the dipole antennas used in those studies, and controlling for applied power, we found virtually no difference in ablation SAR diameter between 915 MHz and 2.45 GHz **(Figure 2.3)**. This result confirmed the conclusions of an earlier microwave hyperthermia antenna study [82]. When comparing antenna designs in a controlled environment with varying powers, computational modeling can play a critical role.

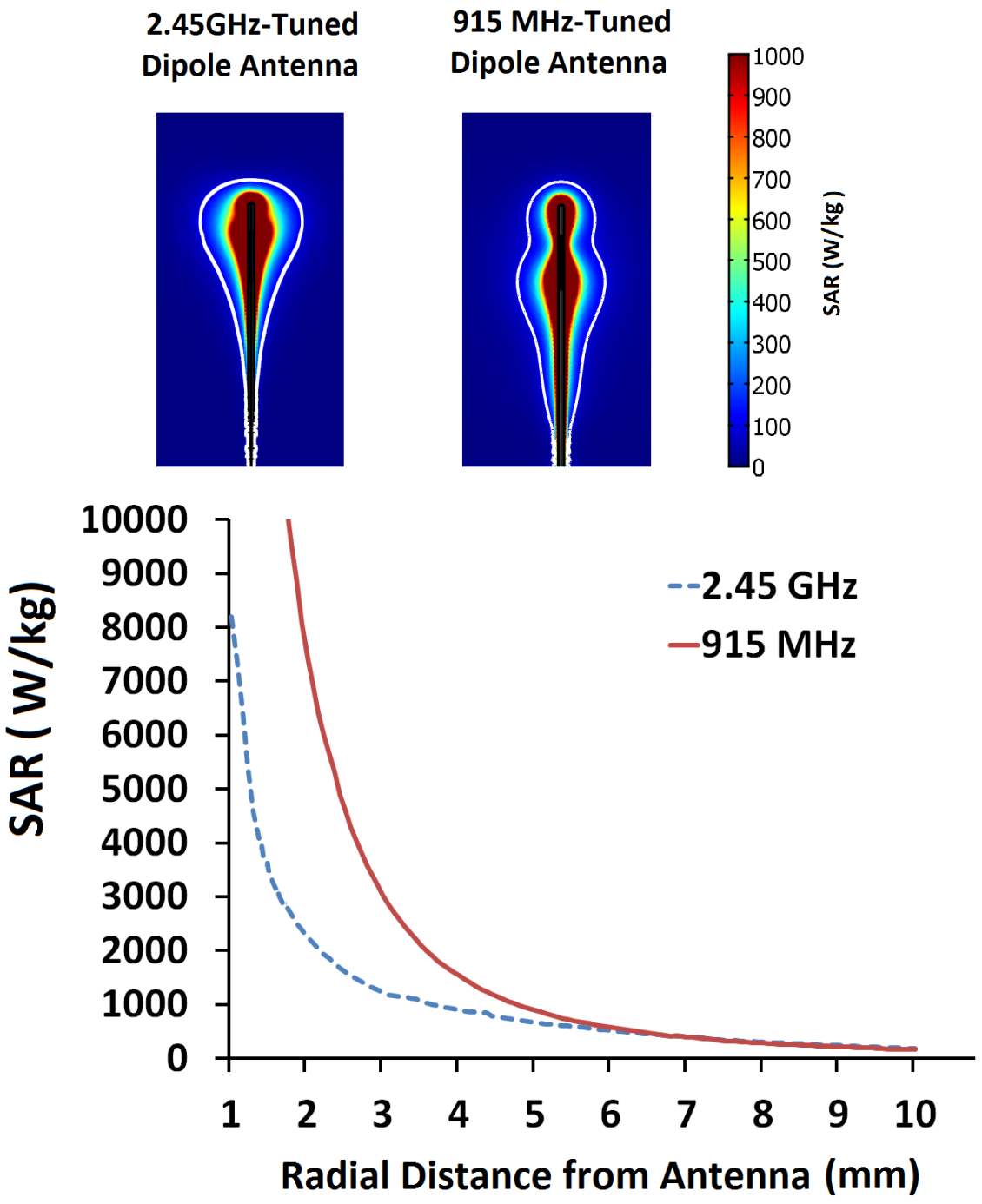

Figure 2.3: (Top) Numerical modeling demonstrating nearly equivalent maximum ablation zone diameters between dipole antenna designs emitting power at 2.45 GHz (right) and 915 MHz (left). The color bars represent the heating rate from 0–1000 W/kg. The white line iso-contour gives a visual approximation to the ablation heating zone. (Bottom) Microwave antenna performance at the two frequencies shows nearly equivalent SARs at radial distances 7 mm from the antenna

2.4.3 Multiple Antenna Optimization

Modeling has also been utilized to analyze and optimize antenna arrays for microwave tissue heating. Such arrays can produce larger, more homogenous ablation zones than with a single antenna [82-87]. As with single antennas, computational models can predict the electromagnetic interactions between antennas and resulting heating pattern in tissue. Zones of constructive and destructive wave interference that can affect relative heating rates have been of particular interest. Computational modeling can help optimize the input wave amplitude and phase to produce deeper tissue penetration and improved local control of the tumor ablation zone [88-90]. Temporal modulation of the amplitude and phase of each antenna has also been analyzed during computational modeling [91,92]. Placement of phased antennas in non-parallel fashion while maintaining the same homogenous ablation zone has also been explored [93]. Array optimization with modeling has led to increased efficacy in treating more irregularly-shaped tumors that are deep within the body and provide more options in the number of antennas placed and their insertion points [94-97].

2.4.4 Tissue Property Changes during Thermal Ablation

Dielectric properties of various tissues are strongly influenced by temperatures and tissue water content [98]. The dielectric properties of tissue include relative permittivity ϵ_r, which describes the tissue's ability to hold electrical charge, and effective conductivity σ, a measure of how well the tissue absorbs electromagnetic energy. The dielectric properties of biological tissue can be described across a wide frequency domain by the multi-pole Cole-Cole dispersion model:

$$\epsilon(\omega) = \epsilon_\infty + \sum_{n=0}^{\infty} \frac{\Delta\epsilon_n}{1 + (j\omega\tau_n)^{(1-\alpha_n)}} + \frac{\sigma_s}{j\omega\epsilon_0} \tag{2.10}$$

where τ is a time constant to characterize the polarization in a relaxation region, ϵ_∞ is the permittivity at field frequencies where $\omega\tau >> 1$, $\Delta\epsilon$ is the magnitude of dispersion, α is a measure of the broadening of the dispersion and σ_s is the static conductivity [99].

The temperature-dependence of dielectric permittivity and conductivity in tissue has been documented in multiple studies. Within a narrow range around physiological temperatures (20-45°C), temperature-dependence can be reasonably described as a linear function [100,101]. Parabolic temperature-dependent models have also been described in the range of 20-60°C [102]. Microwave ablation systems, however, are capable of heating tissue to temperatures well over 100°C [103]. At these higher temperatures, tissues undergo structural changes and water loss, which affect tissue properties substantially [104,105]. By lumping physical phenomena such as water vaporization and tissue dehydration into a temperature-dependent model and using coupled EM thermal simulations, more accurate temperature profiles can be predicted, even at temperatures over 100°C. One study compiled a table of dielectric properties of tissue which were measured at the end of a microwave ablation with various sets of power and time. The results were fitted to a Cole-Cole model and suggested significant changes in the amount of dispersion, time constant and static conductivity values during heating [106]. Two other studies monitored the dielectric property values during high temperature microwave heating of ex vivo bovine liver, revealing a sigmoidal relationship between permittivity and conductivity with temperature [107,108]. These curves were then applied to the computer simulations and found to be more accurate in predicting experimental temperatures when compared to existing models. The temperature-dependent model also more

accurately described changes in antenna reflection coefficient and heating pattern caused by non-uniform changes in the tissue dielectric property during ablation. Establishing the relationship between dielectric properties and heating physics is an ongoing topic of research that holds promise for even more accurate simulations.

2.5 Trends in Microwave Ablation Modeling

Microwave ablation technology development has undergone rapid growth in the last decade and there are multiple areas of active research that leverage the benefits of numerical modeling. The effect of individual parameters on the entire ablation process can be predicted prior to experimental work, saving time and resources for more focused study [109]. But despite the advantages of working with simulations and leveraging nearly a century of research in electromagnetic theory, there is much work needed with regards to the inputs and the validation of existing numerical models.

2.5.1 Water Vaporization and Tissue Contraction in Tissue

Intense heating during microwave ablation leads to physical changes such as water vaporization, vapor mass diffusion and re-condensation. This is evident during experimental studies with microwave antennas in tissue, where vapor formation can be observed with imaging during longer and more powerful ablations. The center of the ablation zone typically becomes dehydrated first, and the water is driven outwards from the antenna. Vapor formation and transport leads to dehydration of the tissue around the ablation zone [65,103-105,110]. Two separate groups tried improving matching between modeling and experimental results by incorporating a latent heat of vaporization term to account for the energy needed to change water

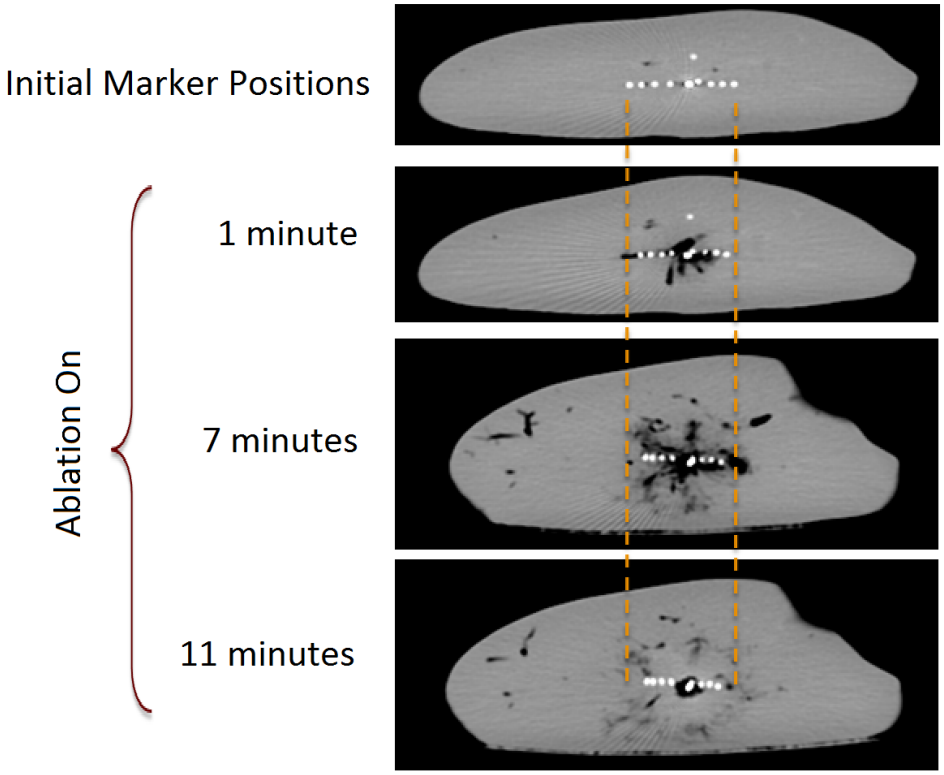

Figure 2.4: Ex vivo tissue contraction is shown by placing pairs of high density wire markers 10–40 mm away from the antenna shaft. The original marker positions are shown in the top image and begin to move closer together as the microwave ablation begins and continues shrinking until the end of the procedure.

from its liquid to gas phase within tissue [103,111]. However, there was an unaccounted decrease in heating rate after 100°C and a high temperature SAR correction term was required to match the model to the experiments. One possible explanation for this model mismatch is a change in the EM field profile secondary to changes in permittivity and conductivity as noted in other works [104, 107]. Incorporating the dielectric changes due to tissue dehydration in the ablation treatment may yield a more accurate model to predict the physical changes occurring during an ablation treatment.

Another important phenomenon affecting the accuracy of computational modeling is the contraction of tissue exposed to ablative temperatures. One previous study had demonstrated that ablation zones contract up to 15-50% in diameter and 27-75% in volume during radiofrequency and microwave ablation. The same study implemented an exponential correction term to the computational model to compensate for the 20-25% radial contraction at various distances from the antenna after 5 minutes [112]. Greater contraction was noted during microwave ablations than RF ablations, likely due to increased water vaporization and collagen dehydration **(Figure 2.4)**. Contraction can complicate the validation of numerical and experimental results because temperature sensors placed into the tissue will move during contraction, artificially increasing temperatures compared to static points in a computational model. Contraction can also confound imaging-based diagnostic and post-ablation staging efforts by shrinking the original boundaries of the tumor. Accurate comparison of numerical simulations and experimental results is possible only by accounting for such contractions.

2.5.2 Model Validation

Experimental validation of computational model predictions is critical to establish broader applicability of the model. Visual inspection and correlation of experimental ablation zone dimensions to numerical predictions is one validation technique. Blanching and desiccation inside the ablation zone are good predictors of cell death in many parenchymal tissues such as the liver **(Figure 2.5)**. Further histological analysis such as microscopic examination, enzyme histochemistry and transmission electron microscopic analysis can help stratify various regions of ablation [40,113,114]. These techniques compare cell death to the predictors of cytotoxicity calculated during simulation. However, such comparisons rely on the numerical

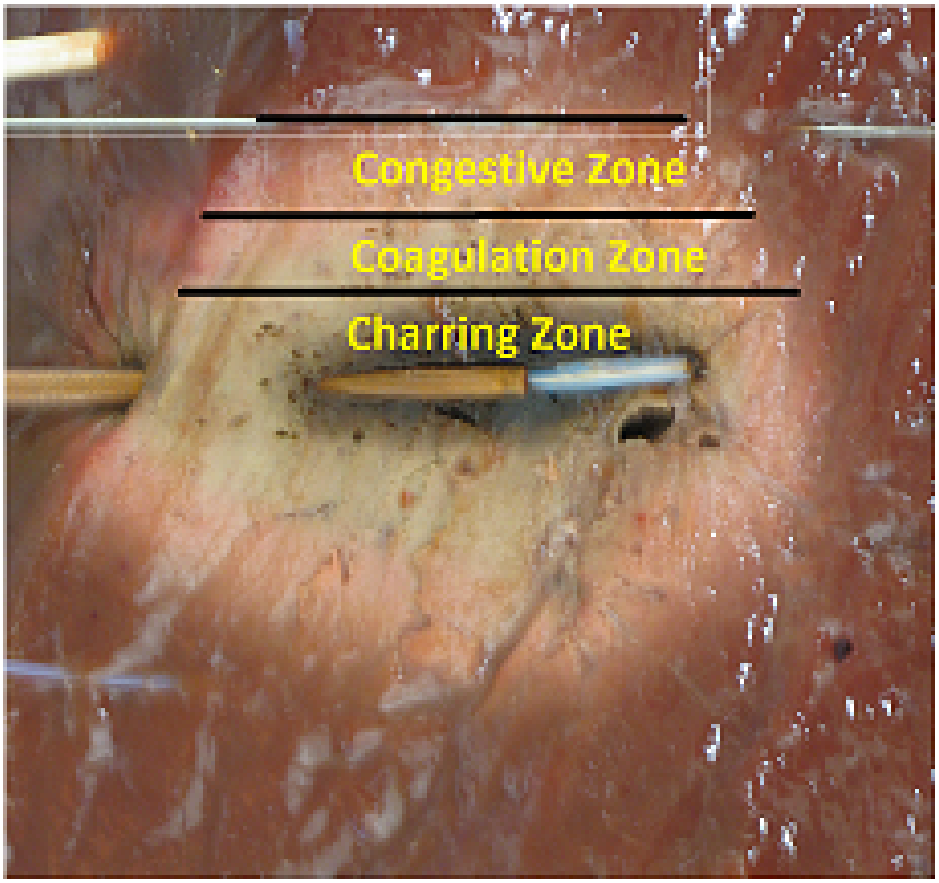

Figure 2.5: Microwave ablation zone created in ex vivo liver tissue. The charred zone is the darkened area at the center of the ablation zone which was highly desiccated from the intense heat and water vaporization (greater than 100°C). The coagulation zone is the blanched region of the ablation zone, usually showing pyknotic nuclei on histology (70–100°C). The congestive zone is the red peripheral area of the ablation zone that represents the boundary of the ablation zone and is sometimes called the transition zone (50–70°C).

metric of cell death, which can vary widely by method [63].

Alternatively, arrays of thermocouples or fiber-optic temperature probes have

been successfully used to map temperatures around the ablation antenna [107]. These temperature probes are structurally robust, exhibit quick response times and provide enough temporal resolution in real-time. Temperature data can be recorded and correlated spatially and temporally with the modeling data. Since contraction can change the location of the temperature probes, it is important to similarly recalibrate the evaluation points in the simulation output or establish a temperature-contraction relationship in the model to accurately compare numerical and experimental results [107,112].

Imaging techniques such as ultrasound, CT or MRI can also be used to validate computational models [115-117]. Contrast-enhanced scans delineate boundaries of the coagulation zone compared to perfused tissues and can be used to compare ablation zone size to predicted sizes [116]. Non-contrast scans with sufficient temporal resolution can be used to monitor ablation zone growth, but thermal ablation features can still be difficult to discern. One more prominent feature is water vapor formation, which appears as hyper-echoic gas bubbles under ultrasound and hypodense regions under CT. The visible gas is not a surrogate for the ablation zone, but can provide an estimate of the most desiccated zone of tissue. The highly visible gas can also be tracked during the ablation to estimate vapor transport (**Figure 2.6**). However, water vapor formation and transport must be calculated in the computational model to use gas as the validation metric. Alternatively, MR thermometry can be used to quantify the temperature change in tissue experimentally for comparison with numerical predictions, but most studies have been targeted toward radiofrequency ablation measurements [118-120]. Current microwave devices are not MR compatible so the utility of MR thermometry has been limited [121, 122].

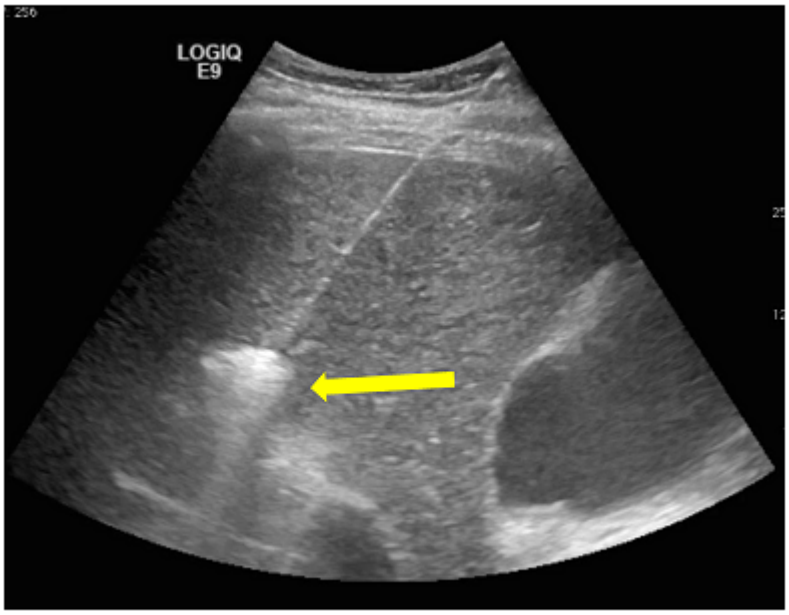

Figure 2.6: Gas bubbles resulting from water vaporisation are visible on ultrasound imaging and can be used to monitor treatment progress.

2.5.3 Extension to Patient-Specific Planning

Treatment planning is most typically performed by the attending physician and is, therefore, heavily dependent on physician experience. Patient-specific treatment planning based on computational modeling may be able to assist in the physicians' decision-making process. Ablation precision would theoretically improve as physicians would be able to recognize whether a given antenna placement could achieve the necessary margins, but also potentially avoid critical structures that could lead to procedural complications [123]. While information needed to create patient-specific antenna guidance systems is available, there are still multiple challenges that need to be addressed before being integrated into hospital workflow. Cooling effects from vasculature can disrupt the growth of a thermal ablation zone, decreasing

the efficacy of an ablation treatment and increasing the risk for local recurrence. Previous literature investigating the effect of blood vessels on thermal ablations are based primarily on radiofrequency ablation [124-126]. Studies relating the effects of blood vessels and vascular trees to radiofrequency ablation zone sizes have revealed additional flow mechanics that influence how a thermal ablation zone may appear [127-130]. While the focus of these studies were on radiofrequency ablation, the implications are increasingly relevant for microwave ablations, which are much more efficient at heating tissue and blood vessels. Vessels near microwave ablations have been shown to act as a heat conduit, as opposed to a "heat-sink" for thrombotic events and perivascular damage [123, 131, 132]. Understanding the effect of vessel flow and nearby vascular beds in thermal ablations is currently an area of active research.

In addition to the modeling of local anatomy near the antenna placement location, patient-specific planning requires detailed knowledge of many other parameters such as the thermal and electrical properties of the organ and surrounding tissue that may be affected by underlying disease processes [133, 134]. Accurately integrating these additional facets into clinically useful information in the hospital workflow in real-time has led to the development of ranking algorithms, image registration and computing reduction techniques. Optimization algorithms have been used to rank the possible insertion points and find the best antenna placement location, maximizing chances of the best clinical outcome and minimizing risks for complications [135-137]. To cut down on computing costs, some groups have utilized an objective cost function that optimizes the temperature distribution by avoiding larger vasculatures, creating an optimal trajectory of an RFA applicator [125]. Decreasing the computational time of calculating ablation zone behavior near major vasculatures has also been demonstrated using patient-independent

lookup tables. These tables utilized previously-calculated cooling rates of blood vessels based on vessel size and distance from an RF applicator. Using these tables to predict ablation zone characteristics was demonstrated to be computationally faster than solving for the electromagnetic and heat transfer solutions independently for a patient-specific anatomy [125]. Other efforts to improve computational speed have involved a GPU-driven real-time calculation of the projected ablation zone, while incorporating the cooling effects of nearby liver vasculature [138].

2.6 Conclusion

Microwave tumor ablation is a rapidly growing modality already used to treat early-stage tumors and gaining traction in combination therapies. The ability to predict the active heating zone and heating behavior within tissue has led to improved understanding of the basic physics behind microwave ablations. The exquisite control of modeling studies affords in-depth investigation of the effects of single variables, leading to decreased experimental sample sizes and costs. Computational and experimental studies have helped optimize the design of microwave antennas, generators and techniques, facilitating clinical translation and further adoption into clinics worldwide. The concurrent development of modeling and validation will lead to better integration of patient-specific, interactive models that can change how ablation procedures are performed in the future.

Chapter 3

Parametric Design of the Dual-Slot Microwave Antenna

3.1 Abstract

Purpose: The original dual-slot antenna design, based on a bare coaxial cable, was capable of producing a more spherical ablation zone localized to the tip of the antenna, leading to less backwards heating along the shaft of the antenna. The purpose of this study was to investigate the possibility of adding a cooling component and a ceramic tip to the original dual-slot design while maintaining the same energy delivery and heating performance.

Methods: A collection of antenna geometries using an inner feeding mechanism and outer two slots were analyzed using finite-element modeling techniques. A cost function was developed to weigh the benefits of power delivery efficiency and ablation shape between each individual antenna design. The performance of the antenna with the lowest cost was then compared to that of the original dual-slot design. Individual components of the final antenna design were also analyzed separately to facilitate the fabrication process.

Results: The optimal antenna design had an outer dual-slot dimensions similar to that of the original dual-slot design. The proximal slot had a length of 1 mm, the distal slot had a lenght of 4 mm and the two slots were separated by a distance of 8 mm. The feeding slot 2mm in length supported optimal energy dispersion when placed right under the proximal slot. The operating bandwidth of this optimized design was 3 GHz, nearly double that seen in comparative monopole antenna designs.

Conclusion: The parametric optimiation process successfully added a cooling compoenent and ceramic tip into the original dual-slot microwave antenna design. Validation of these computational results in a pre-clinical environment is a logical followup to this study.

3.2 Introduction

Microwave tumor ablation has rapidly gained traction in recent years due to its inherent advantages in heating tissue homogenously to cytotoxic temperatures in highly-perfused tissue [139]. Microwave ablation systems utilize an alternating electric field to heat tissue to cytotoxic temperatures, allowing it to continuously heat through desiccated tissues and reach temperatures exceeding 100°C. As a result, compared to predecessor technologies, microwave tumor ablations are typically larger and hotter, reducing the risk for tumor recurrence [140].

A critical component of the microwave ablation system is the antenna design, which determines the radiation pattern and reflection coefficient. To date, there have been several microwave antenna designs proposed for interstitial purposes, including monopoles, dipoles, triaxial, slot and looped designs [72, 141-144]. Many of these designs have attempted to control the energy deliver or ablation zone shape and size. To achieve these goals, however, there were design costs that made clinical adoption prohibitive. For example, the choke design, which adds an extra conducting layer over an antenna, can prevent an electric field from heating backwards, thus improving ablation localization to the antenna tip [71, 145]. However, this extra layer increased the antenna diameter to the point where percutaneous insertion is difficult and potentially dangerous for a patient [146].

Previously, a dual-slot antenna had been optimized to reduce backwards heating without the addition of an extra conducting layer [147]. However, this design utilized a bare coaxial cable not suitable for clinical needs. The copper outer conductor of a bare coaxial cable often heated up during microwave ablations, causing damage around the insertion path of the microwave antenna. Furthermore, the coaxial cable by itself was also not rigid enough to facilitate percutaneous insertion through the

skin and chest wall. The introduction of a cooling apparatus to chill the coaxial cable and a ceramic tip to add rigidity could potentially address these issues. However, these additional features could not simply be placed over the existing dual-slot coaxial antenna design. The size and placement of these components directly affects the overall performance of the microwave antenna. The purpose of this study was to perform a parametric analysis of the dual-slot antenna design with the addition of a cooling apparatus and ceramic tip.

3.3 Parametric Analysis of Antenna Geometry

The cooling apparatus was determined to be confined within a stainless-steel outer cannula. Water would be able to flow in and out of this steel cannula, cooling the copper coaxial cable inside. The steel cannula would be extended up to the point where the dielectric material underneath becomes exposed, where it would also secure the ceramic element.

A preliminary analysis of our own fabrication capabilities and potential designs led to a feeding size ranging from 1-13 mm, located anywhere from 1-12 mm away from the tip of the antenna, as well as a the size of the outer copper (serving as the median of the two slots), ranging in size from 1-12 mm, located anywhere from 1-11 mm. With our fabrication tolerance extending to sizes as small as 1 mm, we determined that with these ranges, there were 20,592 possible antenna designs (**Figure 3.1**).

Analysis was performed using finite-element modeling software to solve Maxwell's equation in the transverse magnetic (TM) propagation mode (Comsol Multiphysics 3.5a; Burlington MA),

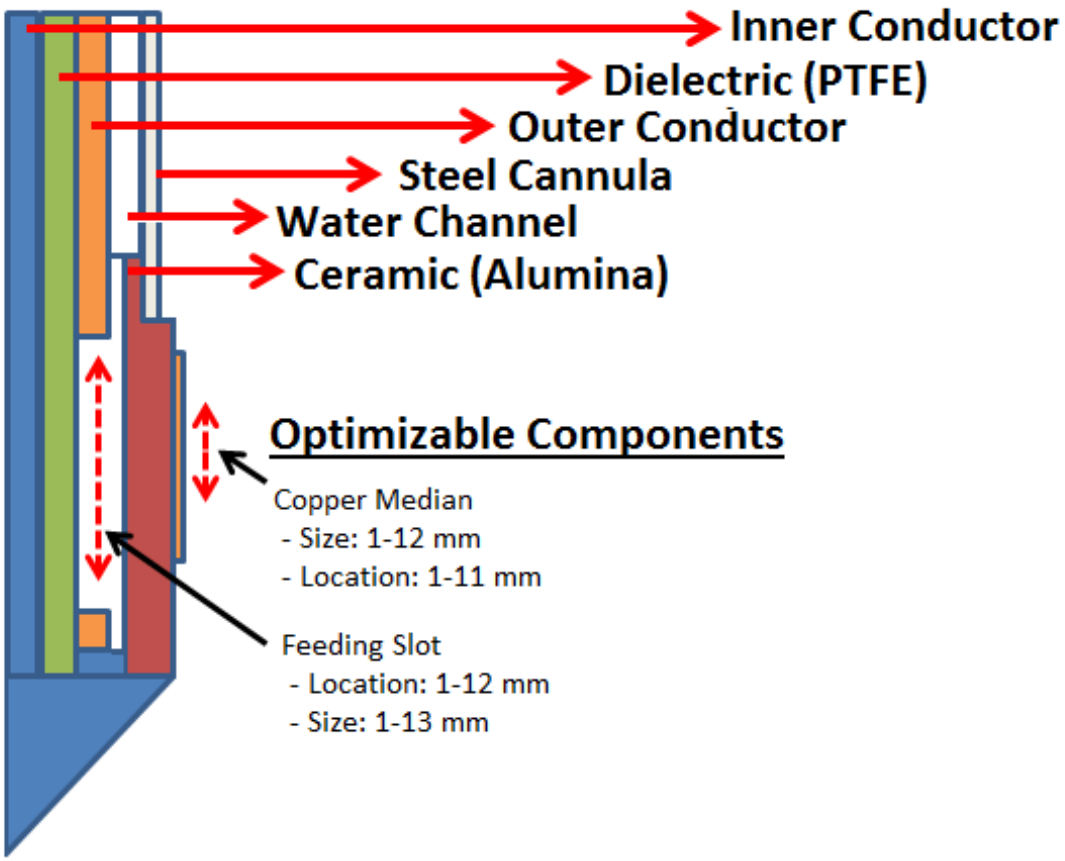

Figure 3.1: The addition of the cooling chamber added several new layers to the overall antenna design. The copper median and feeding slot led to 4 degrees of freedom that could be altered in millimeter increments.

$$\nabla^2 \mathbf{E} = \omega^2(\epsilon(f) - j\frac{\sigma(f)}{\omega})\mathbf{E} \tag{3.1}$$

where E is the electric field vector (V/m), ω is the angular frequency (rad/sec), ϵ_r is the relative permittivity (F/m) and σ is the effective conductivity (S/m). The antenna geometry was set up in a two-dimensional, axially-symmetric domain by assuming rotational symmetry along the shaft of the antenna. The metallic components, both copper and stainless steel, were considered to be perfectly electrically conducting. The dielectric material of the semi-rigid coaxial cable was assumed to be lossless

Input Variable	Expression	Description
P_{in}	1 [W]	Input Power
ϵ_{diel}	2.03	Relative Permittivity of Dielectric
ϵ_{liver}	43.03	Relative Permittivity of Liver
σ_{liver}	1.69 [S/m]	Conductivity of Liver

Table 3.1: Modeling Input Variables

PTFE (polytetrafluoroethylene). Liver properties were taken from available literature (**Table 3.1**). Input power was set to 1 W at 2.45 GHz. Triangular meshes were set to a maximum size of 3 mm.

The metrics used to rank the antennas were based on energy delivery efficiency, known as the S11, or reflection coefficient, and the shape of the ablation zone. The shape of the ablation zone was defined by the aspect ratio, or the ablation zone width divided by the ablation zone length. An isocontour outlining the ablation zone where there was an average power deposition of 3x10^4 W/m^3 was determined to be a reasonable approximation for how an ablation zone would look after 5 minutes. To determine the optimal microwave antenna design, a cost function was utilized to rank the antennas based on their performance in reflection coefficient or aspect ratio. In this case we used a cost function previously defined in [147]:

$$\Psi(\Gamma, AR) = 2 - \frac{1}{1 + e^{A_1(\Gamma + B_1)}} - \frac{1}{1 + e^{A_2(AR + B_2)}} \tag{3.2}$$

where A_1 was set to 0.5, A_2 was set to -10, B_1 was set to 15, and B_2 was set to -0.7. As you can see in the cost-figure below, these constants translated to a lower "cost" if the reflection coefficient was lower than -10 dB, or had an aspect ratio that was higher than 0.5 (**Figure 3.2**). The lower aspect ratio and higher aspect ratio led to a smaller cost and an improved ranking. We used this objective function to score and rank all 20,592 antenna designs.

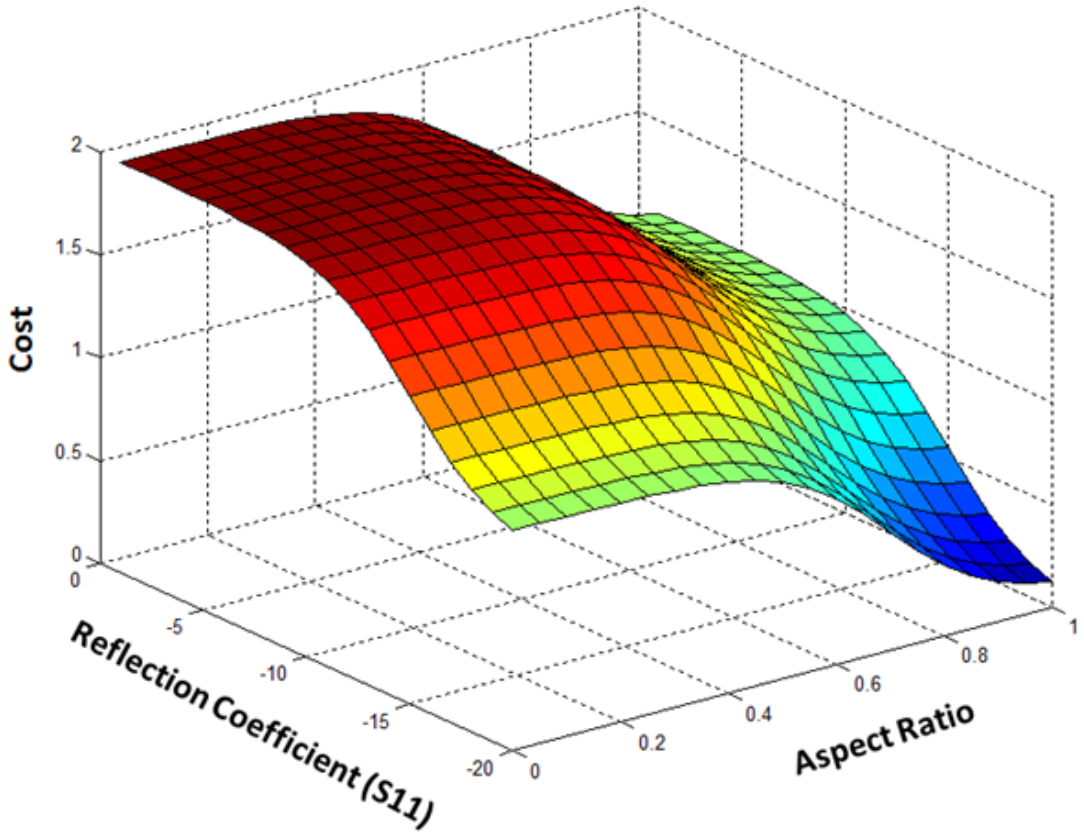

Figure 3.2: The antenna cost function was used to weigh the separate advantages of having a more spherical ablation zone against have more efficient energy delivery into the tissue. Antennas that had the best balance between the two features would be assigned a lower "cost."

3.4 Results

The antenna design with the lowest score, and hence the most optimal design was shown to have an outer copper size of 8 mm, located 4 mm from the beginning of the tip of the antenna, which was embedded within the ceramic heating zone. The interior slot location was located 11 mm from the beginning of the tip, with a slot width of 2 mm. Thus, the inner slot would be primarily feeding the proximal slot of the antenna. This antenna design was shown to have an ablation zone diameter of 1.9 cm and a heating length of 2.8 cm, for an aspect ratio of 0.67. The reflection

coefficient of this theoretical design was given as -22.5 dB. It is interesting to note that the top 8 antenna designs have a similar outer design found in the original coaxial design and the performance varied based on where the inner feeding structure was located.

Rank	1	2	3	4	5	6	7	8
Copper Size (mm)	8	8	8	8	8	8	8	7
Copper Space (mm)	4	4	4	4	4	4	4	4
Slot Size (mm)	11	10	10	10	9	9	8	7
Slot Location (mm)	2	3	2	1	4	3	5	6
Aspect Ratio	0.66	0.67	0.67	0.67	0.68	0.68	0.69	0.70
S11	-22.5	-23.7	-21.2	-21.1	-22.1	-20.2	-21.4	-19.8
Score	0.22	0.22	0.23	0.25	0.25	0.25	0.26	0.26

[Top 8 Results from Parametric Study]The top 8 results showed relative robustness in terms of slot size and location. However, the outer design, which mimicked that of the original, bare-coaxial dual-slot antenna, needed to remain the same.

The resonance structure of this design had two peaks, one at 0.9 GHz and one at 2.5 GHz. These peak resonance frequencies are similar to the resonance frequencies of the two outer slots seen in the original dual-slot design. The operating bandwidth, or where the antenna operates at greater than 90% forward power, was 3 GHz, nearly double that of a monopole antenna.

The heating zone of the antenna was centered on the proximal slot, sitting above the feeding slot in the radial direction. Removal of the outer copper, which eliminates the outer dual slots and effectively deconstructs the antenna into a single-slot antenna, results in electric field propagation along the shaft of the antenna.

While the reflection coefficient stayed approximately the same, the aspect ratio dropped dramatically (**Figure 3.6**).

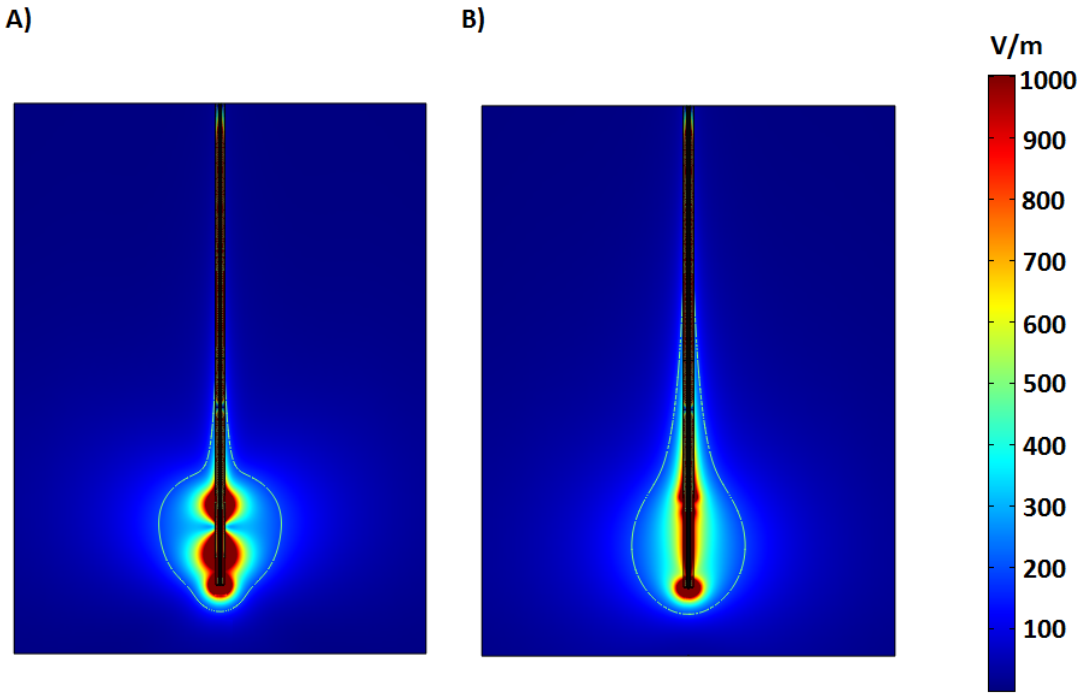

Figure 3.3: The outer copper was required to be located on the ceramic for the antenna to deliver energy efficiently. Removing the outer copper led to a drop in antenna performance.

3.4.1 Analysis of Individual Components

As a validation step, we also looked at the results of the parametric study with respect to individual components, using ablation sizes, reflection coefficient and aspect ratios as the metrics. While some designs led to better aspect ratios than what the parametric study converged upon, their associated reflection coefficient was much lower and thus did not appear in our top 8 list.

Outer Cannula

The outer cannula was found to have improved performance as its interface with the ceramic was moved down toward the location of the outer copper (**Figure 3.4**). The aspect ratio moved from 0.5 to 0.8 as the cannula length was extended toward the outer copper tape. The increase in aspect ratio was primarily due to the decrease in ablation zone length, as the ablation diameter remained unchanged with various cannula lengths. There was also relatively little change between reflection coefficients at various cannula lengths, as the S11 stayed around -10 to -12 dB. Minimizing the distance between the steel cannula and the copper tape re-confirmed that the 1 mm spacing found in the final design was the correct length to use.

Ceramic Length

Extending the length of the ceramic within the steel cannula exhibited sinusoidal behaviors in terms of antenna performance(**Figure 3.5**). The aspect ratio of the ablation zone varied from 0.4 to 0.8, due to the changing ablation length as the ceramic was extended. The reflection coefficient also varied sinusoidally, and suggested that the ceramic length within the cannula had a direct effect on the resonant wave pattern and propagation within the steel cannula and antenna.

Feeding Slot Size

The feeding slot was shown to have the optimal size near the proximal slot, where the ceramic interfaced with the outer cannula (**Figure 3.6**). At the top location, the aspect ratio peaked right under 0.5, but the reflection coefficient was around -10 dB. Enlarging the feeding slot to 4 mm would drop the reflection coefficient to -15 dB but would simultaneously decrease the aspect ratio below 0.4. The parametric

study narrowed the optimal feed slot size to 2 mm, which is a compromise between the sizes leading to the largest aspect ratio and the smallest reflection coefficient.

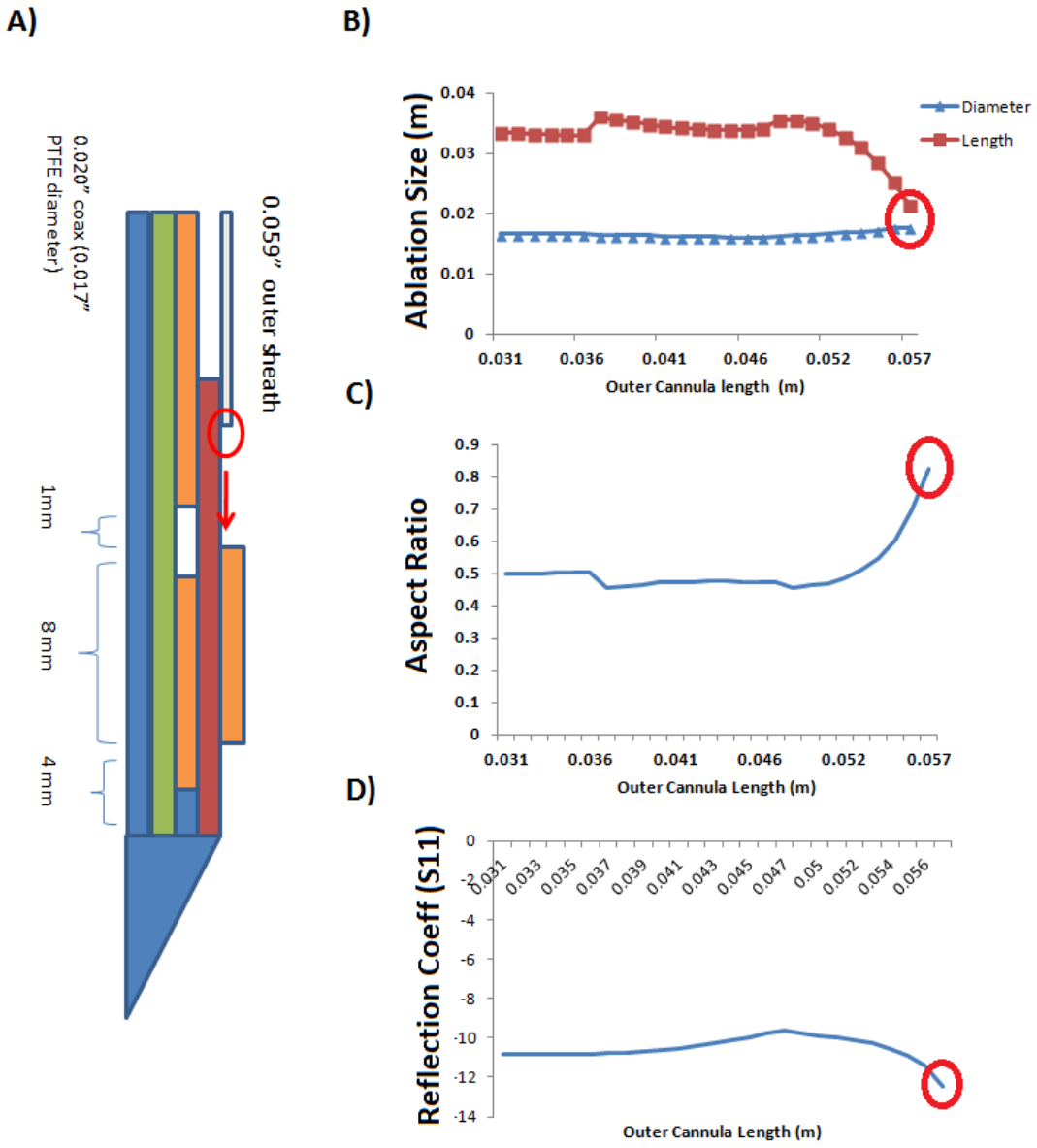

Figure 3.4: Ablation zones were more spherical and energy was delivered more efficiently as the cannula covered more of the ceramic.

]Feeding slot size did not play a large factor in the overall antenna performance. Within a wide range of values, the aspect ratio and ablation aspect ratio remained stable.

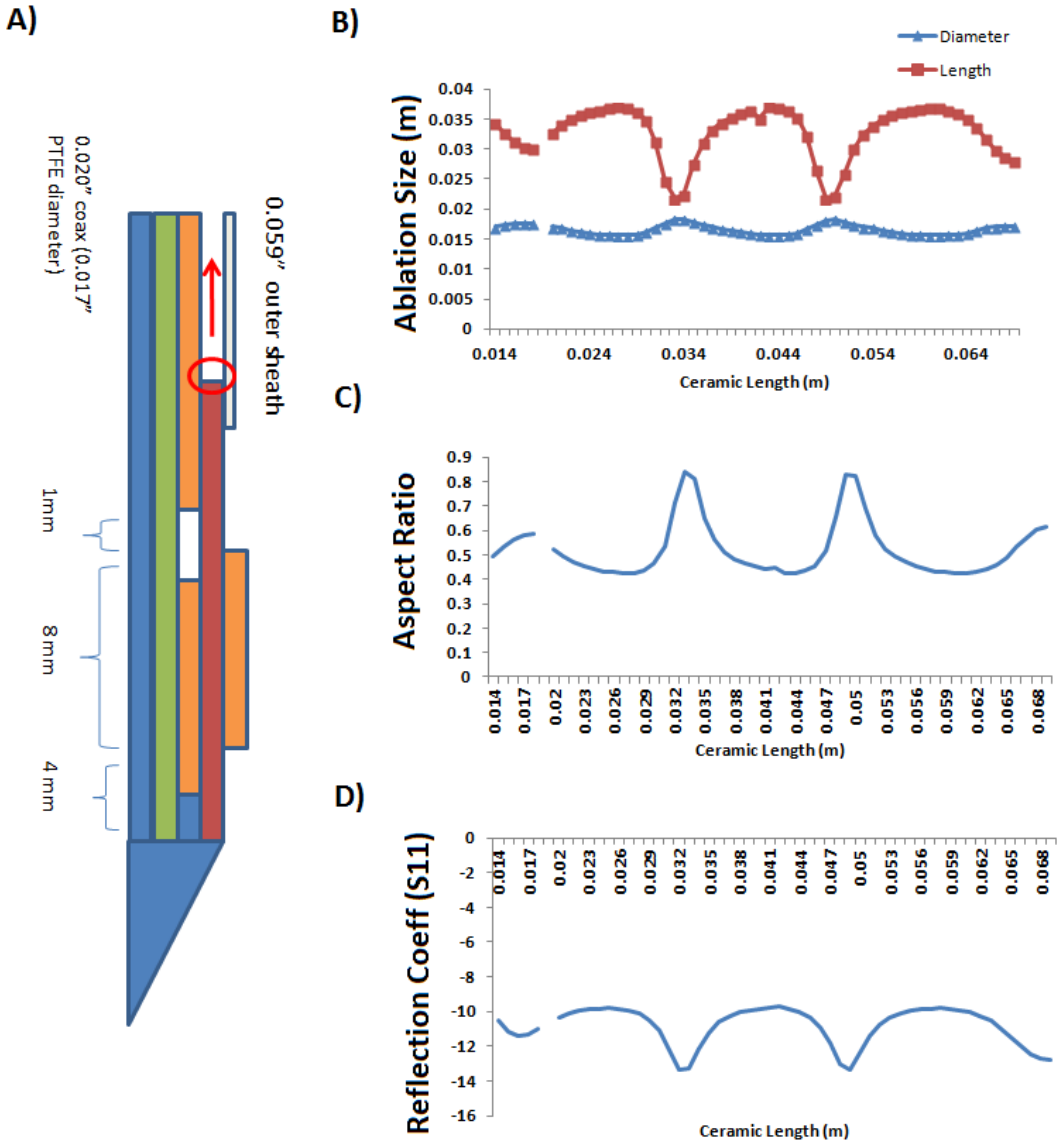

Figure 3.5: Ceramic length showed a sinuosidal relationship with antenna performane as it extended into the outer cannula. Millimeter shifts in ceramic length within the cannula could lead to large drops in antenna performance.

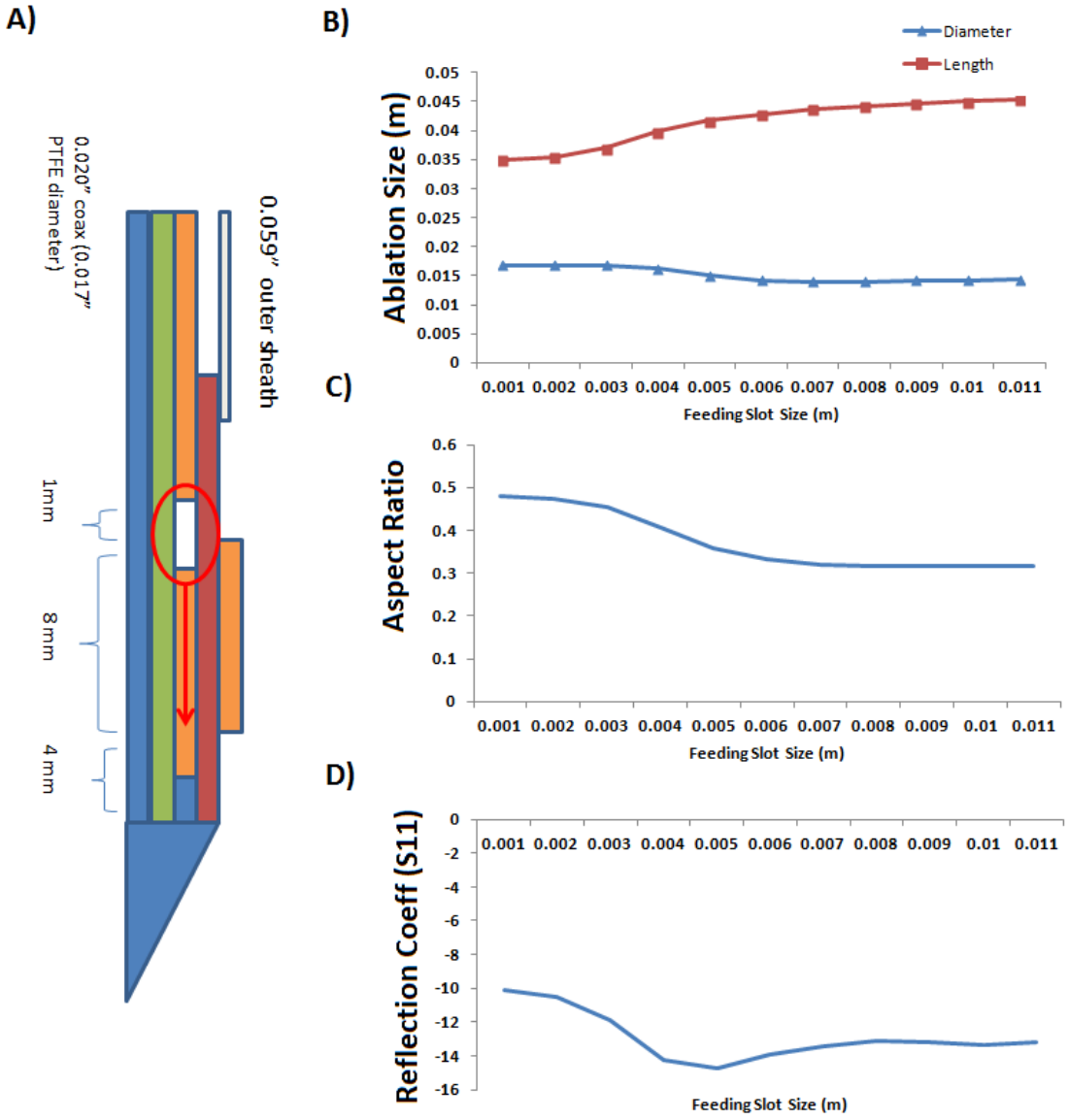
A)
0.020" coax (0.017" PTFE diameter)
0.059" outer sheath
1mm
8 mm
4 mm
B)
Diameter
Length
Ablation Size (m)
0.05
0.045
0.04
0.035
0.03
0.025
0.02
0.015
0.01
0.005
0
0.001 0.002 0.003 0.004 0.005 0.006 0.007 0.008 0.009 0.01 0.011
Feeding Slot Size (m)
C)
Aspect Ratio
0.6
0.5
0.4
0.3
0.2
0.1
0
0.001 0.002 0.003 0.004 0.005 0.006 0.007 0.008 0.009 0.01 0.011
Feeding Slot Size (m)
D)
Reflection Coeff (S11)
0
-2
-4
-6
-8
-10
-12
-14
-16
0.001 0.002 0.003 0.004 0.005 0.006 0.007 0.008 0.009 0.01 0.011
Feeding Slot Size (m)

3.5 Discussion

This chapter discussed the design of a pre-clinical version of the original dual-slot antenna. The addition of the cooling component and ceramic necessitated an optimization process to maintain the benefits in the original dual-slot antenna. Finite-element modeling was used to evaluate over 20,000 potential dual-slot antenna designs. The optimal design yielded results similar to the predecessor dual-slot antenna [147], with a slightly lower aspect ratio, 0.66 versus 0.70 but slightly improved energy delivery efficiency, -22 dB versus -20 dB.

Like the previous dual-slot design, the distal slot size of 4mm represents an approximately quarter wavelength of the microwave energy at 2.5 GHz in liver tissue (1.8 cm), introducing a 180 degree phase shift in its reflection. The two sources of electric field propagation cancel each other out along the shaft of the antenna, to create an active "choke" without increasing the diameter of the antenna. The study demonstrated that we were able to maintain this benefit through proper placement and sizing of the cooling component and ceramic tip.

The operating bandwidth of this optimized dual-slot antenna was found to be larger than conventional monopole antennas. With an operating bandwidth twice as large, the antenna is potentially capable of maintaining superior energy delivery performance in a variety of tissue conditions and types. This can be useful when the tissue changes as water vapor is moved out and desiccation occurs, changing the electrical and thermal properties of the liver. Due to the multiple degrees of freedom in this cooled dual-slot antenna, many modifications can be incorporated to impedance match the antenna to the organ of interest.

A more spherical ablation zone has many benefits in a clinical workflow, especially from the standpoint of patient safety. Microwave energy is unique in its ability

to heat through a wide variety of tissue conditions. However, its implementation has been stalled by suboptimal antenna designs, which need to be matched to the tissue condition it is delivering energy into. The high-powered microwave generator is of little use if the antenna cannot efficiently deliver it into the tissue. Poor matching between the antenna and tissue can cause power to be reflect back along the coaxial needle and along the shaft, causing damage to nearby anatomy and body wall. Previous attempts to reduce shaft heating involved adding an active "choke" or an additional conducting layer over the entire antenna. This extra layer increased the antenna diameter in a way that became cumbersome for percutaneous usage in a clinical setting. Adopting the dual-slot antenna design led to an active reduction of backwards heating can allow for greater energy deposition into tissue without active heating along the shaft of the antenna.

There were specific limitations to this optimization study. The first is that we utilized a parametric design process, which does not explicitly converge to any maxima or minima. In that sense, this is not a true optimization process. We needed to define our own logarithmic cost function to determine what the optimal antenna design should look like. Another weakness of the study is the lack of sensitivity analysis. Although there was a brief summary of individual components, further studies on insertion depth and changing tissue conditions would lead to further insight on the true performance of this specific dual-slot antenna design.

3.6 Conclusion

We were able to demonstrate the possibility of adding a cooling layer and ceramic to the bare dual-slot coaxial antenna design, thus bringing it one step closer to clinical implementation. We utilized a parametric finite-element modeling study

and a ranking algorithm to find the most optimal microwave antenna design. The optimal cooled antenna design was shown to have an aspect ratio of 0.66, a reflection coefficient of -22 dB and an operating bandwidth spanning over 3 GHz. In the next chapter, we will validate the performance of this optimized, cooled dual-slot in an ex-vivo and in-vivo liver environment.

Chapter 4

Validation of the Dual-Slot Microwave Antenna

4.1 Abstract

Purpose: The goal of this study was to compare the performance of a dual-slot microwave antenna design, characterized by two annular slots, to a monopole antenna design in creating a more spherical ablation zone.

Methods: Animal care and use committee approval was obtained prior to in-vivo experiments. Microwave ablation zones were created using dual-slot and monopole control antennas for 2, 5 and 10 minutes using 50 and 100 W in ex-vivo bovine livers and at 100 W for 5 min in in-vivo porcine livers, which also underwent intra-procedural imaging. Ablation diameter, length and aspect ratio (diameter/length) were measured with gross pathology and compared at each power-time combination using the paired Student's t-test. Results were considered significant at $p<0.05$. Aspect ratios closer to 1 reflect a more spherical ablation zone.

Results: The dual-slot antenna created ablation zones with a higher aspect ratio using 50 W for 2 minutes (0.75 vs 0.53, p=0.0025) and 5 minutes (0.82 vs 0.63, p=0.0527) compared to the monopole in ex-vivo liver tissue, although only significantly so at the earlier time point. At 100 W, the dual-slot had a significantly higher aspect ratio at 2 minutes (0.52 vs 0.42, p=0.0017). In-vivo studies showed significantly higher aspect ratios using 100 W at 5 minutes (0.63 vs 0.53, respectively, p=0.0292). Intra-procedural imaging confirmed this characterization showing higher rates of ablation zone growth and heating primarily at the early stages of the ablation procedure using the dual-slot antenna.

Conclusions: The dual-slot microwave antenna was capable of creating a more spherical ablation zone than the monopole antenna in both in-vivo and ex-vivo liver tissue. Greater control over power delivery can potentially extend the advantages of the dual-slot antenna design to higher power-time points.

4.2 Introduction

Percutaneous tumor ablation is a minimally-invasive procedure that destroys cancerous tissue in-situ via cytotoxic thermal energy. Thermal ablation procedures are associated with quicker recovery and fewer complications compared to surgical resection and now play a critical role in the management of early-stage hepatocellular carcinoma (HCC), hepatic metastases, renal cell carcinoma, peripheral lung nodules, osteoid osteomas and osteosarcomas [148, 149]. While radiofrequency ablation (RFA) is the most widely used ablation modality to date, it is limited by heat-induced desiccation and poor performance near blood vessels. Such limitations to heating can lead to potentially inadequate ablation zones and a higher rate of local tumor progression compared to resection [149, 150]. Microwave ablation, on the other hand, has been shown to heat larger volumes of tissue to greater temperatures, potentially increasing procedural efficacy [44, 140, 151].

Interstitial antennas couple power from the microwave generator into the target tissue. The pattern of heating around the antenna varies by antenna design, but high power delivery can also promote electric field propagation along the proximal shaft during an ablation treatment [72, 141, 142, 152, 153]. This effect can cause procedural complications such as body-wall burns and restrict where the applicator can be placed [35, 85, 154]. Such complications may be reduced by cooling the skin surface and limiting the power or duration of the treatment; however, these techniques add procedural complexity and reduce ablation zone size [155]. Antenna cooling can effectively reduce shaft heating but has minimal effect against ablation zone elongation [81, 156-158].

A dual-slot antenna geometry comprising of two coaxial, annular slots at the distal tip of the antenna, was recently shown to inhibit proximal electric field prop-

agation and, therefore, shorten the length of ex-vivo ablations [69]. However, the antenna in that study was created from relatively malleable coaxial cables without active shaft cooling, making it unsuitable for clinical use. A dual-slot antenna was recently developed that incorporates a rigid, sharpened tip and internal water cooling to facilitate percutaneous use while maintaining its original performance. The goal of this study was to compare the performance of a dual-slot microwave antenna design, characterized by two annular slots, to a monopole antenna design in creating a more spherical ablation zone.

4.3 Materials and Methods

The microwave antenna devices used in this study incorporate aspects of multiple patents pending. No industrial support was provided for this study. Author C.L.B. is a founder, shareholder and consultant for Neuwave Medical. Study data and publication information were controlled by J.C. Using a parametric analysis similar to previous work, we designed a dual-slot antenna with a built-in shaft cooling channels and a coaxial feed separate from the trocar tip to simplify fabrication. The optimal cooled design provided a heating pattern and power delivery efficiency similar to the uncooled design previously described [69]. A cooled monopole antenna served as a control antenna for comparison of ablation performance (**Figure 4.1**). Both antennas were fabricated using a thin coaxial antenna (UT-020C; Micro-Coax LLC, Pottstown, PA), an alumina ceramic tip to enhance rigidity (McDanel Advanced Ceramic Technology LLC, Beaver Falls PA), and a 17-gauge steel catheter to create the cooling channel (MicroGroup, Medway, MA). Antennas were fabricated by two authors (authors K.H. and J.C., each with 2 years experience)

Microwave power was delivered by a continuous-wave 2.45 GHz magnetron

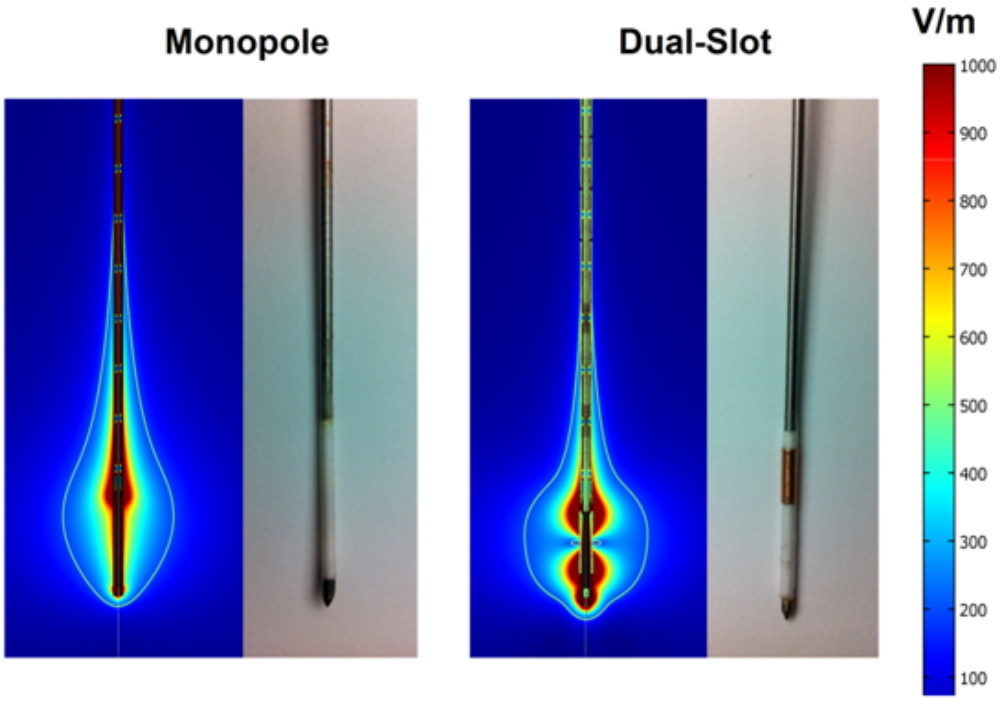

Figure 4.1: Dual-Slot versus Monopole. Numeric modeling image and photograph of monopole antenna (left) and dual-slot antenna (right). In modeling images, color bar represents electric field intensity from 100 to 1000 V/m. Monopole antenna shows electric field emanating from tip of steel catheter; dual-slot antenna shows electric field from each of its slots. White line represents volumetric heating rate of 3 3 104 W/m3, giving a visual approxima-tion of what ablation zone may look like in liver tissue. Note decreased active heating on shaft of dual-slot antenna compared with that of monopole.

source (MG300, 2.45 GHz; CouberMuegge LLC, Norwalk, CT) and transferred to the antenna via a 6-foot RG-400 coaxial cable. Cable losses were measured using a wideband power sensor (Birds Electronic Corp, OH) and used to recalibrate the generator output to ensure delivery of the prescribed power into the tissue.

4.3.1 Ex-vivo Liver Ablation

Microwave antenna performance was initially validated using ex-vivo bovine liver tissue. The liver was sectioned into 6 cm by 6 cm by 9 cm blocks and warmed to room temperature before each experiment. The microwave generator was set to deliver 50 W and 100 W for 2 min, 5 min and 10 min for each antenna. Six samples were performed per power-time (authors K.H. and M.B. both with 2 years experience) combination for a total of 36 dual-slot and 36 monopole ablations. The ablation zone was sliced along the antenna axis for gross pathology analysis. Slices were scanned optically and images stored for analysis using ImageJ 1.43u (US National Institutes of Health, Bethesda, MD). The maximum dimension of the ablation zone transverse to the antenna was defined as the ablation diameter, while the maximum dimension along the antenna insertion path was considered the ablation length. The aspect ratio was defined as the diameter divided by the length. An aspect ratio approaching 1 indicates that the ablation length is approaching that of its diameter, indicating a more spherical ablation zone.

4.3.2 In-vivo Liver Ablation

All studies were conducted with approval from our institutional animal care and use committee and were compliant with National Research Council guidelines [159]. A total of 4 ablations (n=2 using the dual-slot and n=2 using monopole) were created (author J.C. and veterinary technician L.S., with 2 and 12 years of experience, respectively) using 100 W for 5 minutes in each of six female domestic swing ranging from 80-90 kg (Arlington Farms, Arlington, WI) for a total of 24 ablations (n=12 monopole and n=12 dual-slot). For each animal, half (n=2) of the ablation for each experimental arm were performed in the medial lobes and

the other half were performed in the lateral lobes to account for differences in perfusion rates. Ablations that protruded beyond the parenchyma of the tissue or experienced antenna failure were excluded from the results. After exclusion of incomplete ablation zones, there were 8 dual-slot ablations and 8 monopole ablation zones in the in-vivo study. Animals were sedated with intramuscular tiletamine hydrochloride-zolazepam hydrochloride (7 mg/kg, Telazol, Fort Dodge, IA) and xylazine hydrochloride (2.2 mg/kg, XylaJect, Phoenix Pharmaceutical, St Joseph MO). Anesthesia was maintained with inhaled 1.0-2.0% isofluorane (Halocarbon Laboratories, River Edge NJ). An ear vein was cannulated with a 20-gauge angiocath for administration of IV fluids.

After ablation, animals were sacrificed by means of an intravenous injection of Beuthanasia-D (390 mg/mL, pentobarbital sodium and 50 mg/mL phenytoin sodium at 0.2 mL/kg IV; Schering-Plough, Kenilworth, NJ). The liver was removed and sectioned along the axis of each antenna. Image analysis was performed in the same way as with ex-vivo tissue. Non-contrast CT imaging was used to assess ablation growth in two of the animals. Prior to the ablation, a roadmap CT scan was performed through the entire liver. During the ablation, CT data were acquired every 30 seconds. (120 kV, 200 mA, 512512, 1:1 helical pitch, 5 mm slice thickness). A threshold was set at 35 HU, which was approximately 16 HU below the background liver density , on post-processing software (Volume Viewer v3.1; Advantage Windows v4.5, General Electric Medical Systems) to detect and monitor ablation zone area growth at each time point. This value was chosen based on previous CT studies noting the average 16 HU difference between ablated lesion from RFA and the background tissue [116]. The final threshold image was compared with gross pathology to confirm validity of using our threshold technique to monitor ablation growth. The central hypodense region, representing a heated gaseous

region surrounding the emission point, was also monitored with diameter, length and overall area being recorded at each time point.

4.3.3 Statistical Analysis

To ensure that there were no probe-lobe interaction effects, we compared the ablation zone characteristics produced by each antenna while accounting for placement in lobe. Since the effects seemed additive, we averaged over lobes by probe-type to produce a single monopole/dual-slot pair per animal. Differences in mean diameter, length and aspect ratio were identified between the dual-slot and monopole antenna designs, amongst power-time combination using a paired Student's t-test. The paired Student's t-test was considered appropriate after validating approximately equal variances and symmetric distribution among comparison groups. P-values less than 0.05 were considered significant. Statistical analysis was performed using Graphpad Prism v5.04 (La Jolla, CA, USA) with assistance from the departmental statistician.

4.4 Results

4.4.1 Ex-vivo Results

Power-time dose responses of the monopole and dual-slot antennas are shown below (**Figure 4.2**). At 50 W, the dual-slot antenna created ablation zone diameters similar to those of the monopole at 2 minutes (1.95$\pm$0.18 versus 1.79$\pm$0.27 cm, respectively; p=0.2775), 5 minutes (2.12$\pm$0.14 versus 2.32$\pm$0.18 cm; p=0.0784) and 10 minutes (3.01$\pm$0.29 versus 3.02$\pm$0.16 cm; p=0.9869). With respect to ablation length, the dual-slot antenna created significantly shorter ablation zones compared to those of

the monopole antenna at 2 minutes (2.64±0.30 versus 3.38±0.42 cm; p=0.0074) and 5 minutes (2.61±0.34 versus 3.83±0.92 cm; p=0.0199), but not at 10 minutes (5.14±0.64 versus 4.71±0.51 cm, respectively; p=0.2249). Accordingly, the combination of equivalent diameters and shorter ablation lengths led to a greater aspect ratio for dual-slot ablation zones at 2 minutes (0.75±0.11 versus 0.53±0.04, p=0.0025) and 5 minutes (0.82±0.13 versus 0.63±0.14, p=0.0527) but not at 10 minutes (0.59±0.07 versus 0.64±0.05, p=0.1677).

At 100 W, the dual-slot antenna created ablation zones with diameters greater than those created by the monopole antenna at all time points (2.14±0.15 versus 1.86±0.24 cm at 2 minutes, p=0.0315; 3.07±0.35 versus 2.80±0.19 cm at 5 minutes, p=0.0770; 3.86±0.32 versus 3.12±0.48 cm at 10 minutes, p=0.0169), but only significantly so at 2 and 10 minutes. On the other hand, no differences were noted between ablation lengths between the dual-slot and monopole at any time points (4.16±0.20 versus 4.44±0.44 cm at 2 minutes, p=0.1855; 4.83±0.50 versus 4.62±0.31 cm at 5 minutes, p=0.3545; 6.04±1.35 versus 5.55±0.69 cm at 10 minutes, p=0.4580). Collectively, the greater ablation diameter of the dual-slot antenna with the equivalent ablation lengths led to a significantly higher aspect ratio than that of the monopole antenna at only 2 minutes (0.52±0.03 versus 0.42±0.05, p=0.0017), with the aspect ratios being statistically similar at 5 minutes (0.64±0.05 versus 0.61±0.03, p=0.1907) and 10 minutes (0.66±0.13 versus 0.56±0.06, p=0.1358).

4.4.2 In-vivo results

In-vivo studies confirmed the trends shown in the ex-vivo studies (**Figure 4.3A**). The dual-slot antenna created a significantly greater diameter (2.85±0.45 versus 2.35±0.42 cm, respectively; p=0.0340) and a slightly shorter length (4.47±0.71 cm versus 4.59±0.81 cm, respectively; p=0.5970), leading to a significantly greater aspect

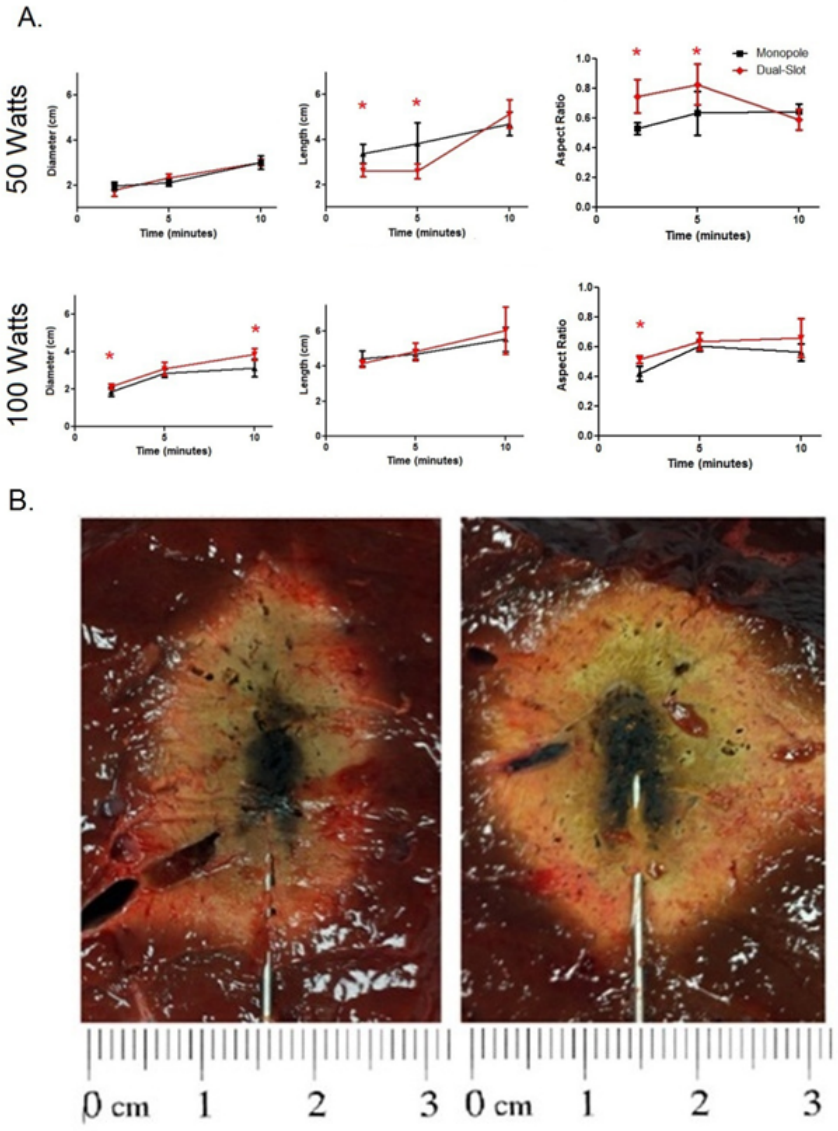

Figure 4.2: Ex-vivo data A) Graphs show ablation diameter, length, and aspect ratio of ex vivo ablations comparing dual-slot with monopole antennas. Solid dots represent sample mean, and horizontal line segments represent standard deviation. $*$ = significant difference ($P<.05$). B) Sample ablation zone created by dual-slot (left) and mono-pole (right) antennas at 100 W for 5 minutes. Dual-slot antenna created significantly shorter and more spherical ablation zone than did monopole antenna at 50 W for 2 and 5 minutes. Dual-slot antenna created a significantly wider and more spherical ablation zone compared with monopole antenna at 100 W for 2 minutes

ratio compared to the monopole antenna (0.63±0.08 versus 0.53±0.08, respectively, p=0.0291).

Intra-procedural CT with thresholding confirmed these trends, with the final ablation zone of the dual-slot antenna showing a greater diameter and shorter ablation zone compared to the monopole antenna ablation zone. Intra-procedural CT also demonstrated differences in the ablation zone growth pattern. The diameter of the dual-slot ablation zone was similar to that of the monopole at the start of the procedure but grew much faster than the monopole until 4 minutes into the procedure. After this point, the growth rate of the diameter slowed down, while the monopole ablation diameter continued to grow in a linear fashion. The ablation length of the dual-slot antenna was shorter than that of the monopole antenna at nearly every time point, although the growth rate was approximately the same. The combination of the dual-slot antenna creating a wider ablation zone while maintaining a shorter ablation length led to the dual-slot antenna having a greater aspect ratio at every time point during the 5 minute ablation (**Figure 4.3C**).

Intra-procedural CT also demonstrated differences in heating pattern, which was demarcated by a coarse outline of hypodense region (less than -300 HU), most likely representing water vaporization at the interface between tissue and the antenna heating element (**Figure 4.4A**). The hypodense region was noted initially near the base of the monopole radiating segment, approximately 20 mm proximal to the antenna tip. The dual-slot antenna created a similar region approximately 5 mm proximal to the tip. That region grew slightly along the proximal antenna shaft but to a lesser degree than that of the monopole. The growth rate of the hypodense region area varied between antenna designs (**Figure 4.4B**). The dual-slot antenna created a larger hypodense region at all time points compared to the monopole, suggesting a higher rate of local heating and subsequent vaporization. In terms of

growth rate, both antennas created the majority of the hypodense region within the first 2 minutes, the dual-slot antenna appeared to plateau within 3 minutes, while the monopole antenna's hypodense region continued to grow steadily until 5 minutes.

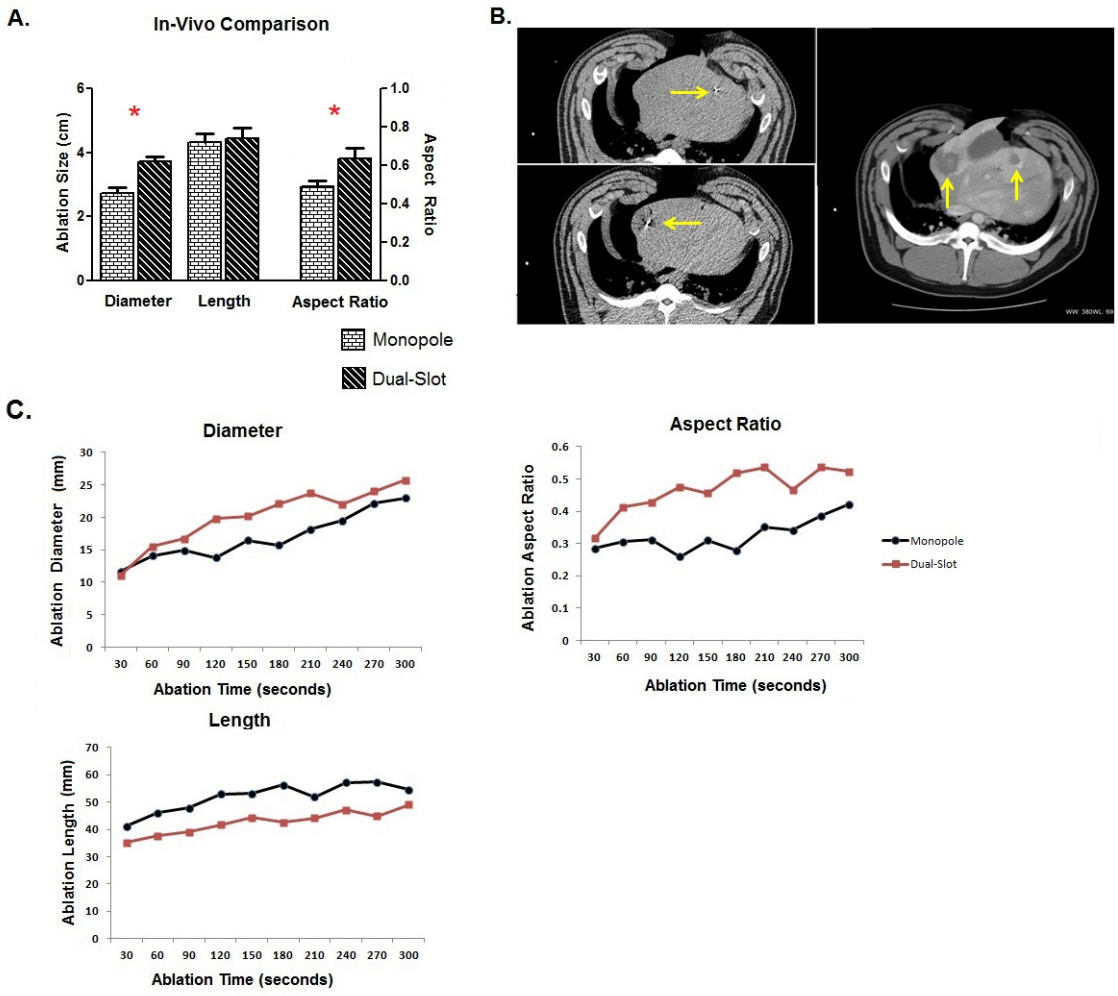

Figure 4.3: In-vivo data. A) Bar graph shows in vivo diameter, length and aspect ratio of dual-slot and monopole antennas at 100 W for 5 minutes. Dual-slot antenna created ablation zones that were significantly wider and more spherical than those created by using monopole antennas. This is consistent with trends found in power and treatment length in ex vivo tissue. $*$ = significant difference ($P < .05$). B) Sample intraprocedural images show microwave antenna placement in porcine liver. C) Intraprocedural monitoring of ablation zone diameter, length, and aspect ratio during in vivo ablation with dual-slot and monopole antennas.

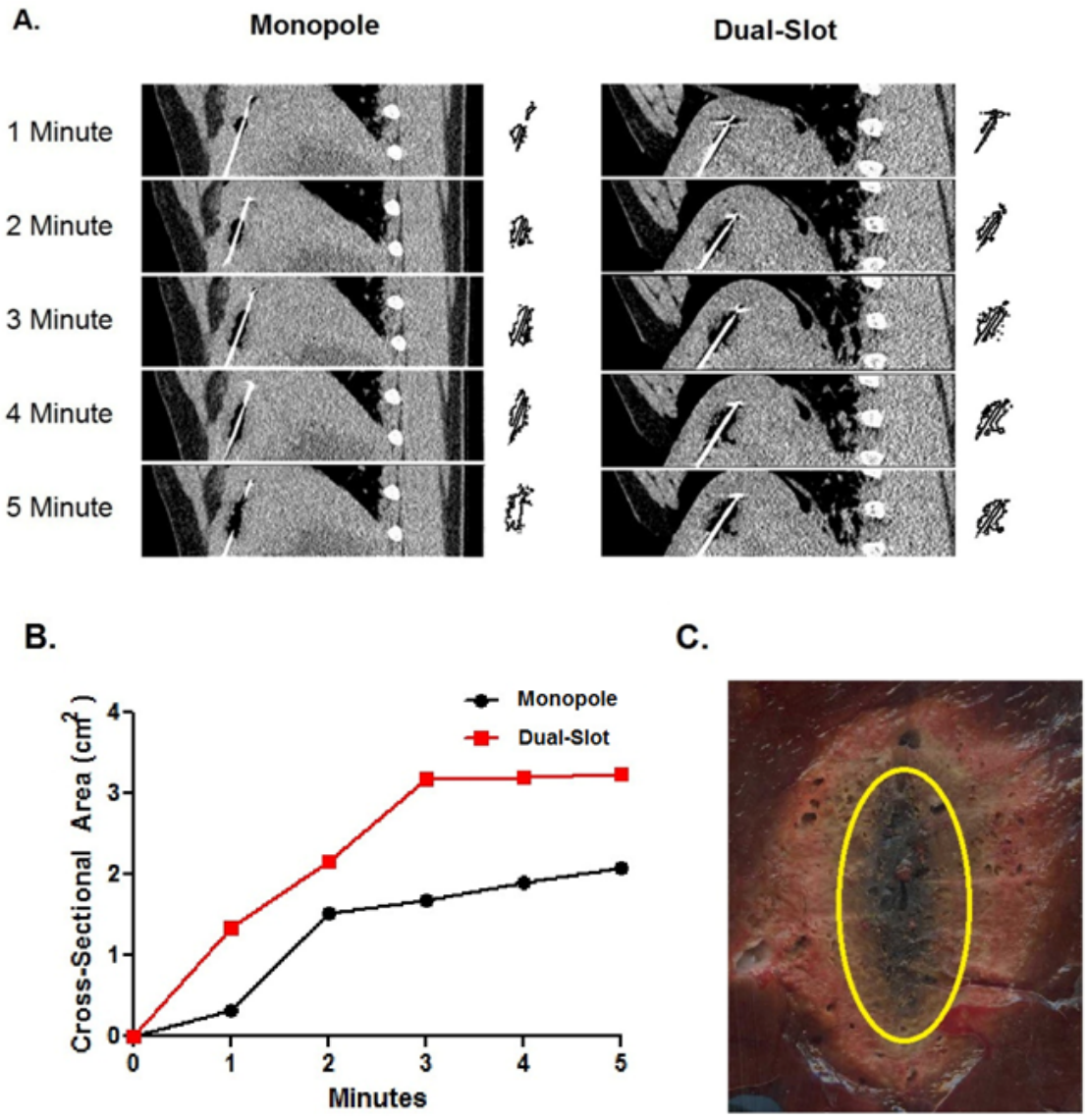

Figure 4.4: A) In vivo intraprocedural CT images of monopole (left) and dual slot (right) antennas show differences in hypoat-tenuating area corresponding to vapor formation around heating element. Hypoattenuating region outlines appear on the right of each CT image. B) Graph shows comparison of the hypoattenuating cross-sectional areas of dual-slot and monopole antennas at 1-minute intervals. C) Gross histologic examination shows hypoattenuating region demarcating area of central desiccation in ablation zone. Dual-slot antenna is capable of maintaining hypoat-tenuating region of growth longer and of creating overall larger hypoattenuating area compared with that of monopole antenna.

4.5 Discussion

Our study characterized the ablation zone produced by water-cooled dual-slot antenna in a preclinical liver tissue model. Compared to a cooled monopole antenna, dual-slot ablations were characterized by greater diameter-to-length aspect ratios, particularly for treatment times less than 5 minutes. Greater aspect ratios were attributed to shorter ablation lengths when using lower power, and increased ablation diameters at higher power. Similar trends were observed in-vivo, although ablation zones were markedly smaller and more spherical than those made in ex-vivo tissue due to the presence of perfusion.

Our results suggest that antenna design may be more effective at actively controlling the ablation shape for the first few minutes of the ablation. After that time, effects such as thermal conduction and tissue property changes may wash out earlier differences. Schramm et al predicted only a small influence of thermal conduction on microwave ablations, but that study did not account for water vaporization or associated heat transfer [130]. Ji et al noted an increase in the ablation zone length over time when accounting for dielectric property changes caused by vaporization and desiccation around the antenna shaft [107]. Our study appears to confirm those findings, as noted by the lack of difference between dual-slot and monopole ablation aspect ratio at 10 minutes. This evidence suggests that power delivery techniques may need to be tailored to a particular antenna design to optimize treatment results at earlier time points.

Intra-procedural imaging revealed differences in ablation zone growth and vapor formation between both antennas, which may contribute to the final gross pathology results. The dual-slot ablation length started out shorter than that of the monopole and maintained that difference throughout the procedure, with both ablation zones

growing at approximately the same rate. Although our gross pathology studies reveal only snapshots of the entire ablation growth curve, these imaging results confirm the ablation trends found in both the in-vivo and ex-vivo studies.

Zones of extreme hypodensity were also monitored near the ablation applicator, corresponding to water vaporization in the tissue [107]. The vapor zones corresponded approximately to the centrally blackened, desiccated area in the middle of the ablation zone, which appeared to experience much higher temperatures compared to the transition zone, which was darker but maintained its structure on gross pathology. Similar to the overall ablation trends found in the ex-vivo, in-vivo and imaging studies, there is evidence of a dynamic heating profile specific to each antenna design. This region of desiccation has potential implications in post-operative pathology or monitoring in demarcating areas where cells potentially experience thermal fixation [160].

The ablation zones found with the dual-slot antenna were comparable with those found in other cooled antenna designs. Ablation zones by the monopole antenna and dual-slot antenna were both larger than the cooled dipole antennas reported by Sun et al and Zhou et al , in both diameter and length at 50 W, but reported comparable dimensions at the higher powers (80-100 W for 10 minutes) [81, 161]. These studies are confirmatory in that antenna designs create distinct ablation zones at lower powers but become similar to each other at higher powers. Hines-Peralta et al characterized a cooled large-gauge antenna that created much wider and longer ablation zones compared to the ones reported here, but utilized an antenna that was much greater in diameter [158]. Cavagnaro et al reported a validation study with cooled choked-dipole design, which added a third outer conductor over an entire dipole antenna [157]. Their ex-vivo results showed an increasingly spherical ablation zone as ablation length continued, up until 15 minutes at lower powers (20-

60 W). At shorter time periods the choked-dipole antenna design created ablation zones that were more elongated, with comparable diameters, compared to those created by the dual-slot antenna. Comparisons between ex-vivo and in-vivo studies were consistent with these previous studies, where the in-vivo ablation zones were noticeably smaller than those created in ex-vivo tissue. One exception was with the Hines-Peralta study, where the in-vivo ablation zones were larger than the ex-vivo ablation zones for all 150 W ablations under 10 minutes. These variations could potentially have been attributed to the condition of the liver or more rapid tissue contraction, which was not evaluated [112].

There were certain limitations to our study. First, the cooled monopole and dual-slot antennas were fabricated by hand, limiting tolerances to 1 mm and producing some variation between antennas. However, such variations were not likely to influence the treatment more than variations between tissue properties, perfusion rates and placement locations. Secondly, the ex-vivo and in-vivo tissue often had vasculature that disrupted the shape of the ablation zone. Microwave energy is capable of overcoming large vascular heat sinks and expanding the ablation zone through extreme vessel heating, adding variability to our ablation geometry measurements [37]. Third, our in-vivo studies were limited in that they were not performed in a tumor-specific model, which would have a different vasculature density as well as different thermal and electrical properties. However, tumor models for large animals are not widely available or feasible for such characterization studies. Lastly, our in-vivo data were limited to a single power setting. Preliminary testing at 50 W created ablation zones that were highly susceptible to the effect of perfusion and not useful for antenna characterization. Using higher powers could potentially add further detail toward the performance of the two antennas.

4.6 Conclusion

In conclusion, the cooled dual-slot antenna created more spherical ablation zones compared to those of a cooled monopole in both ex-vivo and in-vivo liver models. The ablation zones of both antennas became more elongated at higher powers and longer treatment times. Intra-procedural CT studies utilizing a threshold function to observe the ablation zone growth was not consistent with the gross pathology. Further refinement with this method of observing ablation growth under non-contrast CT is required in order to obtain more consistent monitoring. Intra-procedural studies revealed a distinct hypodense region of vapor that was unique to each antenna design, demonstrating different rates of volumetric ablation growth between the monopole and dual-slot. This vaporization pattern can potentially be used to characterize microwave antenna performance. Differences between antenna designs may gradually diminish when increasing power or treatment duration. Adjusting the power delivery algorithm may more fully exploit the theoretical advantages of specific antenna designs.

Chapter 5

Flow-Dependent Vascular Heat Transfer during Microwave Ablation

5.1 Abstract

Microwave tumor ablation is an attractive option for thermal ablation because of its improved heating capabilities over radiofrequency ablation (RFA) in the treatment of solid tumors such as hepatocellular carcinoma (HCC). Microwave energy heats tissue to higher temperatures and at faster rates than RFA, creating larger, more homogenous ablation zones. While reducing the rate for recurrence, high-powered microwave ablation systems may also cause vascular damage.

In this study, we investigate microwave heating near large vasculature using coupled fluid-flow and thermal analysis. Numerical modeling techniques were used to predict the change in heat transfer as a function of blood flow. Experimental blood viscosity measurements were made at cytotoxic temperatures to evaluate their contribution to blood flow velocity. Validation with temperature probes lining a membrane vessel encased in phantom agar gel was used to simulate the numerical setup and confirm heat transfer.

Low-flow conditions were predicted to be more likely to cause cytotoxic heating and, therefore, vessel thrombosis and endothelial damage of downstream tissues. Such conditions may be more prevalent in patient with severe cirrhosis or compromised blood flow. High-flow conditions create the more familiar heat-sink effect that can protect perivascular tissues from the intended thermal damage. These results may help guide placement and use of microwave ablation technologies in future studies.

5.2 Introduction

Thermal tumor ablation has emerged as a viable treatment option for patients who are ineligible for surgery or have unresectable solid tumors [151]. Ablation

procedures can be performed percutaneously and are associated with less bleeding, quicker recovery and virtually no scarring compared to surgery. The primary approach of ablative therapies is to create enough thermal stress to cause cellular necrosis. Immediate cell death occurs when tissue temperatures reach 52°C, while temperatures from 43-52°C can cause cell death when maintained for longer periods of time [162].

Radiofrequency (RF) electrical current remains the most widely used heat generation source for thermal ablation. However, RF ablation is a self-limiting process since ablative temperatures lead to water vaporization and dehydration, which in turn increase impedance to electrical current flow [163]. Such limited heating also makes RF ablation susceptible to the "heat sink" effect of nearby blood vessels [44]. Large vascular heat sinks cause suboptimal perivascular heating and increased risk for tumor recurrence in patients undergoing RF ablation [164]. Microwave energy, on the other hand, propagates through all types of non-metallic material, including the dehydrated, charred and desiccated tissues associated with thermal ablation zones. As a result, continuous powers can be applied during microwave ablation, leading to larger and more complete ablation zones compared to RFA [151].

A consequence of using continuous high powers, however, is the possibility of transferring energy through nearby vessels during an ablation procedure. Microwave heating has been shown to be capable of overcoming vascular heat sinks, but little is known about how microwaves transfer heat into the nearby vasculature. Therefore, there is concern that very high powers could lead to greater risk of vascular damage and subsequent complications (**Figure 5.1A and 5.1B**). Concerns of vascular thrombus following RF ablation procedures were limited because of their low incidence and tendency to self-resolve over time [37]. As a result, there have only been a few studies looking at the theoretical heat transfer of thermal ablations

[8]. However, with the recent development of microwave ablation, there have already been reports of thermal damage in peri- and intravascular areas outside of the ablation zone, leading to portal vein thrombosis [123]. Portal vein thrombosis and associated elevated portal vein pressure are linked with high risks of variceal bleeding and decreased liver perfusion, which can be life-threatening for patients already suffering from compromised liver reserves. As more clinical centers worldwide adopt microwave ablation technology, and treatment approach becomes more aggressive, improved understanding of vascular heat transfer is necessary.

An additional factor that comes into play of heat transfer near blood vessels is the role of temperature on blood properties and its subsequent effect on blood velocity. The physical properties of blood are derived from the fluid mechanics of plasma and its cellular components, namely red blood cells. Blood is a non-Newtonian, shear-thinning fluid, meaning its viscosity decreases as the shear rate increases. While hematocrit level is the main determinant of blood viscosity, temperature can also play a role in changing blood viscosity [165]. Plasma fibrinogen levels have been shown to be activated in higher temperatures[166]. In present literature the role of temperature on blood viscosity has been established, but mostly in relation to cold agglutination (< 30 °C). There is almost no data detailing the effect of high temperatures, namely in the ranges found in microwave ablations, on blood viscosity. When correlating the effect of velocity on heat transfer in blood vessels, recognizing the potential effect of temperature-dependent blood viscosity is critical.

In this study, we employ finite-element modeling to investigate the potential of cytotoxic heat transfer in blood vessels near high-temperature ablation zones. Temperature-dependent blood viscosity was measured on heparinized porcine blood in order to confirm that blood flow continues to behave as a Newtonian fluid under cytotoxic temperatures. Numerical simulations were validated in a

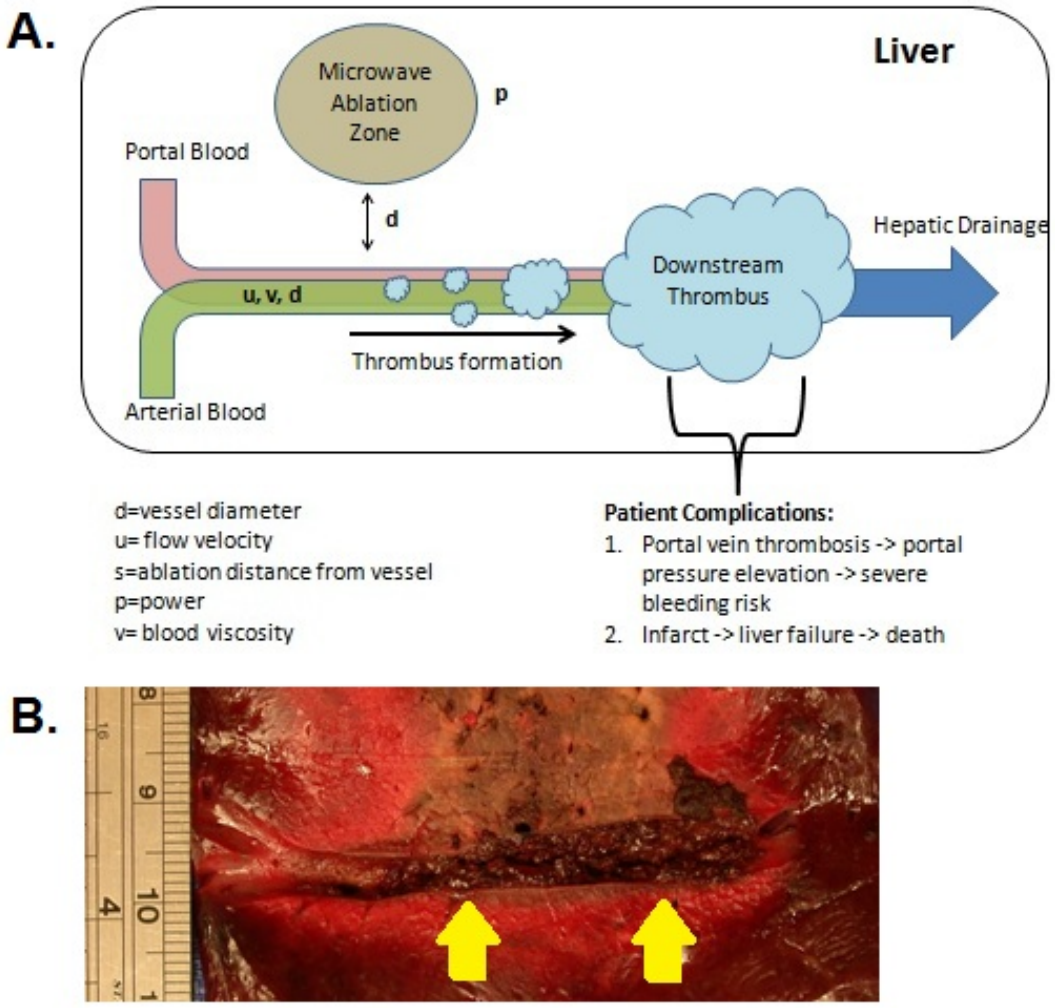

Figure 5.1: Model Setup A) Heat transfer from the MWA can occur between the tissue and nearby blood vessels. Local thrombus formation in the smaller vessels can be dislodged and travel to occlude larger vessel downstream from the ablation site. B) Thrombosed vessel from an in-vivo porcine model using three microwave antennas

phantom vessel model and used to identify conditions that favor vascular damage or thrombosis.

5.3 Materials and Methods

5.3.1 Numerical Modeling Setup

We utilized the finite-element software COMSOL (v3.5) to generate a model that coupled heat transfer with fluid flow analysis. Our geometry was set up in a three-dimensional domain with a heat source placed 1-3 cm away from a liver-embedded blood vessel of 1 cm diameter. Liver tissue properties were taken from available literature [99]. We utilized the incompressible Navier-Stokes model to simulate the laminar flow conditions inside a blood vessel. The relation of the aforementioned variables in a vessel is as follows:

$$\rho\frac{\partial u}{\partial t} + \rho(u \cdot \nabla)u = \nabla \cdot [-\rho l + \eta(\nabla u + (\nabla u)^T)] \tag{5.1}$$

$$\nabla \cdot u = 0 \tag{5.2}$$

Variable η is the dynamic viscosity of the blood and velocity u is the dependent variable which is then inserted into the conduction-convection equation as an input. We assumed blood to be a Newtonian fluid with no temperature-dependence in order to simplify the computation. This is a valid assumption at ablation temperatures since blood viscosity converges to a steady-state value at above-physiological temperatures. To model the thermal energy propagation through the tissue and vessel in from the ablation zone, we utilized the heat equation,

$$\rho C_\rho \frac{\partial T}{\partial t} + \nabla \cdot (-k_t \nabla T) = Q - \rho C_\rho u \cdot \nabla T \tag{5.3}$$

The variable ρ is the density, C_ρ is the heat capacity, Q is the heat source and u is the velocity. The heat source Q is given in W/m^3 and empirically determined beforehand to match up with the heating powers associated with microwave appli-

cator probes. In this case, we used 107 W/m^3, which provided a heating pattern similar to that created by a monopole microwave applicator delivering 50 watts of power for 2 minutes.

To observe the effect ablation spacing, we first varied the distance of the heating source from the vessel from 1 cm to 3cm. Temperature profiles along the vessel were calculated and compared to each other. To observe the effect of flow velocity, we varied the velocity from 1 mm/sec to 1000 mm/sec on a logarithmic scale. These values encompass all possible flow ranges seen in healthy and diseased liver vasculatures of the portal-venous system [167]. Temperature profiles in a spatial domain were determined and a cytotoxic damage zone was determined by highlighting the 53°C isotherm shell, which was associated with immediate cytotoxicity.

5.3.2 Blood Viscosity Measurements

A blood sample drawn from a healthy pig into a 500 mL hepatinized bag. A temperature-controlled rotational rheometer (MCR302, Anton Paar, Austria) was used to make the viscosity measurements. Whole blood viscosity η was measured under six chosen shear rates (1 , 10, 20, 50 and 100 s^{-1}) while the blood was simultaneously heated form 40 - 65 °C in 5 °C intervals. The range of shear rates were chosen to represent the slower flowing blood found in portal/hepatic veins and the faster flowing arterial flow in hepatic arteries [168]. The temperature range was chosen to reflect what woule be seen in a blood vessel near a microwave ablation zone before immediate clotting would occur.

5.3.3 Experimental Validation

An agar phantom model was used to validate the numerical modeling while introducing complexities that reflect a more clinical environment. An agar vessel phantom had advantages over ex-vivo tissue in that it was homogenous and devoid of vessels with complex geometries. Furthermore, our agar vessel was semi-transparent, which facilitated precise antenna placement. Lastly, the agar vessel phantom was reproducible and could reliably create an idealized environment for comparisons with simulations. A clinical microwave ablation system (Neuwave Medical, USA) was used to create an ablation zone 1 cm away from the vessel in the transverse direction. Fiber-optic temperature probes (Neoptix, Canada) were inserted inside the vessel to line up ipsilaterally with the ablation probe. The position inside the vessel allowed us to more accurately measure the heat transfer from the ablation zone. The vessel phantom on one end was connected to a flow pump (Masterflex, USA) to deliver fluid through the vessel. Our computational model assumed a Newtonian fluid input and thus we chose to use water for validation purposes. The flow pump was set to deliver blood at rates associated with cytotoxic heat transfer found in our numerical models.

The ablations were made at 50 W for 5 minutes and temperatures were recorded real-time at a rate of 1 Hz during the entire ablation period at 0, 2, 4 and 6 cm downstream from the ablation zone. A 1 cm vessel diameter was selected to accommodate the temperature probes without disrupting the fluid flow during the ablation.

5.4 Results

5.4.1 Numerical Modeling Results

The numerical models predicted decreased heating along the vessels at all velocities when the heating source was moved from 1 cm to 3 cm away from the vessel (**Figure 5.2A**). Placing the applicator further away from the vessel was more effective in decreasing the temperature distribution as the vessel velocities became slower. At a velocity of 0 mm/sec, 1 mm/sec and 5 mm/sec, there was a drop in max temperature from 119°C to 57°C, 76°C to 48°C and 50°C to 40°C, respectively. There was also a decrease in downstream heating as the applicator was moved further away. With the applicator placed 1 cm from the vessel, the 1 mm/sec blood velocity carried heat higher than 53°C, where immediate cytotoxicity occurs, up to 5 cm downstream of the heating source. With the 3 cm spacing, under the same blood velocity, the temperature does not rise higher than 53°C at any point past the heating source. With respect to blood velocity, the model demonstrated a negative correlation between flow rates and downstream heating. However, this correlation did not hold at the null velocity, where there was virtually no downstream heating past the applicator. In this no-flow condition, the ablation zone was confined only to the treatment region by conductive heat transfer. In the low-flow conditions (1-5 mm/sec), significant downstream heating occurred, with temperatures rising above 53°C up to 5 cm past the heating source. As we move to faster velocities (5-10 mm/sec), there is less heat being carried downstream and temperature does not rise substantially over that of a normal vessel (**Figure 5.2B**). At these faster velocities, the heat distribution behaved similarly to that of a vessel acting as a heat sink. This pattern suggests that the flow is fast enough to dissipate energy over long distances rather than local heating downstream tissues.

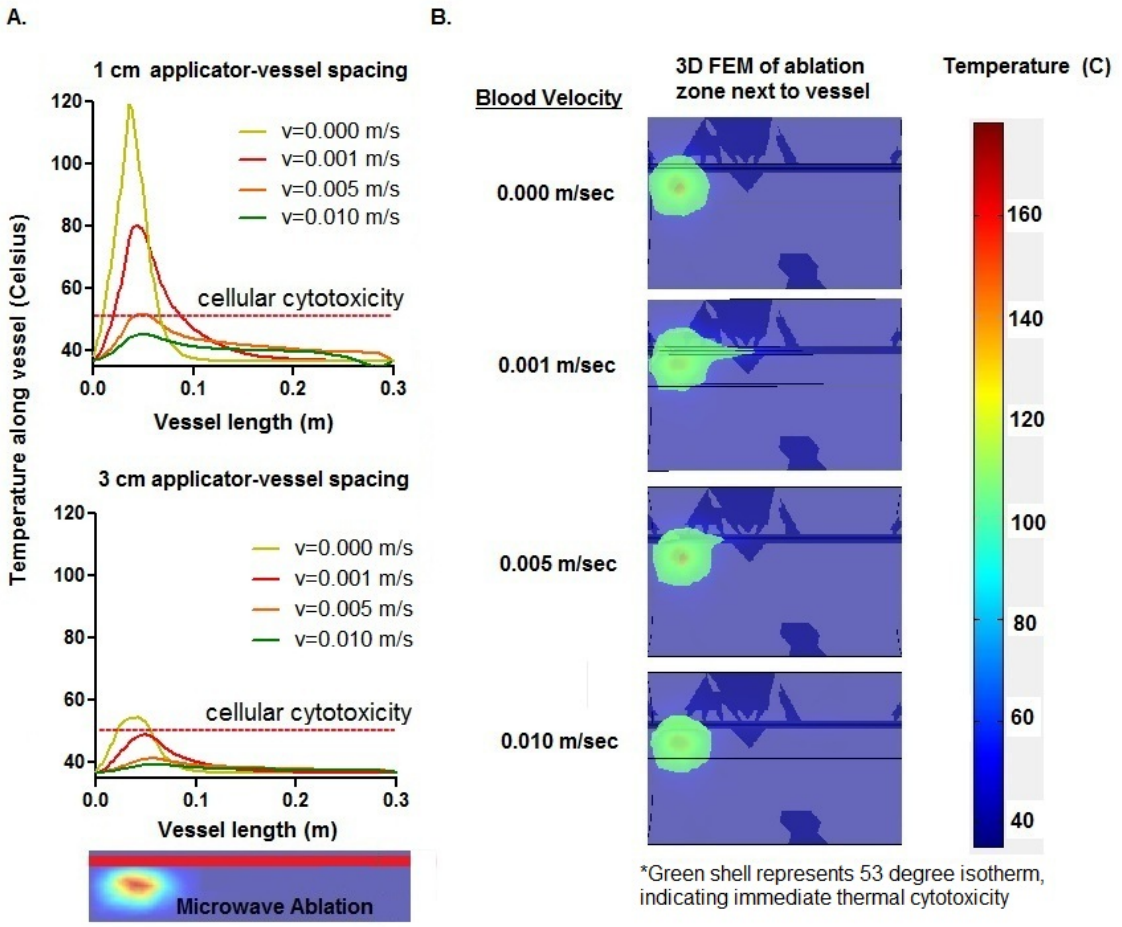

Figure 5.2: Computational Results A) Numerical modeling depicts decreased heat transfer while increasing vessel-antenna spacing from 1 cm to 3 cm. B) Temperature map of ablation at different velocities, with the 53°C isotherm highlighted to indicate location of immediate cellular necrosis. Increasing blood velocity is associated with a decrease in intravascular heat transfer near ablation zones.

5.4.2 Blood Viscosity Measurements

Temperature-dependent viscosity results are shown in Figure 5.3. Heparinized blood viscosity exhibited only minimal changes as temperature increased, with mean viscosity ranging from 0.002-0.005 (Pa·s) as temperatures reached 65 °C. These trends held for shear rates found in low-flow (venous) and high-flow (arterial) environments. Blood viscosity changes were more dramatic at sub-physiological

shear rates (1 s^{-1}), where there was a 3-fold rise in viscosity as temperatures reached 65 °C.

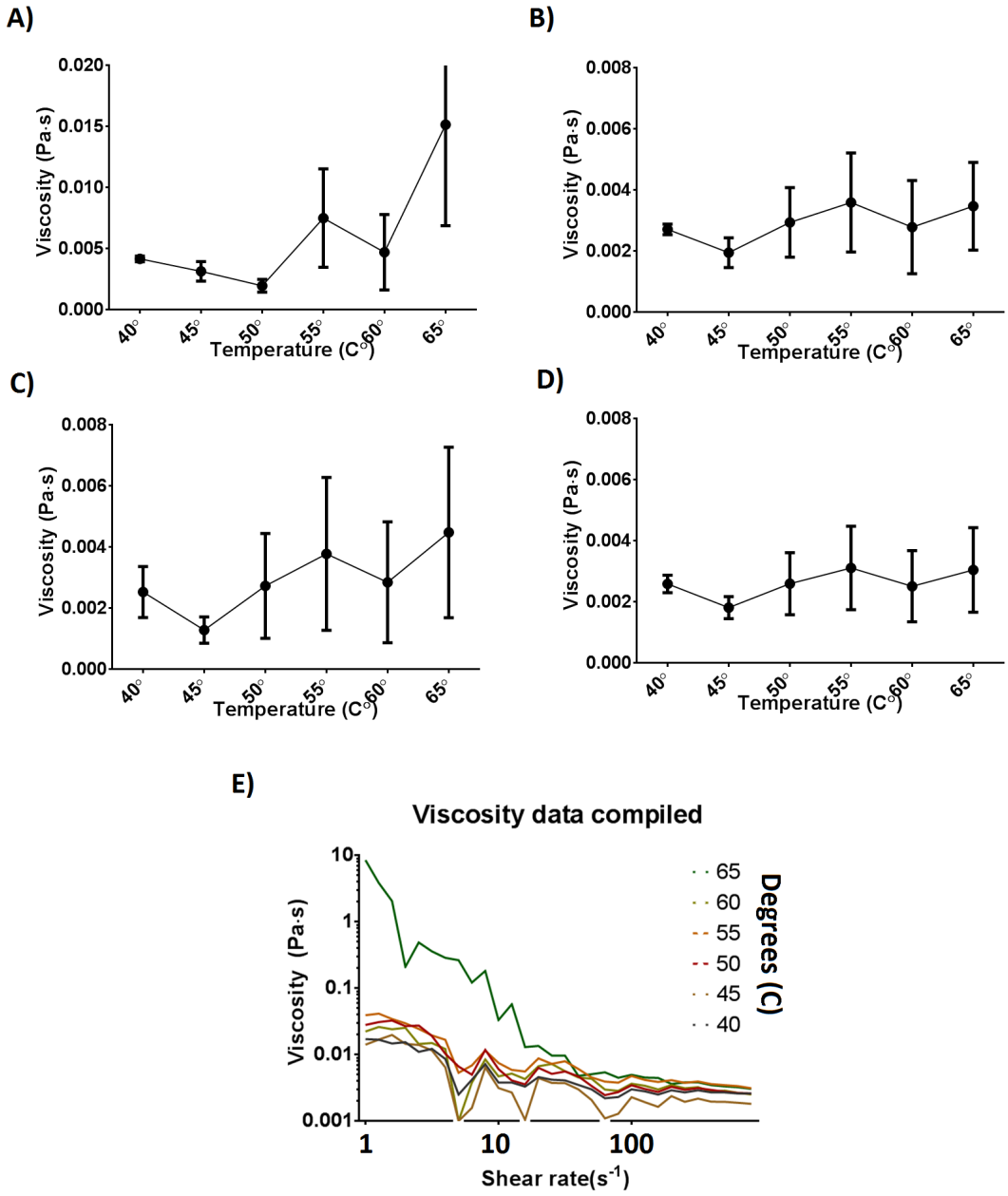

Figure 5.3: Temperature-dependent blood viscosity measurements. Blood viscosity was measured against changing temperature at A) 1 , B) 10 , C) 50 ,and D) 100 s^{-1} A summary of the measurements is depicted in E). At physiological shear rates ($>10s^{-1}$), there are only slight changes in viscosity with respect to temperature.

5.4.3 Experimental Validation Results

The temperature trends in the phantom validation were similar to those found in the computational simulations (**Figure 5.4**). At higher blood velocities (11-14 mm/sec), there was no appreciable rise in temperature along the vessel (6 cm). However, once a lower velocity was reached (3 mm/sec), there was a significant increase in temperature inside the vessel as the energy deposit started accumulating. At this lower velocity, the temperature was significantly higher compared to the other 3 velocities at locations 4 and 6 cm downstream from the heating zone ($p<0.05$ at 4 cm, $p<0.02$ at 6 cm). There was no significant difference in temperature elevations converged as we moved closer and closer to the actual ablation probe location, which was expected from the volumetric heating associated with microwave antennas.

5.5 Discussion

This study investigated the risk of vascular damage during microwave thermal ablation. As expected, vascular heating decreased as distance between the vessel and thermal source increased, regardless of fluid velocity. This suggests that distant microwave antenna placement is a feasible way to reduce the risk of vascular heating, downstream damage and thrombosis during microwave tumor ablation.

We noted a rapid increase in cytotoxic heat transfer in vessels with decreased perfusion, notably at velocities of 7 mm/s or less. At higher velocities, the thermal heat transfer occurs too rapidly for localized temperature elevations. The phantom vessel modeling results confirmed significant temperature elevations found in the numerical modeling study. This finding is potentially relevant for potential ablation patients, notably those who suffer from pre-existing cirrhotic livers and poor vascular flow. These implications suggest that characterization of nearby vessel size and

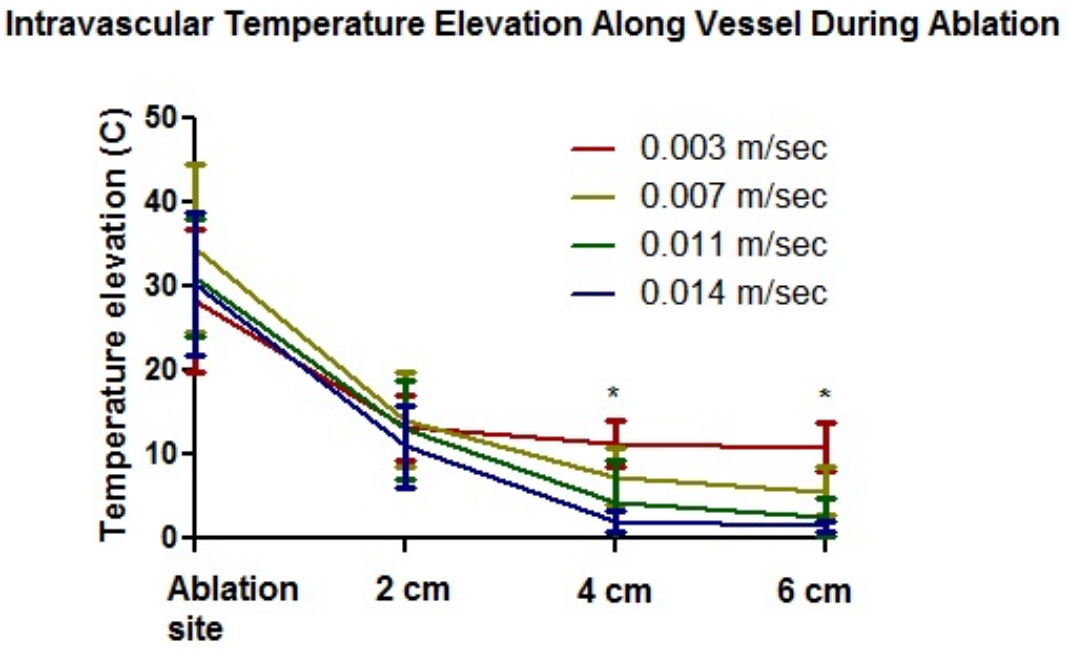

Figure 5.4: Phantom modeling results (n=6) demonstrating significantly higher temperature elevation ($p<0.05$) at 0.003 m/sec compared to all other perfusion rates at vessel locations 4-6 cm downstream from the ablation zone.

blood flow should be taken into account during the treatment planning stage. The scale-invariant nature of the Navier Stokes equations imply that the computational results can be translatable to various vessel sizes and flow velocities associated with a variety of patient profiles during an ablation procedure.

The velocities encountered in these simulations and models are considered low, even for the smaller vasculature in a cirrhotic liver. This discrepancy suggests that there are perhaps other velocity-dependent factors involved in the heat transfer process beyond simple conduction-convection. One possibility is the formation of water vapor inside the vessel from surrounding tissue, which has been seen in ex-vivo and in-vivo ablation studies. Efforts to account for water vapor formation inside

heated vessels have been investigated previously and can potentially be coupled to our numerical models to predict heat transfer in a more clinically realistic scenario [103, 107].

Blood viscosity was found to not change dramatically with respect to cytotoxic temperatures at physiological shear rates. With relatively constant viscosity, it is possible to infer that there is not a significant change in blood viscosity during heating and its effect on blood velocity is minimal. Sub-physiological shear rates, found in patients with cirrhosis or congestive heart failure, can potentially lead to higher viscosities at temperatures related to ablations. The subsequent effect of high viscosity on blood flow velocity is currently unknown and requires further investigation.

Assessing the performance of our numerical modeling in predicting clinical thrombotic risk is critical. However, there are aspects that have not yet been integrated into the numerical model, such as the tortuous vessel geometries encountered in liver anatomy. Furthermore, we utilized heparinized blood to evaluate temperature-dependent blood viscosity. By inactivating a component of the clotting pathway, it is difficult to conclusively declare that blood viscosity does not experience dramatic changes with high temperatures. The phantom vessel model offered an idealized vessel geometry that could validate our simplified numerical model. We added additional complexities such as utilizing a clinical microwave ablation system but recognize that there are still gaps between our numerical/phantom model and the clinical scenario. THe similarities in trend and temperature elevation between the numerical and phantom modeling suggests that our numerical modeling is a viable starting point to creating a thrombotic risk model. Integrating more complexities into our numerical models may provide more accuracy and clinical utility for future studies.

5.6 Conclusion

Creating ablation zones near vessels with slow blood flow can potentially increase the risk of vascular damage and thrombosis. Further investigation to determine the optimal placement of the microwave antennas to nearby blood vessels appears warranted, and may guide treatment planning in future studies.

Chapter 6

Predictors of Thrombosis in Hepatic Vasculature during Microwave Ablation in an In-Vivo Porcine Model

6.1 Abstract

Purpose: The goal of this study was to evaluate and model the risk of in-vivo thrombosis in each hepatic vessel type during hepatic microwave ablation as a function of vessel size, velocity and vessel-antenna spacing.

Materials and Methods: Animal care and use committee approval was obtained prior to in-vivo studies. A single microwave ablation antenna was inserted into a single porcine lobe (n=15 total) adjacent to a hepatic artery, hepatic vein, or portal vein branch. Conventional and Doppler ultrasound were used to measure the vessel size (1-13 mm), blood flow velocity (5-200 cm/sec) and vessel-antenna spacing (1-30 mm). A microwave ablation zone was then created at 100 W for 5 minutes. Thrombus formation was evaluated on immediate post-procedure ultrasound imaging. Logistic regression was used to evaluate the predictive value of vessel size, blood flow velocity and vessel-antenna spacing on vascular thrombosis.

Results: Thrombosis was identified in 53.3% of portal veins (8/15), 13.3% of hepatic veins (2/15) and 0.0% of the hepatic arteries (0/15). The average peak blood flow rate of the hepatic artery (106.3 $\pm$ 27.2 cm/sec) was significantly greater than that of the hepatic vein (24.0 $\pm$ 8.9 cm/sec; $p<0.0001$) and portal vein (15.6 $\pm$ 9.0 cm/sec; $p<0.0001$). Peak blood flow velocities less than 12.45 cm/sec, vessel diameters less than 5.10 mm and vessel-antenna spacings less than 3.75 mm were strong predictors of hepatic vein thrombosis. However, these individual factors were not predictive of the more common portal vein thrombosis.

Conclusions: Portal vein thrombosis was more common than hepatic vein thrombosis during microwave ablation treatments, but was not as predictable based upon vessel size, flow velocities, or vessel-antenna spacing alone. Larger hepatic arteries do not appear to be at significant risk for thrombosis during microwave ablation

procedures, likely due to their high peak velocity.

6.2 Introduction

Image-guided thermal tumor ablation is a promising treatment modality for early stage hepatocellular carcinoma and hepatic metastases [78, 169, 170]. Radiofrequency ablation is currently the most widely-used modality for thermal ablations in the liver, with several series demonstrating nearly equivalent survival outcomes compared to resection in terms of overall survival rates [26, 27, 171, 172]. In both prospective and retrospective studies, radiofrequency ablation was associated with lower hospital expenses, fewer complications and faster recovery [173]. However, radiofrequency ablation has been plagued by higher rates of local tumor progression compared to resection [26, 27, 172]. The most significant predictors of local tumor progression are tumor size greater than 3 cm, insufficient ablation margin, and proximity to blood vessels larger than 3 mm in diameter [150, 174-176]. In particular, radiofrequency ablation is highly susceptible to the so-called "heat-sink effect," where blood vessels and tissue perfusion decrease tissue heating, potentially limiting tumor cell death in perivascular regions [128, 174, 177, 178]. This problem is exacerbated by the fact that RF heating is self-limited by the poor electrical conduction of tissue once heated to the point of desiccation or charring [139, 174].

Microwave ablation systems have been shown to more effectively heat a spectrum of biological tissues by utilizing an alternating electric field rather than an electrical current [139]. Multiple studies have demonstrated the ability of microwave ablation to deposit energy into tissue at a higher rate than radiofrequency ablation systems [40, 44, 180, 181]. As a result, microwave ablations created with modern high-powered systems can be larger, form more rapidly, are more reproducible, and

more capable of overcoming the heat-sink effect associated with vascular blood flow compared to RF ablations [38, 140, 181]. However, the greater heating rates can have negative consequences due to the potential for clinically relevant thrombosis of non-targeted vessels [123, 132].

Acute thrombosis of small hepatic vessels from radiofrequency ablation has traditionally been considered rare and self-resolving, and is usually only a minor complication [39, 182, 183] However, with greater heating rates and more continuous energy delivery during microwave ablation, the potential to cause thrombosis to larger vessels resulting in compromised hepatic function may be increased. Hepatic vascular thrombosis in clinical and in-vivo microwave studies has already been reported, but not systematically studied [123, 132, 184]. A better understanding of the risk factors for microwave ablation-induced thrombosis is needed to help guide the clinical application of these more powerful ablation devices.

The goal of this study was to evaluate and model the risk of thrombosis in portal veins, hepatic veins, and hepatic arteries during microwave ablation as a function of vessel size, velocity and vessel-antenna spacing.

6.3 Materials and Methods

All studies were performed under approval from our institutional animal care and use committee and complied with National Research Council guidelines [159]. Female domestic swine (n=6, mean weight=70kg); (Arlington Farms, Arlington WI) were sedated with intramuscular tiletamine hydrochloride-zolazepam hydrochloride (7 mg/kg, Telazol, Fort Dodge IA) and xylazine hydrochloride (2.2 mg/kg, Xyla-Ject, Phoenix Pharmaceutical, St Joseph, MO). Anesthesia was maintained with inhaled 1.0-2.0% isofluorane (Halocarbon Laboratories, River Edge, NJ). An ear vein

was cannulated with a 20-gauge angiocatheter for administration of IV fluids.

Microwave ablations (n=15) were performed under ultrasound guidance with a single microwave antenna (LK-15; Neuwave Medical, Inc., Madison WI). Conventional and Doppler ultrasound (Siemens Antares, Siemens Medical Solutions Inc., Issaquah, WA) were used before and after the ablations to determine the diameter, size and blood flow velocity (peak and temporal pattern of flow) of the nearest hepatic artery, hepatic vein and portal vein with a 5 MHz center-frequency linear transducer (VFX 13-5, Siemens Healthcare, Ultrasound Group, Issaquah, WA) (**Figure 6.1**). Thrombosis of a vessel was defined as loss of Doppler flow within the vessel lumen and was generally associated with hypo-echoic thrombus identified on the grey-scale imaging. Thrombus formation was defined as a binary event, either categorized as present (**Figure 6.2**)

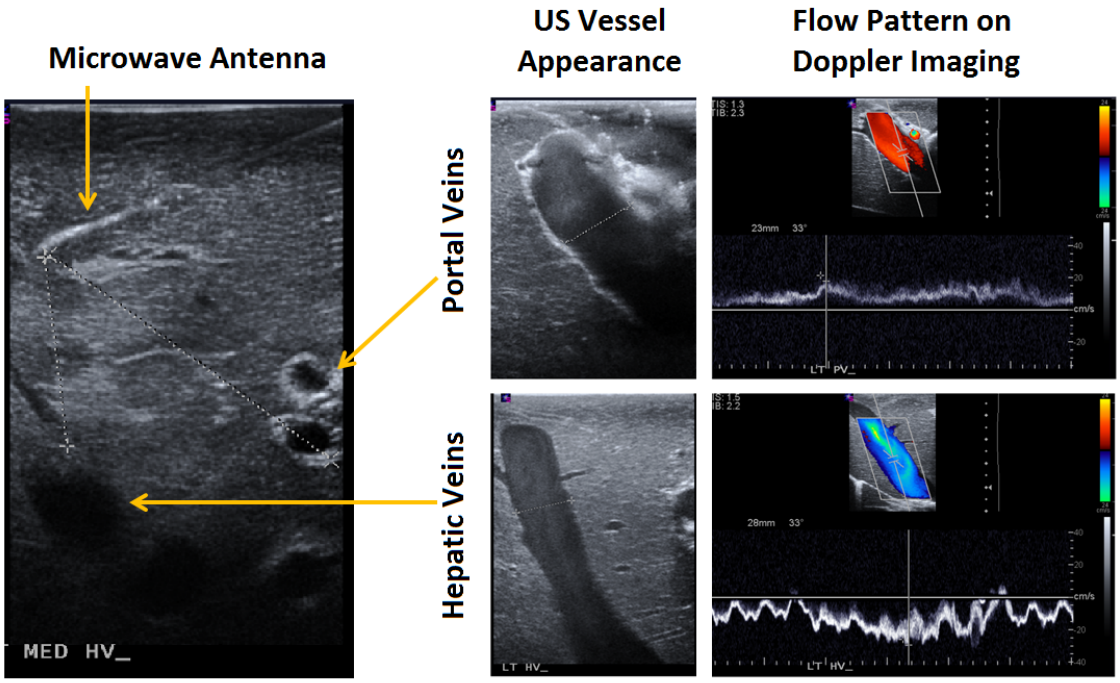

Figure 6.1: Experimental setup of a microwave antenna positioned in the proximity of portal veins and hepatic veins with corresponding ultrasound and Doppler measurement. Portal vein walls, comprised of loosely-packed connective tissue, appear hyperechoic under ultrasound imaging. Hepatic vein walls, comprised of tightly-packed collagen fibers, was characterized by the absence of echogenic artifacts. On Doppler, hepatic vein blood flow is more pulsatile due to anterograde-retrograde pressure/flow variations from the cardiac cycle. Conversely, portal vein blood move anterograde toward hepatic sinusoids, greatly dampening the flow.

After ablation, animals were sacrificed with an IV injection of Beuthanasia-D (390 mgmL, pentobarbital sodium and 50 mg/mL phenytoin sodium at 0.2 mL/kg; Schering-Plough, Kenilworth, NJ). The liver was removed and sectioned along the axis of each antenna to confirm the location of the ablation zone near the targeted vessels.

6.3.1 Statistical Analysis

Differences in mean diameter, peak velocity and spacing were identified between hepatic arteries, hepatic veins and portal veins by using a paired Student's t-test. Partial and full thrombus formation was considered a positive event, while the absence of thrombus formation was considered a negative event. With thrombus formation coded as a binary event, univariate logistic regression was used to model the rate of thrombosis as a function of the predictive variables (vessel diameter, blood flow velocity and vessel-antenna spacing) in each type of vessel. Multivariate logistic regression was also performed to account for the simultaneous effect of two or three of the variables against thrombosis formation. Receiver operator characteristic (ROC) curves and areas under the curve (AUC) were obtained for each model. Differences in AUC were assessed with DeLong and Delong tests [185]. Two-tailed p-values less than 0.05 were considered significant. Statistical analysis was performed using MedCalc v7.4 (Mariakerke, Belgium) and R v3.01 with assistance from a statistician (A.M,R)

6.4 Results

As expected, the average maximum flow rate of the hepatic artery was significantly greater than that of the hepatic vein and portal vein (106.3 $\pm$ 27.2 [mean $\pm$ 1 SD]

versus 24.0 $\pm$ 8.9 cm/sec; $p<0.0001$ and 15.6 $\pm$ 9.0 cm/sec; $p<0.0001$, respectively) (**Figure 6.3A**). The hepatic artery diameter was significantly smaller than that of the hepatic vein and portal vein (2.21 $\pm$ 0.23 versus 7.33 $\pm$ 1.93 mm; $p<0.0001$ and 7.32 $\pm$ 3.47 mm; $p<0.0001$, respectively) (**Figure 6.3B**). No differences were noted in the average spacing between the microwave antenna and hepatic arteries, hepatic veins or portal veins (21.11 $\pm$ 5.51, 17.76 $\pm$ 10.50, 20.77 $\pm$ 5.21 mm) (**Figure 6.3C**).

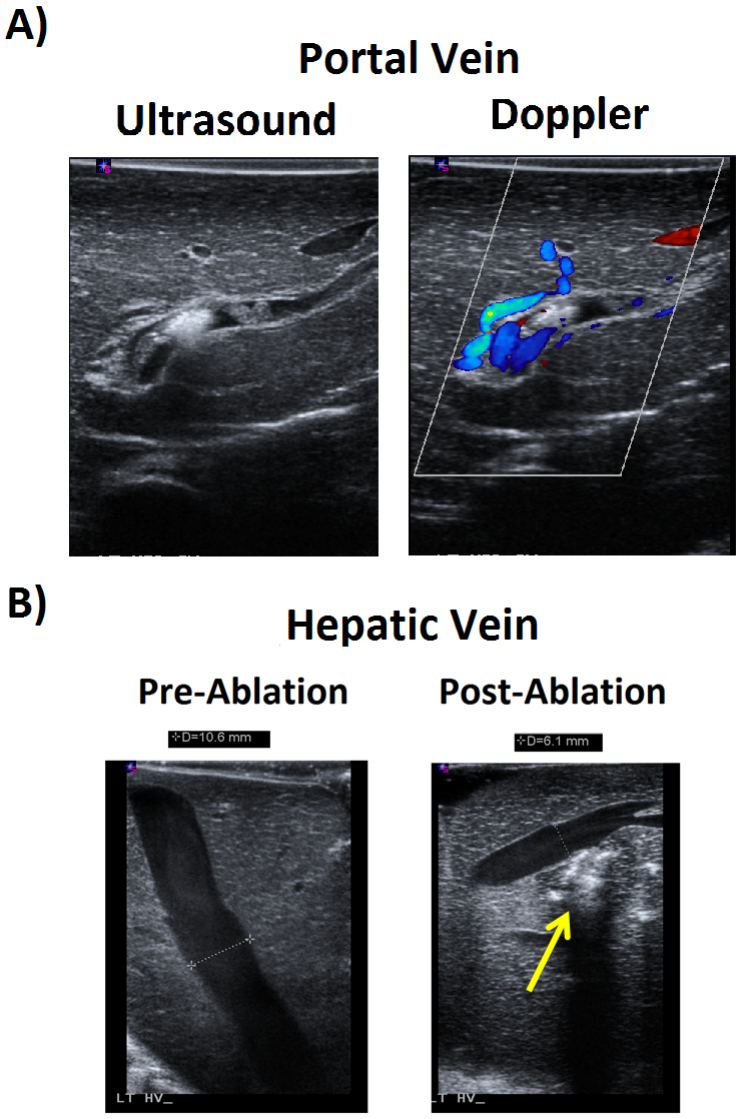

Figure 6.2: Post-ablation vessel imaging. A) Thrombus formation seen in a nearby portal vein immediately on ultrasound after the ablation procedure at 100 W for 5 minutes. Color Doppler was also performed to observe either stagnant or diverted flow around the thrombus. B) Absence of thrombus in a hepatic vein immediately before and after microwave ablation zone creation. Note the absence of thrombus in the hepatic vein, even though the ablation zone abutted the vessel wall as denoted by the hyper-echoic gas bubbles made from the ablation zone (arrow)

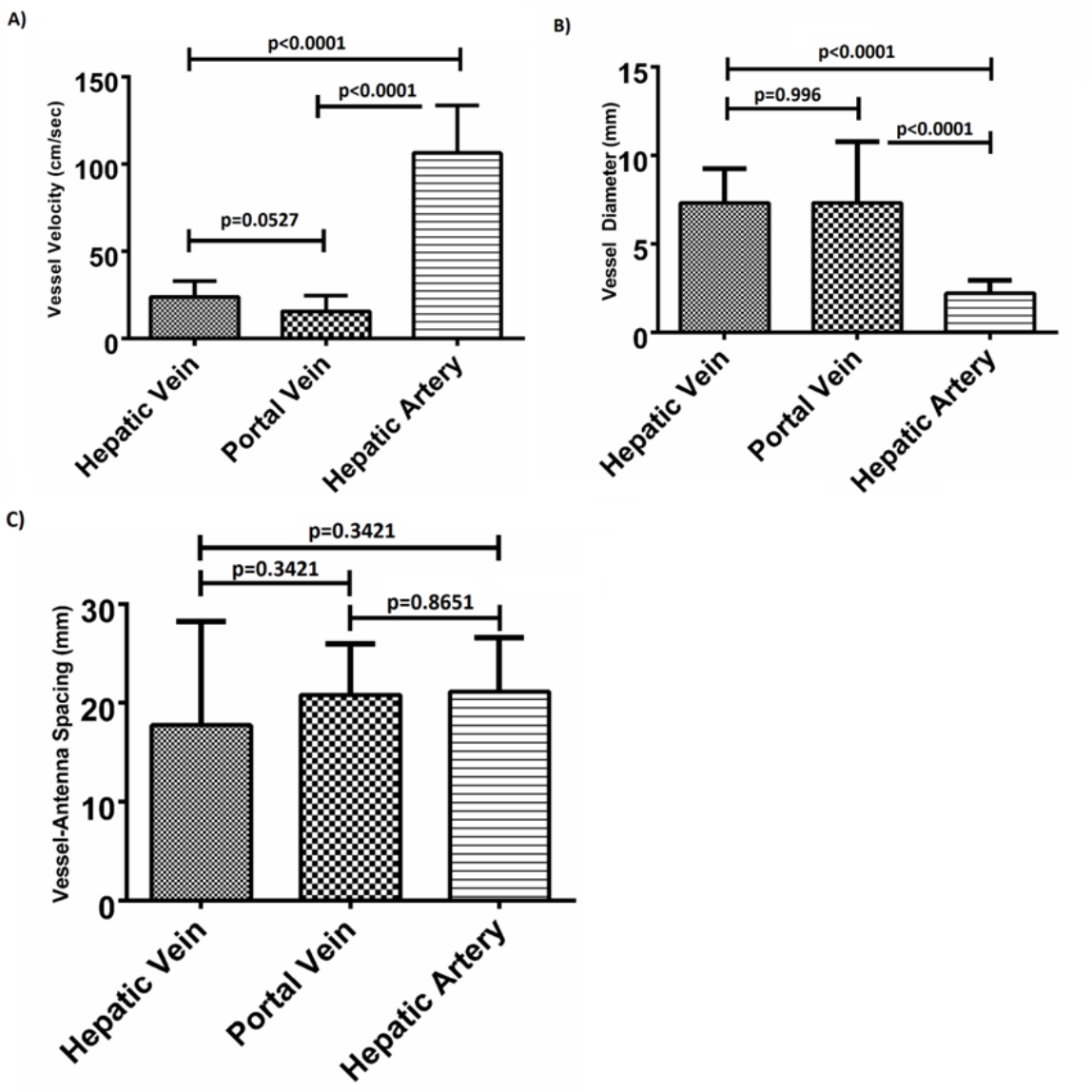

Figure 6.3: Summary of the vessels that were targeted with microwave ablations. A) Hepatic arteries had significantly faster peak velocities (106.3 cm/sec) compared to portal (24.1 cm/sec) and hepatic veins (15.6 cm/sec); B) Hepatic arteries were also significantly smaller in diameter (2.2 mm) compared to portal (7.3 mm) and hepatic veins (7.3 mm); C) There was no significant difference between any of the vessels in terms of antenna spacing (21.1 cm vs 17.8 vs 20.7 cm).

No thrombus formations were identified in any hepatic arteries but 13.3% of the hepatic veins (2/15; 1/15 partial and 1/15 full occlusions) and a 53.3% of the portal vein (8/15; 4/15 partial and 4/15 full occlusions) demonstrated thrombus formation (**Figure 6.4**).

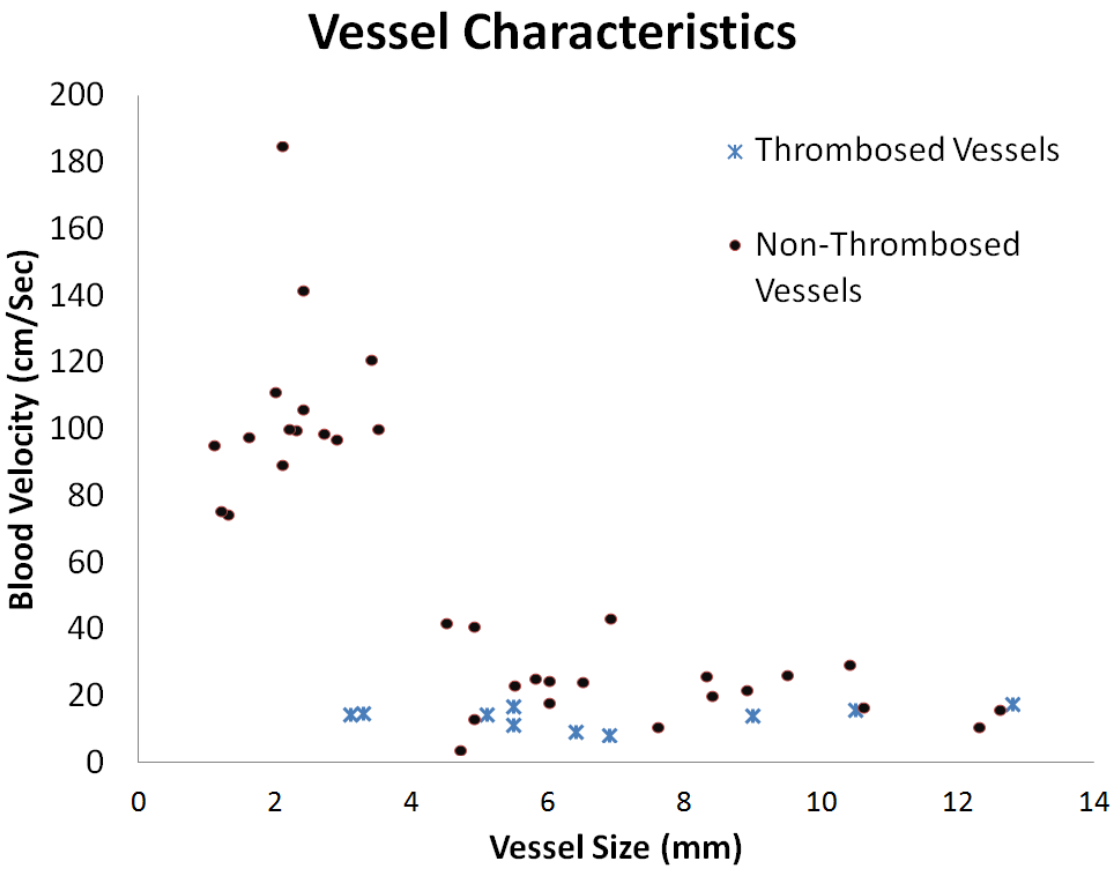

Figure 6.4: Thrombosis versus non-events as a function of vessel size and blood velocity. The cluster of points in the upper left-hand corner shows the hepatic arteries, which were small in diameter and fast in blood velocity. The rest of the data points, on the bottom portion of the chart show portal and hepatic veins, which were slower and larger on average than the hepatic arteries.

6.4.1 Hepatic Artery Analysis

Thrombosis was not seen in any hepatic arteries, despite targeting vessel sizes up to 4 mm in diameter and positioned as near as 4 mm from the microwave antenna. Due to the absence of thrombus formation, a logistic function and its corresponding ROC curve could not be created.

6.4.2 Hepatic Vein Analysis

Univariate peak velocity, vessel size and vessel-antenna spacing were found to be highly correlated with thrombus formation using logistic functions and significantly so with vessel size and vessel-antenna spacing. Specifically, faster flow, larger vessels and increased vessel-antenna spacing from microwave antennas were found to be predictive factors that made thrombus formation less likely in hepatic veins (Figure 6.5A). Likewise, slower flow, smaller vessels, and closer vessel-antenna spacing led to an increased likelihood of thrombosis. Univariate logistic regression modeling predicted a 50% chance of thrombus formation if the peak blood flow velocities less than 12.45 cm/sec, vessel diameter was less than 5.10 mm or the vessel-antenna spacing was less than 3.75 mm. The areas under the ROC curve generated from each univariate logistic function was high, indicating strong performance in separating thrombosis versus non-thrombosis in hepatic veins (Figure 6.5B). Details of the quantitative statistical metrics are outline in Table 1.

Multi-variate logistic regression, which adjusted an individual variable to account for the confounding effect of the other two variables, showed an inflated area under the ROC curve due to low sample size. Furthermore, using vessel size, blood flow velocity and vessel-antenna spacing simultaneously did not show improvements in predictive power over using the individual variables alone. Perfect

Variables	Odds Ratio	95% CI	P-Value	AUROC
Peak Velocity (cm/s)	0.773	0.529-1.128	0.083	0.885
Vessel Size (mm)	0.096	0.002-5.231	0.032	0.904
Vessel-Antenna Spacing (mm)	0.725	0.472-1.114	0.014	0.923

Table 6.1: Univariate logistic contributions from hepatic vessels. Peak velocity, vessel size and vessel-antenna spacings were found to be strong contributors to thrombus formation in hepatic veins. The large area under the ROC curve for each variable suggested strong performance in distinguishing between thrombosis and no-thrombosis in hepatic veins.

separability between events and non-events also caused unreliable estimates of standard errors, preventing further significance testing.

6.4.3 Portal Vein Analysis

In contrast to the results found for hepatic veins, peak flow velocity, vessel size and vessel-antenna spacing were not found to be significant predictors of thrombosis in portal veins. In fact, portal vein thrombosis occurred indiscriminately across peak flow velocity, vessel sizes and vessel-antenna spacings (Figure 6.6A). The area under the ROC curve of the portal vein logistic functions were significantly less than that of the hepatic veins, suggesting poor classification power of univariate peak flow velocity (Figure 6.6B). Details of the quantitative statistical metrics are outline in Table 2.

Variables	Odds Ratio	95% CI	P-Value	AUROC
Peak Velocity (cm/s)	0.942	0.788-1.085	0.264	0.607
Vessel Size (mm)	0.942	0.788-1.085	0.264	0.607
Vessel-Antenna Spacing (mm)	0.881	0.698 – 1.111	0.256	0.607

Table 6.2: Univariate logistic regression from portal vein characteristics. Peak velocity, vessel size and vessel-antenna spacings were found to be poor individual predictors of thrombus formation in portal veins. The area under the ROC curve for each variable was lower than that found in hepatic veins and indicated poor predictive value in separating thrombotic and non-thrombotic events in portal veins.

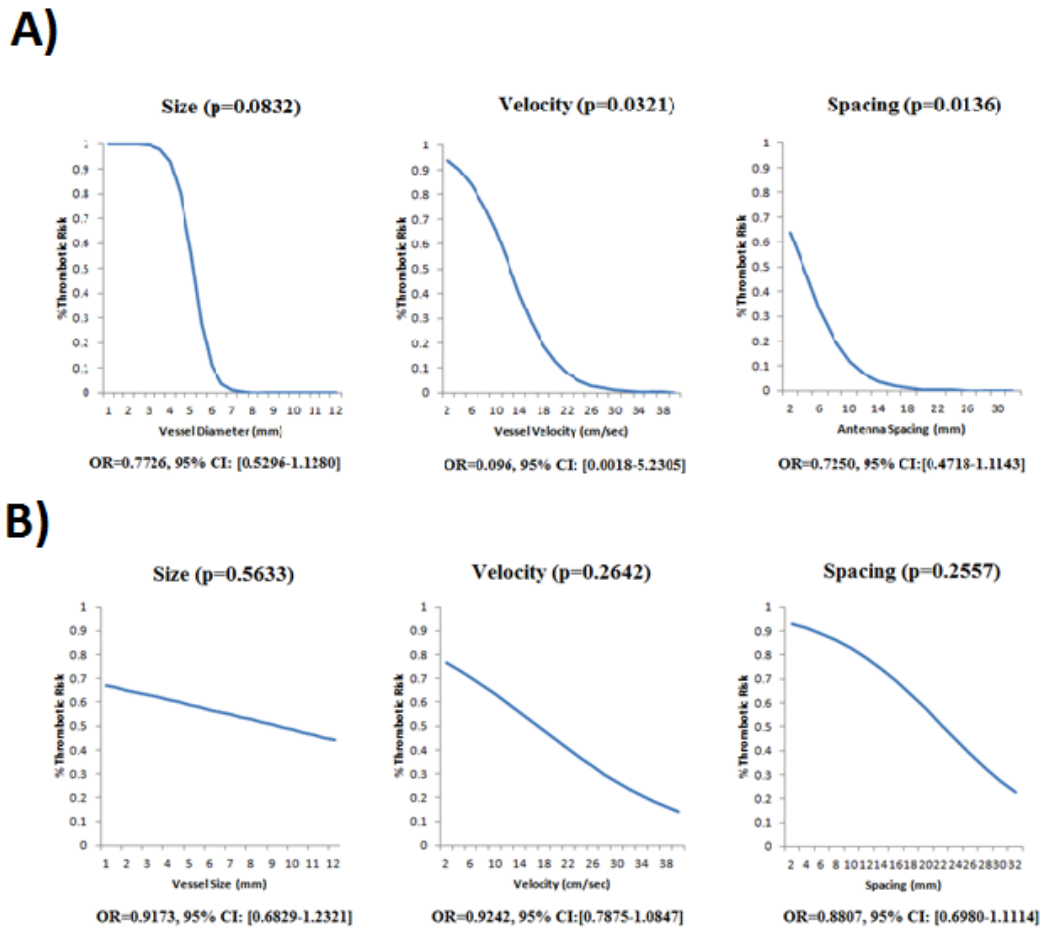

Figure 6.5: Univariate logistic functions for the hepatic and portal veins. A) Logistic regression model of hepatic veins. Vessel velocity and spacing were significantly correlated with thrombosis, while vessel size was correlated but not significant. B) Logistic regression model for portal veins. Vessel size, velocity and spacing were not significantly correlated with thrombosis.

Multi-variate logistic regression showed similarly poor contribution from each variable after accounting for the confounding effect of the other variables. However, there was a slight increase in the area under ROC curve of the multivariable portal vein analysis using vessel size and vessel-antenna spacing simultaneously, compared to that of the univariate logistic regressions. This multi-variate regres-

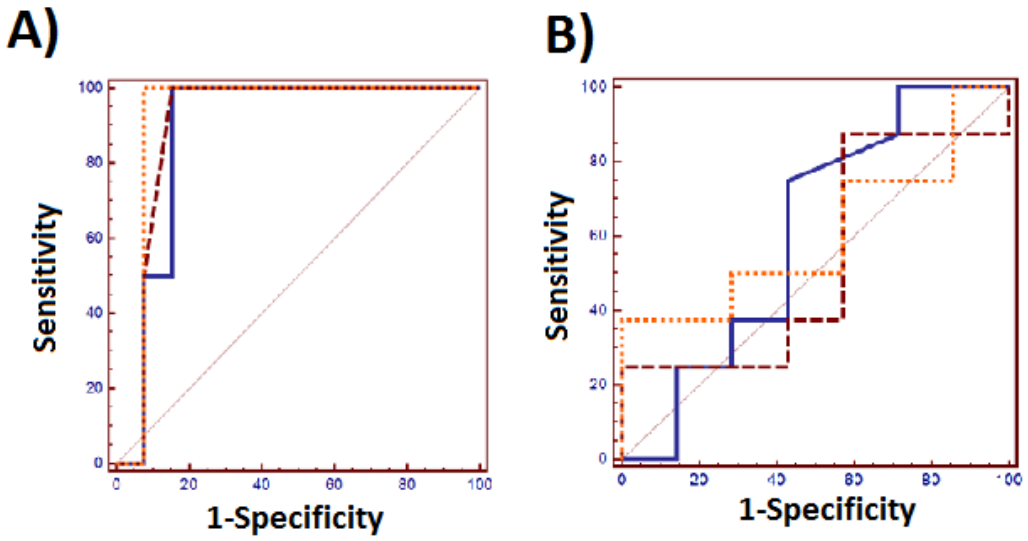

Figure 6.6: Univariate receiver operator characteristic curves for hepatic vein and portal veins. A) With a low number of thrombus events in hepatic veins, the regression model could classify thrombus formation with high sensitivity and specificity. B) The portal vein regression model was poorly discriminating, offering limited performance in separating the likelihood of a thrombotic event during an ablation procedure. The areas under the curve of each predictor were not significantly different from each other.

sion model created a combination of vessel sizes and vessel-antenna spacings that could be categorized into various thrombus formation risk categories (Figure 5E). One sample combination showed that vessels greater than 7 mm, coupled with a vessel-antenna spacing greater than 27 mm, predicted a less than 30% chance of thrombosis formation. In the vicinity of a 15 mm sized vessel, the vessel-antenna spacing can be decreased to 19 mm distance while maintaining a 30% chance of thrombosis formation. Likewise, a smaller vessel sized at 5 mm in diameter would need a vessel-antenna spacing of at least 30 mm to maintain the 30% chance of thrombosis formation. The addition of blood velocity to the multi-variate model offered only marginal improvement in the area under the ROC curve compared to the univariate velocity predictor (0.75 ± 0.13 versus 0.61 ± 0.16, p=0.48), vessel size

predictor (0.75 ± 0.13 versus 0.54 ± 0.08, p=0.17) and vessel-antenna spacing (0.75 ± 0.13 versus 0.607 ± 0.08, p=0.34).

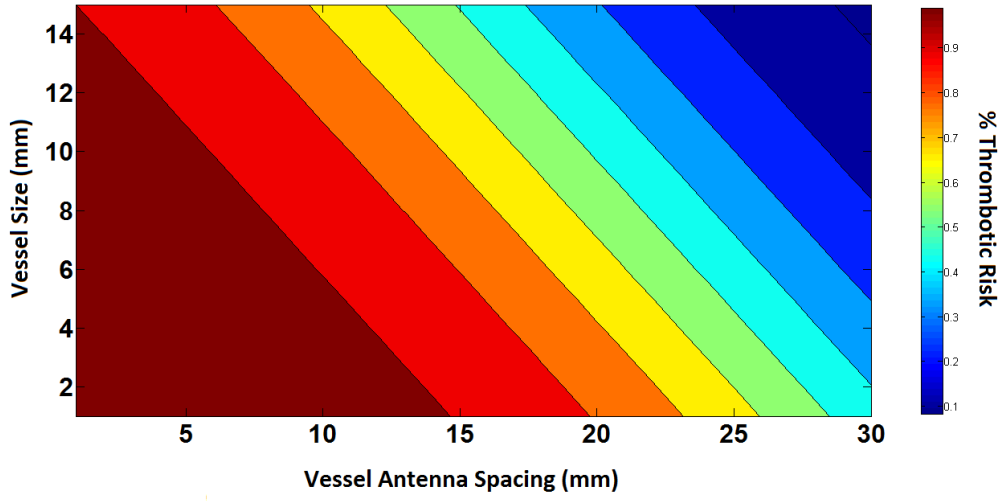

Figure 6.7: Contour mapping of the multi-variate regression model demonstrating how various combinations of vessel size and vessel-antenna spacing measurements are correlated with risk of thrombus formation in portal veins.

6.5 Discussion

This in-vivo pilot study demonstrated that vessel size, peak blood flow velocity and vessel-antenna spacing are predictive of thrombosis of hepatic veins when performing microwave ablation. In contrast, portal vein thrombosis happens at a higher rate than with hepatic veins, and was not as predictable. Using multiple variables simultaneously to predict thrombosis in portal veins had improved performance over using single variables, but the fit of the portal vein model was still poor compared to the hepatic vein model.

The primary goal of thermal ablation is to heat the target tumor and margin to cytotoxic temperatures. A significant limitation of RF ablation is that the majority

of tissue heating is related to thermal conduction. This relatively inefficient heating mechanism can be overwhelmed by vascular heat sinks – especially at the periphery of the ablation zone, resulting in incomplete treatments [186]. Microwave ablation, on the other hand, is less affected by vascular heat sinks and perfusion-mediated cooling [38, 56, 181]. As a result, clinical adoption of newer high-power microwave devices in recent years has demonstrated the potential for creating larger ablation zones at a faster rate [56, 140, 187].

The potential downside of this more powerful heating is unintended collateral damage, in this case, to the hepatic vascular structures [39]. The larger, hotter, and faster ablation zones associated with these high-powered systems has raised the concern of indiscriminate damage to hepatic vessels, particularly in cirrhotics. No incidents of hepatic arterial thrombus were identified in this study despite the close proximity of the microwave antenna to various-sized hepatic arteries. This raises the possibility of a protective effect of rapid blood flow. The results of this study suggests that an optimization strategy may be appropriate when placing microwave antennas near critical vessels, particularly in cases of slow blood flow and when tumors are located in close proximity to larger portal or hepatic veins.

The results reported in this study confirm the previously established relationship between vessel size and acute thrombosis. An early in-vivo porcine study on the effect of RF ablation on vessels found that vessels less than 3 mm in diameter had an increased risk for occlusion [174]. That study did not distinguish between portal and hepatic veins. The same group later found similar results with MW ablations, showing that vessels less than 3 mm in diameter had an increased risk for thrombosis, while larger vessels had less of a risk for thrombosis [37]. Clinical studies of hepatic RF ablation have also demonstrated the incidence of inadvertent portal vein thrombosis (0.87%; 12/1379) to occur at a higher rate than hepatic vein

thrombosis (0.29%; 4/1379) [188]. These findings are concordant with our study, albeit at lower overall rates of thrombosis. Our higher rates can be attributable to the fact that we placed antennas close to vessels in normal parenchyma, compared to the center of a tumor.

The underlying reason for the observed differences in the rate of thrombus formation and the ability to predict thrombus formation between portal and hepatic veins is not completely clear. The most likely explanation is a difference in blood flow dynamics. Specifically, the portal vein is flowing in a non-pulsatile fashion into a capillary bed (hepatic sinusoids). Thus, any thrombus, even if located intravascularly and not associated with the vessel wall, is likely to become lodged in the hepatic sinusoids, increasing resistance to forward flow. This situation would be exacerbated in portal hypertension where portal venous resistance is already increased. The result of thrombus and increased portal pressures at the sinusoidal level would eventually decrease flow velocity and subsequently increase the chances of activating the coagulation cascade. In contrast, hepatic veins experience pulsatile flow, known to decrease the likelihood of thrombus formation due to turbulence, and flow forward into progressively larger vessels and ultimately into the heart [189-191]. Thus, any hepatic venous thrombus is less likely to become established within a vessel.

There were some limitations to our study related to the in-vivo environment with a simultaneous interplay of heat transfer, blood flow and clotting. Reproducibly creating the appropriate array of vessel-antenna spacing and velocities needed to assess their relationship to thrombus formation was difficult. We did have a reasonable number of samples at varying distances from the vessel, but without the control that may be possible in fixed, ex-vivo system. In an effort to reduce variability between ablations, we used a single ablation setting of 100 W for 5

minutes. While the results here can be potentially generalized to other power-time settings by using a scaling factor, such broad analysis was beyond the scope of this investigation and requires further evaluation. Secondly, the objective of our study was to focus on acute thrombus formation. There is a higher expected rate of delayed thrombus formation, which would result from not only the decreased blood flow from upstream acute thrombus but also the thermally-damaged endothelial layers [184]. Clinically, patients with cirrhosis and portal hypertensions could experience flow velocities significantly lower than those in healthy porcine livers and thus experience a much higher rate of portal vein thrombosis compared to what was seen in this study.

6.6 Conclusion

In conclusion, our in-vivo study demonstrated that portal veins are at higher risk for acute thrombus formation during microwave ablation as compared with hepatic veins, but thrombus formation is not as predictable in the portal vein. Hepatic veins showed a clear correlation between peak flow velocity, vessel size, and vessel-antenna spacing with the risk of thrombus formation but portal veins did not. We did not identify thrombus formation in a cohort of hepatic arteries greater than 4 mm in diameter. Follow-up studies to further refine the risk of vascular thrombosis in the clinical setting would be helpful for procedural planning and establishing risk profiles.

Chapter 7

Mechanisms of Thrombosis in Microwave Ablation in In-Vivo Porcine Liver Model

7.1 Abstract

Purpose: Thermal ablation is rapidly gaining traction as a viable alternative to surgical resection. A challenging issue with ablating tumors near blood vessels is determining how to overcome the heat-sink effect while not thrombosing larger vasculature. The reason behind why some vessels are predisposed to greater heat-sink effect and why others are predisposed to thrombus formation is currently unknown. The purpose of this study was to broadly observe the physical and biological differences between portal and hepatic veins that might explain these differences.

Materials and Methods: Animal care and use committee approval was obtained prior to in-vivo studies. A single microwave ablation antenna was inserted into a single porcine lobe (n=11 total) adjacent to a hepatic vein or portal vein branch. Conventional and Doppler ultrasound were used to measure the vessel size, blood flow velocity and vessel-antenna spacing. A fiber-optic temperature probe was placed in the lumen of the targeted vessel. A microwave ablation zone was then created at 100 W for 5 minutes. Thrombus formation was evaluated on immediate post-procedure ultrasound imaging. Genes coding for pro- and anti-thrombotic proteins were also analyzed on normal portal and hepatic vein tissue.

Results:Thrombosis was identified in 54.5% of portal veins (6/11) and 0% of hepatic veins (0/12). No significant difference in temperature elevation was observed between blood in the lumen of the portal vein and hepatic vein during the ablation period (0.24$\pm$0.38 °C versus 0.63$\pm$0.91 °C, p=0.46), even in the presence of thrombus formation. Normal, untreated portal veins demonstrated significantly higher gene expression fold-differences of thrombomodulin (THBD – 2.92 $\pm$ 1.98), von Willebrand factor (vWF – 7.53 $\pm$ 2.73) and the protein C receptor (PROCR – 3.55 $\pm$

1.28).

Conclusions: As seen in Chapter 6, portal vein thrombosis was more common than hepatic vein thrombosis during microwave ablations. Lack of luminal temperature changes during ablation in both vessels suggest most of the thermal damage occurs at the vessel wall. Significant differences in coagulation gene upregulation between portal veins and hepatic veins suggest that portal veins have an underlying propensity to thrombose compared to hepatic veins when exposed to thermal damage.

7.2 Introduction

Thermal ablation is an alternative to surgical resection for early-stage liver cancer [192]. Compared to surgical resection, ablation has been found to be associated with quicker recovery time, less complications and virtually no bleeding [193]. When performing an ablation procedure, image guidance with computed tomography (CT) or ultrasound (US) is utilized to guide the applicator into the vicinity of the tumor. In tumors abutting larger blood vessels, careful placement of the antenna is required due to the balance required for optimal treatment efficacy. Large blood vessels can siphon heat away from the ablation zone, a phenomenon known as the "heat-sink effect," decreasing the amount of thermal energy delivered to the tumor [150]. Undertreated tumors near blood vessels are at a higher risk for future recurrence. On the other hand, delivering too much heat around a vessel can cause excess vascular damage and subsequent thrombus formation, potentially shutting off blood supply to an entire lobe [132]. These consequences can be devastating for patients with decreased liver function from cirrhosis, commonly found in patients with primary liver cancer.

Radiofrequency ablation systems, the most commonly used ablation modality worldwide, utilize an electric current to treat the tumor. Volumetric heating of an entire tumor is dependent on passive thermal conduction to warm the tissue around the applicator. One drawback, however, is that the electrical conduction path can often be disrupted during heating, as the surrounding tissue becomes dehydrated and desiccated. As a result, radiofrequency ablation systems are plagued with incomplete heating. This deficiency is exacerbated by the heat-sink effect of nearby blood vessels, further increasing the chance of incomplete ablations [150].

Microwave energy, an ablation modality that has gained traction in recent years, utilizes an alternating electric field to oscillate polarized water molecules to generate heat inside tissue. This electric field is capable of penetrating various kinds of tissue, including desiccated and charred tissue, leading to tissue temperatures in excess of 100 degrees C. The heating advantages of microwave ablation over radiofrequency ablations are well-documented, with multiple studies reporting larger, more homogenous ablation zones in head-to-head ablation studies [44, 140, 181]. The higher heating rate of microwave ablation systems lends itself well to treating tumors near blood vessels, where the microwave energy can overcome the cooling effect of nearby blood vessels, improving treatment outcomes [38]. However, with such high energy deposition in tissue, a risk exists for vascular and peri-vascular damage near blood vessels. Thrombus formation using microwave ablation systems have already been noted in in-vivo and clinical studies [37, 132, 184].

Physicians want to overcome the heat-sink effect while avoiding vascular damage when carrying out ablation procedures near hepatic vasculatures. However, there exists only a limited studies characterizing vessel damage and heat sinks from radiofrequency and microwave ablation systems [37, 174, 184, 189]. These studies suggested that smaller vessels were more likely to be damaged and faster flowing

vessels would exhibit more of the heat-sink effect [38]. The in-vivo study related to Chapter 6 had demonstrated significant differences between portal vein and hepatic vein thrombus formation rates during microwave ablation procedures in in-vivo porcine liver models.

The purpose of this study was to broadly observe the physical and biological differences between portal and hepatic veins that might explain these differences. Intravascular temperature elevation during ablation was used as a marker to infer physical differences between portal and hepatic veins. Gene expression was also performed to broadly characterize underlying differences between vessels that can lead to thrombus formation.

7.3 Materials and Methods

7.3.1 In-Vivo Study

All studies were performed under approval from the institutional animal care and use committee and complied with National Research Council guideline. Animals were sedated with intramuscular tiletamine hydrochloride-zolazepam hydrochloride (7 mg/kg, Telazol, Fort Dodge IA) and xylazine hydrochloride (2.2 mg/kg, Xyla-Ject, Phoenix Pharmaceutical, St Joseph, MO). Anesthesia was maintained with inhaled 1.0-2.0% isofluorane (Halocarbon Laboratories, River Edge, NJ). An ear vein was cannulated with a 20-gauge angiocatheter for administration of IV fluids.

Individual microwave antennas (Neuwave Medical Inc, Madison WI) were inserted into single liver lobes (n=6) of two female domestic swine (50 kg); (Arlington Farms, Arlington WI). Microwave antennas were placed strategically in the vicinity of larger portal and hepatic veins (>5 mm diameter) under ultrasound guidance (Siemens Antares, Siemens Medical Solutions Inc, Issaquah, WA). Fiber-optic tem-

perature probes (MTG-170 Opsens, Quebec, Quebec) were then inserted under ultrasound guidance into the nearest vessel. Temperature probes appeared echogenic under ultrasound, marking the tip of the temperature probe. The temperature probes were strategically placed in the center of the vessel on the same plane as the microwave ablation heating element. Microwave ablation zones were then created at 100 W for 5 minutes, with the fiber-optic temperature probes recording temperatures every second. Post-ablation ultrasound imaging was performed after the ablation to confirm the placement of the fiber-optic temperature probe as well as any sign of vascular damage in terms of vessel stricture or thrombus formation **(Figure 7.1)**.

After ablation, animals were sacrificed by an IV injection of Beuthanasia-D (390 mgmL, pentobarbital sodium and 50 mg/mL phenytoin sodium at 0.2 mL/kg; Schering-Plough, Kenilworth, NJ). The liver was removed and sectioned along the axis of each antenna to expose the transverse cross-section of the nearby vessels and confirm the location of the temperature probe. Normal and ablated portal and hepatic veins were excised using sterile technique and utilized for the qPCR study, which is detailed in the following section.

7.3.2 Gene Analysis

For isolation of primary cell samples, endothelial cells were detached from portal and hepatic veins within 1-hour of animal sacrifice (n=3) under an approved animal protocol. Tissue samples were stored at -80 C. Reverse transcription (RT) reactions were performed using 1 ug of total RNA isolated from primary portal (n=9) and hepatic veins (n=9) and an RNA isolation kit (RNAeasy Plus Mini Kit; Qiagen, Venlo, Netherlands) for real-time RT (qRT)-polymerase chain reaction (PCR) and a reaction mix

Eight genes (Table 7.1) associated with pro and anti-coagulation proteins and an

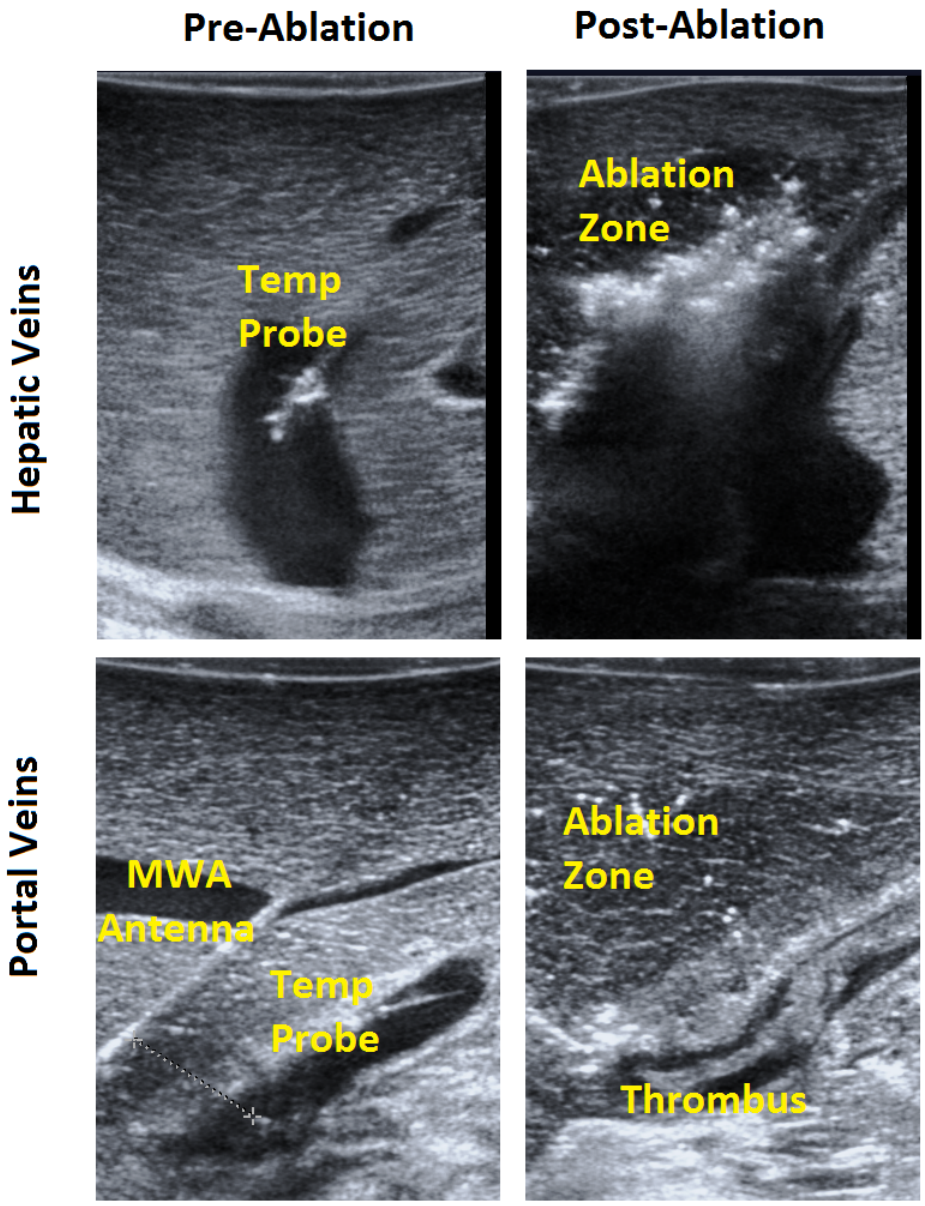

Figure 7.1: Intravascular temperature probe placement in hepatic veins and portal veins. A thrombus is noted in the portal vein (bottom right)

endogenous control (18s) were quantified with qRT-PCR by using a PCR platform (Bio-Rad CFX96; BioRad, Hercules, CA) and a reaction mix (FastStart Master SYBR Green I; Roche Applied Science, Basel, Switzerland) according to the manufacturer's

instruction manual. Real-time PCR was performed under cycling conditions of 95 °C for 10 minutes, followed by 30 cycles of denaturation at 95 °C for 10 seconds, annealing at 55 °C for 10 seconds, ad extension at 72 °C for 20 seconds using the nine primers. Primer sets used were validated (Integrated DNA Technologies, Coralville, IA) and quantified (J.C.) according to the PCR platform instructions. Measurements of mean cycle threshold value from triplicates (n=3) were used to calculate the expression of each gene using the 2ΔΔCt formula, normalized to ribosomal 18S in respective vessels as an internal control. Up-regulation was determined to be significant when differential expression of mRNA was more than two-fold.

Gene	Forward Primer/Reverse Primer
Urokinase	5′-GATCCCTCTGACTACCTCTATCC–3′ 5′–ACTTCGCTGCCGTAGTAATG–3′
Heparin Binding RPL29 (control)	5′–CAGAAACGGCATCAAGAAACC–3′ 5′–CTTCTTGGCAAAGCGCATATT–3′
Plasminogen Activator Inhibitor	5′–CAGGGTTTCATGCCCTACTT–3′ 5′–GTGTCTCTTCACCCAGTCATTT–3′
Thrombomodulin	5′–AAGTGGACAGAGGACCATTTC–3′ 5′–CCAGAGACCACCAACCAATAA–3′
Tissue Factor	5′–CACTGTTCAGATAAGCCCTAGAC–3′ 5′–CCTTCACGTTCCTCATGATCTC–3′
von Willebrand Factor	5′–CTCGAACCCAAGAAGAGAATGG–3′ 5–GGATCACTTCCTCCACAAACTC–3′
Plasminogen Activator	5′-ACATGTCTGCAGGCTATCTATTT–3′ 5′-GGTGGCTCTGGCATCTATTT-3′
Protein C Receptor	5′-GAAACACATCACCACGCATAAC–3′ 5′–CCACTCCTGCGATGATGAAA–3′
18s (control)	5′–CTGAGAAACGGCTACCACATC–3′ 5′–GCCTCGAAAGAGTCCTGTATTG–3′

Table 7.1: Pro-and anti-Thrombogenic genes from endthelial tissue was analyzed

7.4 Results

7.4.1 In-Vivo Study

Thrombus formation was detected in 54.5% (6/11) of portal veins and 0.0% (0/12) of hepatic veins on ultrasound and Doppler imaging **(Figure 7.2)**. Targeted portal veins and hepatic veins did not show significant difference between average vessel size (8.65 $\pm$ 2.37 mm vs 9.65 $\pm$ 3.38 mm, p=0.44), blood flow velocity(14.92 $\pm$ 4.87 vs 22.31 $\pm$ 11.67 mm, p=0.067) and vessel-antenna spacing (10.03 $\pm$ 9.87 vs 10.07 $\pm$ 2.63, $p<0.99$).

Probes showed temperature elevation from room temperature to the animal body temperature as the probes traversed the liver parenchyma. No significant difference in temperature elevation was observed between blood in the lumen of the portal vein and hepatic vein **(Figure 7.3)** during the ablation period (0.24$\pm$0.38 °C versus 0.63$\pm$0.91 °C, p=0.46), even in the presence of thrombus formation. A single temperature measurement of the vessel wall showed temperatures exceeding 100 °C during the ablation period. No acute thrombus formation was found in that particular sample **(Figure 7.4)**.

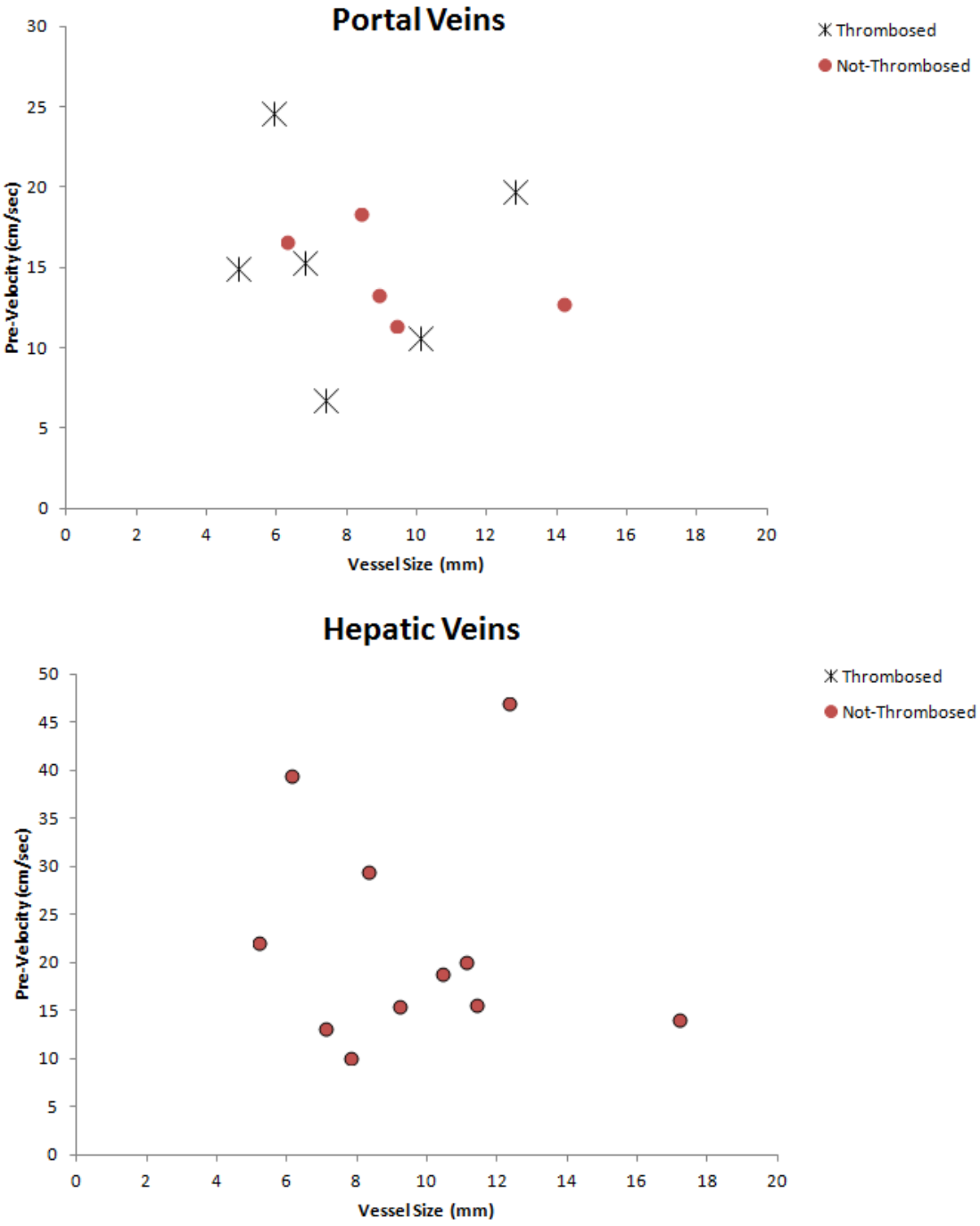

Figure 7.2: Thrombus formation rates were similar to those found in Chapter 6. Portal veins thrombosed at slightly higher than 50% rate while hepatic veins remained resistant to thrombus formation. Average vessel sizes, velocities and spacing were equivalent between portal and hepatic vein datasets.

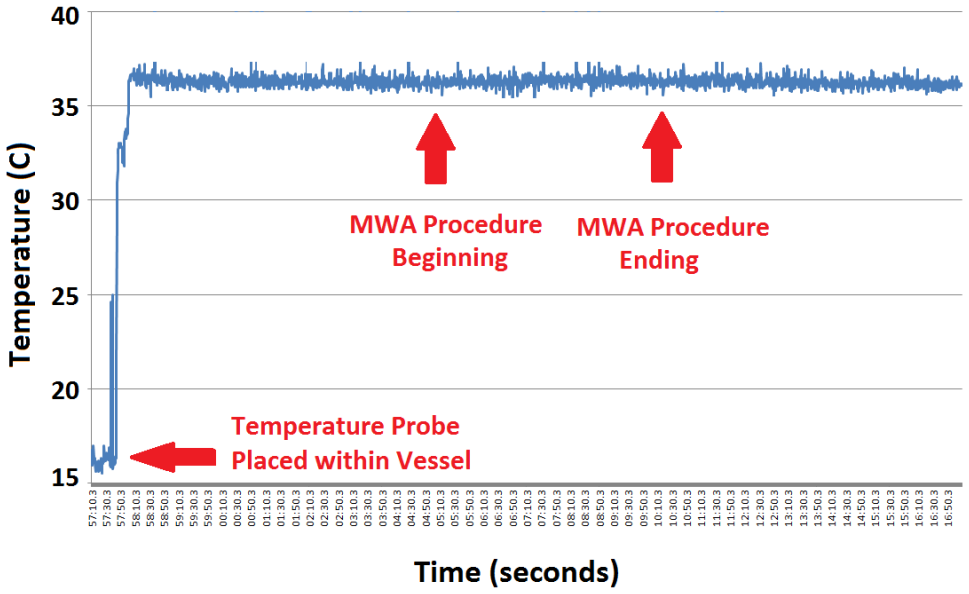

Figure 7.3: Hepatic vein temperature measurements. Initial rapid temperature elevation can be noted as fiber-optic probes move from room temperature to liver parenchyma. There was minimal change in lumen temperature during the microwave ablation procedure.

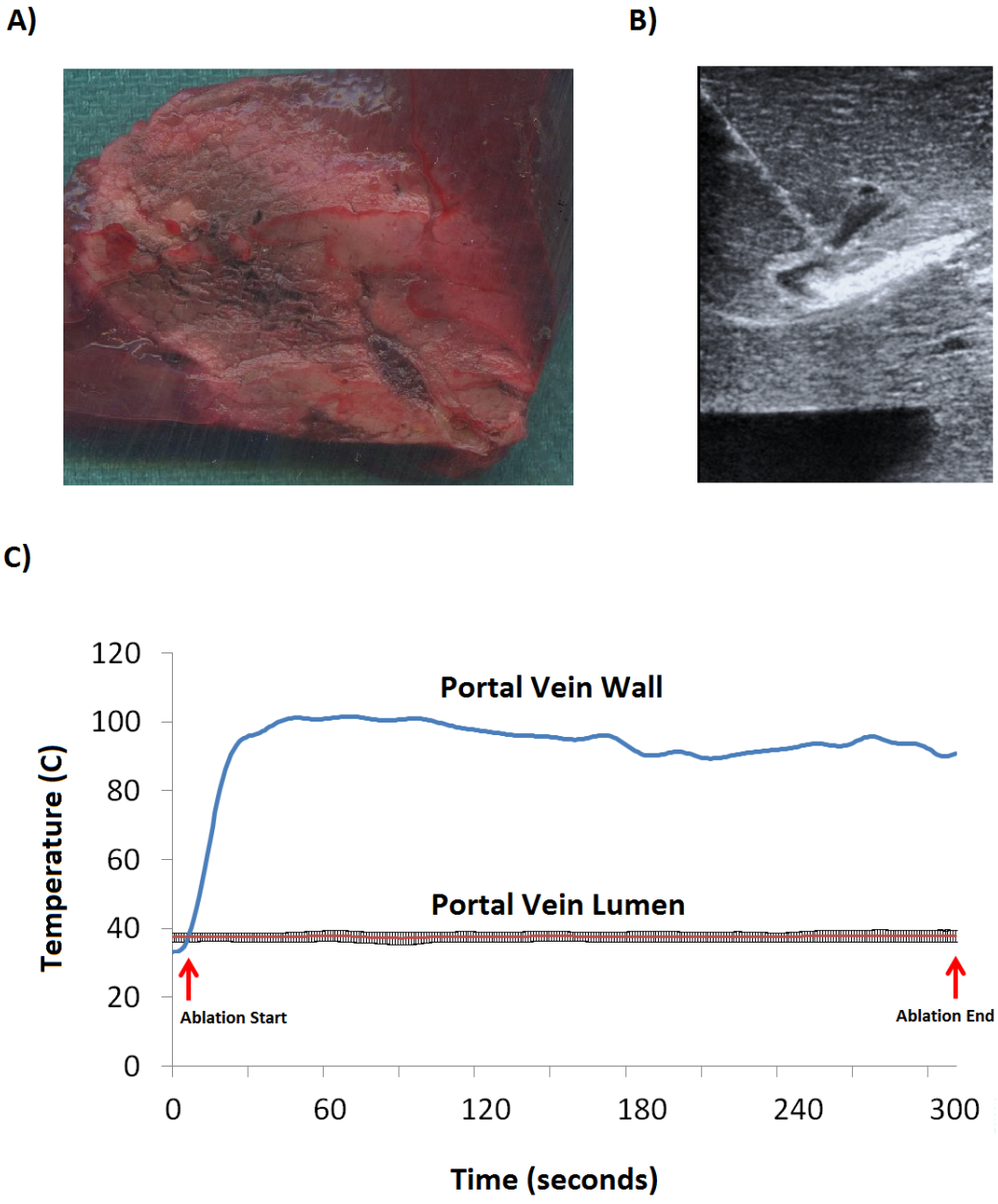

Figure 7.4: Portal vein temperature measurements. A) Gross pathology and B) ultrasoung imaging of ablation zone next to portal vein wall. C) Comparison between portal vein lumen and wall temperature during microwave ablation.

7.4.2 Gene Analysis Study

Portal veins demonstrated significantly higher gene expression fold-differences of thrombomodulin (THBD – 2.92 $\pm$ 1.98), von Willebrand factor (vWF – 7.53 $\pm$ 2.73) and the protein C receptor (PROCR – 3.55 $\pm$ 1.28) **(Figure 7.5)**.

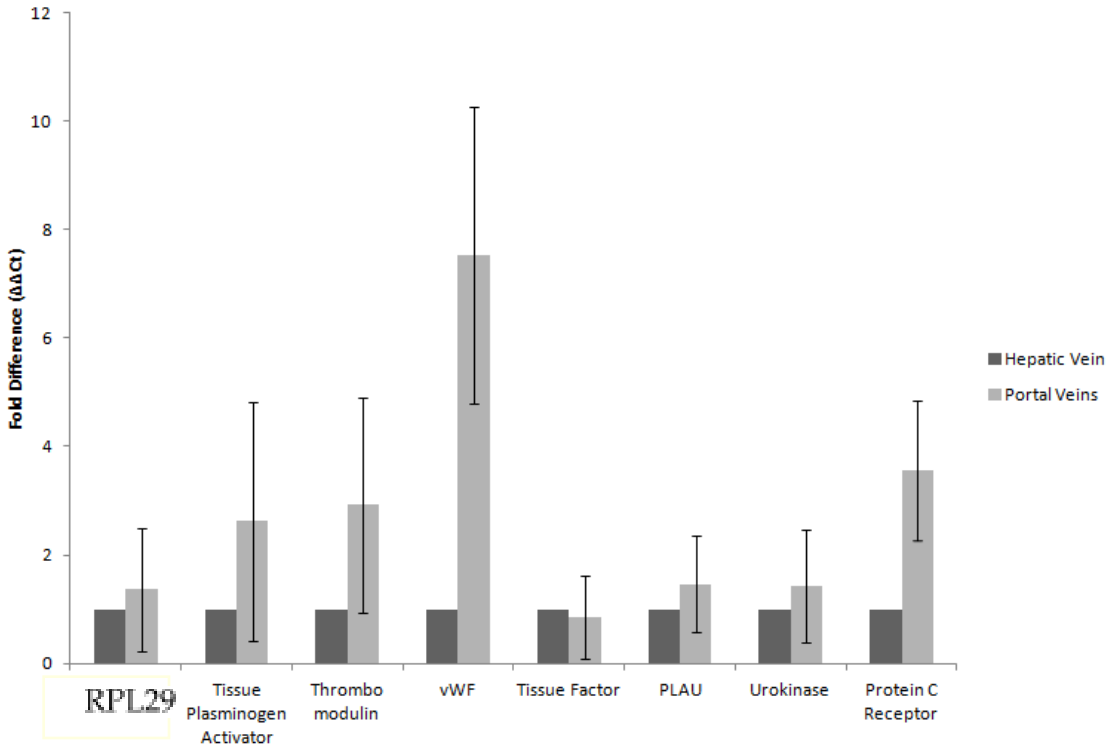

Figure 7.5: Gene expression differences between vessels. Normal, untreated portal veins expressed significantly more vWF, thrombomodulin and protein C receptor compared to normal, untreated hepatic veins.

7.5 Discussion

Thermal ablation has been widely cited as a faster and safer option for treating early-stage cancers. While resulting in significantly less complications compared to surgical resection, care is needed in carrying out ablation procedures. Most impor-

tantly, the ablation requires enough heat to destroy the tumor tissue and margin to minimize the risk for recurrence, especially near blood vessels that may interfere with the heating efficacy. On the flip side, however, too much heat delivered near the blood vessels may lead to inadvertent vascular damage and thrombosis, which is associated with complications that require management. Thrombosis or lobar infarction can be harmful to a patient with decreased liver reserves. The various ways that hepatic vasculatures can be damaged or affected by the heat-sink effect during thermal ablation are poorly understood due to the lack of characterization of portal veins and hepatic veins. A recent observational study had suggested that the cooling effect of nearby hepatic blood vessels can vary from vessel to vessel during laser ablation procedures in the liver. Specifically, the study concluded that portal veins exhibit more of a heat-sink effect compared to hepatic veins, based on how the ablation zone changes around the vessel [189]. Those results suggest that less thermal energy accumulates within portal veins, although the paper did not specify any potential mechanism. Ultrasound studies looking at mechanistic reasons for the appearance of echogenic rims in portal veins have suggested differences in vessel wall configuration [194]. At best, these references open up more questions as to why some vessels thrombose and why some do not during ablation procedures.

In this study, higher rates of thrombus formation were found in portal veins compared to hepatic veins, even with near equivalent vessel size, velocity and vessel-antenna spacing, results that are consistent with the data presented in Chapter 6. However, intravascular temperature measurements during ablation showed absence of temperature elevation within the lumen of a vessel near an ablation zone, even when thrombus formation was noted. It is clear that the thrombus formation cannot be attributed to a simple temperature elevation since there was no temperature elevation noted. The single measurement of vessel wall temperature (on the luminal

side) during ablation revealed a temperature spike up to 100 °C, far above cytotoxic temperatures. Although far from conclusive, the evidence seems to rule out that we are simply "boiling" the blood to cause thrombus. A more likely explanation is that thermal damage in the vessel wall is activating a biochemical process such as the clotting cascade.

The qRT-PCR study showed significantly more expression of von Willebrand Factor, endothelial Protein C receptor and thrombomodulin in portal veins compared to hepatic veins. While these particular genes code for both pro-coagulation and anti-coagulation proteins, their different expression between vessels highlight the fact that even vessels within the same organ can have varying potential for thrombus formation.

The underlying mechanism for preferential thrombus formation in portal veins compared to hepatic veins is presently unclear. Mechanically, the flow pattern of portal veins and hepatic veins differ drastically due to the fact that the hepatic veins drain into a low-resistance inferior vena cava and the portal vein into a high-resistance capillary beds of the liver. Thus, hepatic veins have a highly pulsatile flow that corresponds to the cardiac cycle while the portal vein is associated with more of a damped, continuous flow. Computational studies that show pulsatile flows affecting heat transfer of larger vessels also suggest negligible effect in the smaller vessels normally found in the liver [190, 191]. A plausible link for the role of pulsatile flow in thrombus formation lies in the genes and associated proteins associated with clotting. Specifically with our proteins of interest, there is a large body of evidence associating their activation and aggregation with rates of endothelial shear stress [195-197]. In light of these previous studies, controlled studies looking at the effects of shear stress on thrombus formation in the liver seem warranted.

Due to the transient nature of thrombus formation and multiple factors leading

up to a thrombotic event, there were many facets of the study that could be improved upon. First we treated the ablations as independent events in the same animal, even though there are potential systemic effects that can affect the potential for thrombus formation. Platelet counts and inflammatory markers were not monitored in the animal, preventing the elimination of potential of inter-lobar effects. Secondly, while the vessel characteristics were averaged across many samples, the complex anatomical and biochemical environment associated with each sample would be more accurately represented if the outputs were paired with its own inputs. However, since we were only looking at thrombus formation and larger (>10 degree °C) changes in temperature, the individual temperature measurements were averaged together. This would be more important for computational modeling studies, where the details of the input anatomy and heat transfer environment are important. Third, the amount of thermal damage within the blood vessels was not quantified. While the ablation zone typically encompassed at least a portion of the vessel, vessel damage was simply categorized as a binary event with respect to thrombus formation. Area of cellular damage with respect to the vessel would be useful in determining if there is a critical threshold required for thrombus formation. Lastly, with respect to our gene expression study, only normal portal and hepatic veins were investigated. Post-ablation vessel damages have effects of thrombus-related gene expression that were not evaluated, but could potentially play a role in delayed thrombus formation.

In conclusion, this study suggested that temperature elevation in the vessel wall, rather than the lumen, near an ablation zone is not likely to contribute to thrombus formation. Cytotoxic temperatures near the vessel wall can potentially cause enough damage to activate the coagulation cascade within vessel near those heating zones. Differences in gene expression associated with clot formation were found between portal and hepatic veins, providing a plausible link between thermal damage and

thrombosis. The individual effects of specific genes and proteins related to clotting and their activation from thermal damage need to be characterized in order to confirm the links found in this study.

Chapter 8

The Role of Single and Dual-Source Energy Computed Tomography in Water Content Measurements

8.1 Abstract

Purpose: The purpose of this study was to investigate the possibility of using conventional and dual-energy CT to non-invasively infer changes in water content in ex-vivo liver tissue.

Materials and Methods: Ex-vivo liver tissue blocks (n=6) weighing approximately 15 grams were dehydrated to water concentrations of approximately 25%, 50% and 90% water loss by weight using a manual desiccators rack. Tissue blocks were scanned under conventional CT and a histogram of the tissue radiodensity was created. Water content was then correlated to higher-order statistics of the radiodensity distribution. A completely desiccated sample was also scanned under a dual-energy CT scanner to decompose the liver block into water, vapor and solid liver tissue.

Results: Linear mapping of mean radiodensity and kurtosis to water content showed good correlation, with a Pearson correlation coefficient of R^2= 0.780 and R^2=0.819, respectively. Dual-energy scans demonstrated accuracy in identifying gas spaces against water or liver tissue. Since the radiodensity of water and liver tissue was very similar, there was difficulty in separating water and liver from the scan.

Conclusions: Single and dual-energy CT scans can be used to infer changes in moisture content within ex-vivo liver tissue. However, the results are depending on post-processing and interpretation is limited to this specific experimental setup.

8.2 Introduction

One of the advantages of microwave tumor ablation technology is the ability to continuously heat through tumor tissue, leading to higher temperatures and more homogenous heating zones compared to other heating modalities such as radiofrequency and laser [139]. The consistency in forming ablation zones in tumor tissue leads to better margins for tumor destruction and a smaller chance for recurrence [198].These improved heating physics have led to its rapid adoption and replacement over predecessor technologies.

Since microwave energy is capable of propagating through dried and desiccated tissue, temperatures near the microwave antenna can often exceed 100 degrees C. This rapid heat generation leads to the formation of water vapor and its subsequent movement through tissue. The mass of water vapor appears as a hypodense region under computed tomography (CT) imaging, easily distinguishable from the background tissue, which undergoes only minimal changes in Hounsfield Units (HU)during heating from the temperature change [199].

The tracking of water vapor formation and movement through tissue has traditionally been utilized in computer modeling of food processing and cooking [200]. Cooking techniques such as frying, baking or boiling often leads to varying patterns of dehydration and moisture movement. As a result, these underlying physics of vapor formation often has a strong contributory affect on the texture and taste of the final dish. With microwave ablations, the moisture can directly change how the electromagnetic waves and heat travel through the tissue, by altering the dielectric and conductivity of the tissue [108, 111, 201]. Moisture content can also indirectly serve as a marker for temperature distribution. Within an ablation zone, the area near the center of the ablation appears dark and charred, with most of the

moisture driven out from the intense heating in the region. Immediately outside of this area, tissue appears blanched and can often serve as an estimate for cytotoxic temperatures where cell death has occurred instantaneously. In areas beyond the ablation zone, where the microwave energy has not reached, the tissue appears pink, having retained a large fraction of its original water content, and accompanied with some inflammation. Monitoring these moisture changes in real-time can provide invaluable information about how tissue is changing during an ablation procedure, leading to improved numerical predictions and system design.

Moisture content in tissue is inherently difficult to measure due to the necessity to disturb its local environment using conventional drying techniques. This requires isolating the surrounding environment to prevent water loss and monitoring the decrease in water mass as the material is desiccated. This method has been adapted by many moisture analysis devices and can make an estimate of water content within minutes. While fairly accurate, this technique does not capture the time-sensitive moisture changes occurring within an ablation zone during the ablation procedure, which occurs over the period of seconds. A quick and easy technique for inferring these moisture changes would provide a powerful validation technique for numerical modeling predictions.

Conventional CT scans are useful in monitoring experimental thermal ablation due to their resolution and speed, as well as their ability to distinguish vapor from tissue [103]. Dual-energy CT scanners offer even more information by acquiring CT images at 2 different x-ray photon energies and recording their respective attenuation between various materials. While algorithms exist to use these attenuation differences to highlight iodine, water and minerals in a single scan, they are not designed to decompose phase changes in a material of interest. CT scanners are also already used in the clinical workflow to confirm microwave antenna placement,

lending itself well to the potential translation into real-time patient-specific water content measurements. The purpose of this study was to investigate the possibility of using conventional and dual-energy CT to non-invasively infer changes in water content in liver tissue.

8.3 Materials and Methods

8.3.1 Tissue Preparation

Ex-vivo liver tissue blocks (n=6) weighing approximately 15 grams were dehydrated to water concentrations of approximately 25%, 50% and 90% water loss by weight using a manual desiccators rack and initially assuming a 70% water content in each tissue sample (**Figure 8.1A**). Once the tissue reached the desired moisture loss, the tissue was immediately sealed to prevent further water loss. The images were then scanned, as described in the next paragraph, and then completely desiccated to confirm the original water content in the tissue sample (**Figure 8.1B**).

8.3.2 Single-Energy CT Scan

CT imaging was performed on a GE Lightspeed CT750 HD 64-Slice Scanner, 120 kVP, 200 mA, 0.625 mm by 0.625 mm resolution. All desiccated liver tissue blocks were placed on the same plane, while images were taken coronally. An ROI was placed around each liver block and a histogram of the HU ranging from -800 to 200 HU. The mean, standard deviation, kurtosis and skewness of the HU distribution was calculated for each sample and averaged across corresponding groups of the same moisture content. A Pearson correlation coefficient was then calculated to assess how well each metric correlated to the sample water content.

8.3.3 Dual-Energy CT Scan

Dual-energy scans were performed on completely dehydrated liver tissue at 80 (peak) kVp and 140 kVp. Completely dehydrated tissue was chosen in order to get the components of water vapor, liver tissue and water to group together and make them easier to categorize on the CT scan. In this setup, the liver, tissue and gas are compartmentalized and reduces the amount of tissue that may be difficult to decompose. Since the images were taken simultaneously, there was no additional step required to maintain proper registration. Liquid deionized water was simultaneously scanned as a reference point.

The material decomposition procedure utilized the following three equations, with three unknowns representing the fractional contribution of water, vapor and solid liver,

$$\mu_{water_{1}40kVp} f_{water} + \mu_{vapor_{k}Vp} f_{vapor} + \mu_{liver_{1}40kVp} f_{liver} = \mu_{total_{1}40kVp} \tag{8.1}$$

$$\mu_{water_{8}0kVp} f_{water} + \mu_{vapor_{8}0kVp} f_{vapor} + \mu_{liver_{8}0kVpkVp} f_{liver} = \mu_{total_{8}0kVp} \tag{8.2}$$

$$f_{water} + f_{vapor} + f_{liver} = 1 \tag{8.3}$$

where μ represents the Hounsfield unit of the material at the energy specified in the subscript. For water, vapor and liver tissue, identical pixels were compared at both photon energies. The 140 and 80 kVp are the HU values corresponding to the pixel value in the CT at each respective energy and f is the fraction of the material

indicated by the subscript contributing to the pixel value we calculate. A fraction of 1 corresponds to a pure material. With 3 equations and 3 variables, it becomes possible to solve this system of equations, where the fraction of each phase was restricted between 1 and 0, corresponding to 100% and 0% of the material. Pixel values that were less than the smallest material values of μ were assumed to be composed of neither vapor, water, nor solid liver.

8.4 Results

8.4.1 Single-Energy CT Scan

Final tissue block groups had an average final water content percentage of 27.8%, 53.9% and 91.5%. Mean HU had a Pearson correlation coefficient of R^2= 0.780 when compared to water content (**Figure 8.2**). The kurtosis of the data set was slightly better, with a Pearson correlation coefficient of R^2=0.819 (**Figure 8.3 and Figure 8.4**). These two metrics had much better correlation compared to the standard deviation and skewness (R^2=0.4687 and R^2=0.6635).

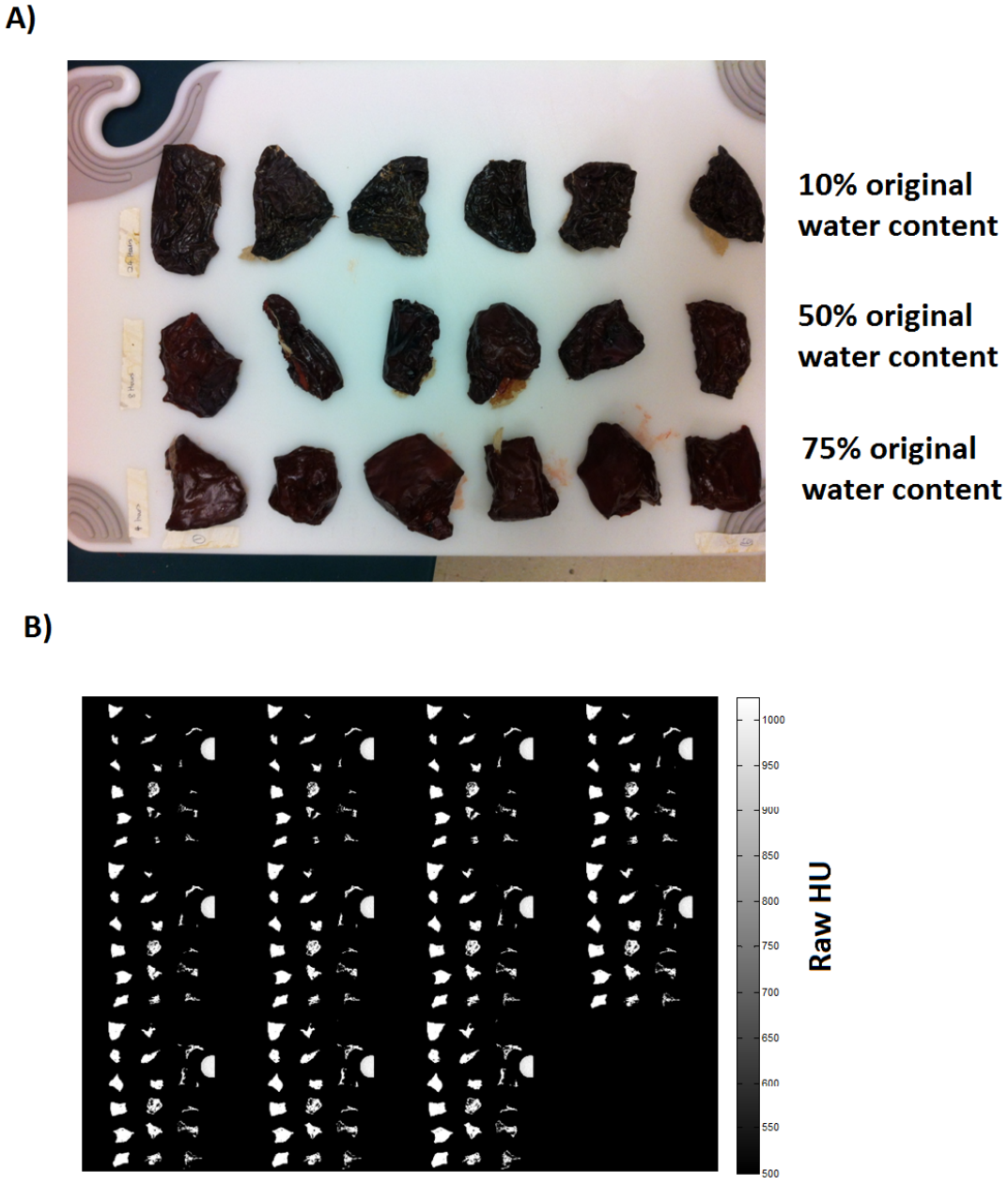

Figure 8.1: Ex-vivo liver blocks were A) dessicated to 10%, 50% and 75% original water content using a manual dessication rack. B) Each sample underwent CT imaging through the entire volume. Each image set represents a CT slice at a different depth.

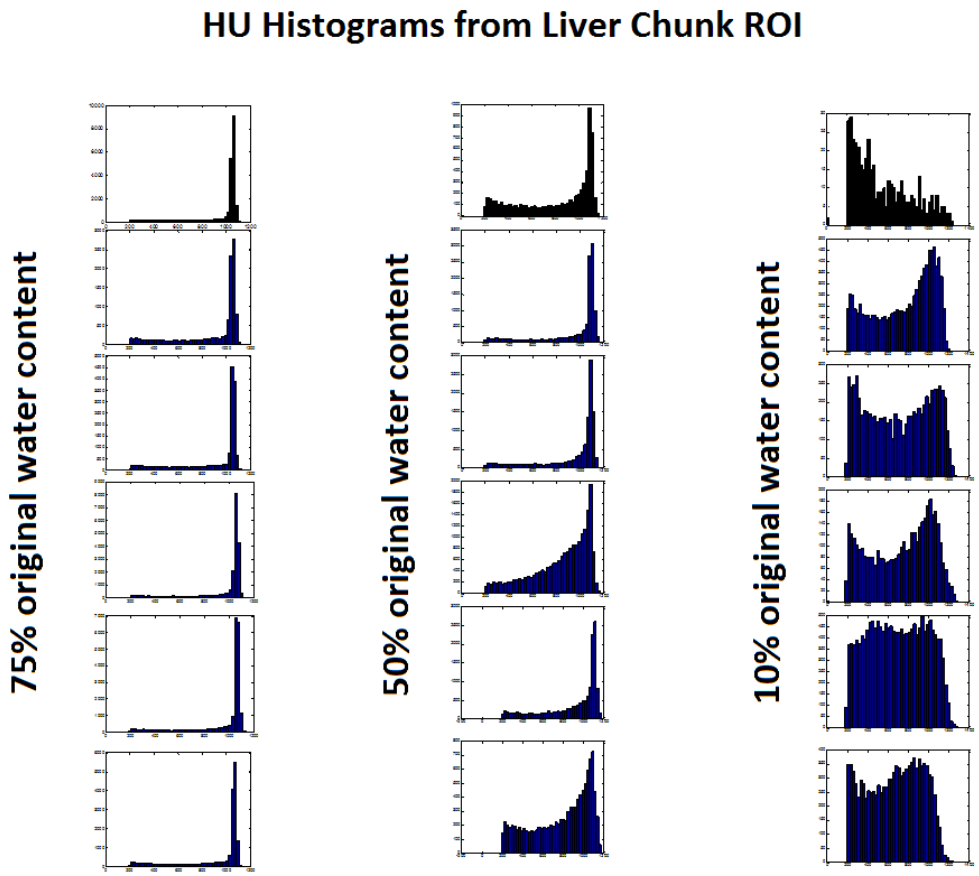

Figure 8.2: Radiodensity histogram from single-energy CT scan. The histogram comprises of the CT numbers of the compiled voxels in each volumetric scan. As more dehydration occurs, there is a wider distribution of CT numbers. This phenomena is due to the fact that the volumetric void where water (HU~0) had original occupied becomes filled with air (HU~-1000).

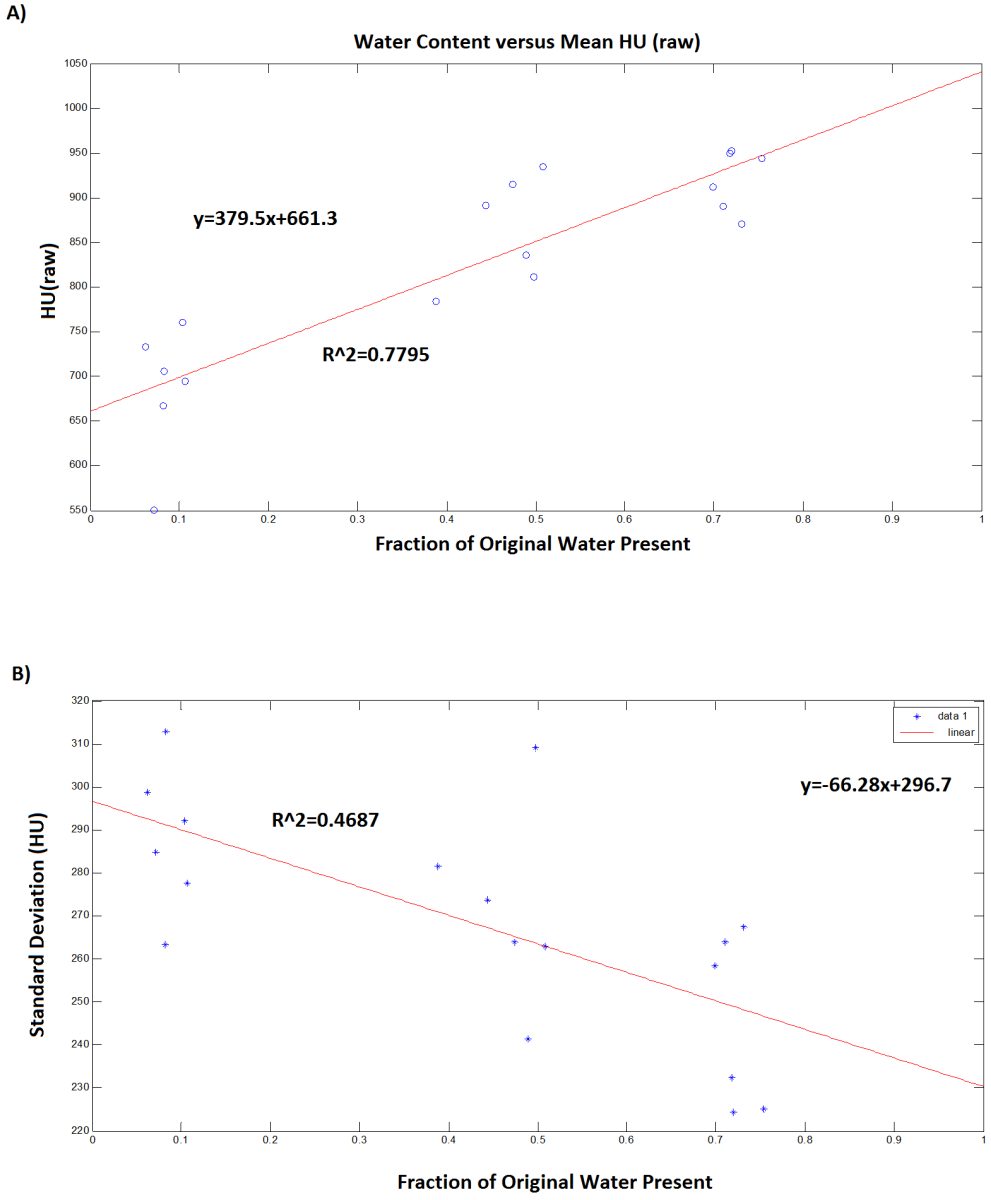

Figure 8.3: Mean and standard deviation of radiodensity with respect to water content. A) Mean HU increased with increased water fraction, which is expected due to the large attenuation of water compared to air. B) Standard deviation of HU decreased with corresponding decreased water evaporation due to the lack of change in material from normal ex-vivo tissue.

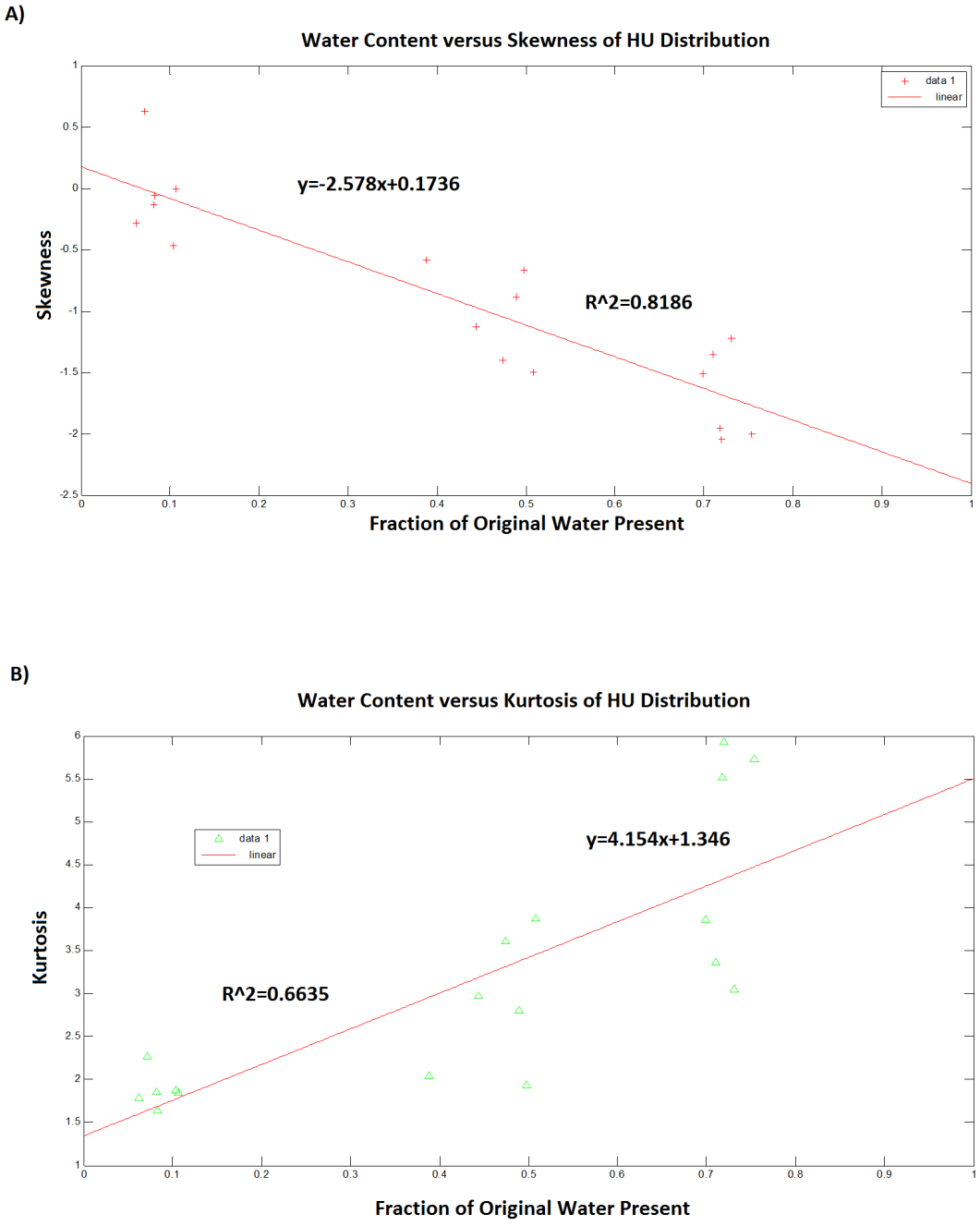

Figure 8.4: Kurtosis and skewness of radiodensity distribution with respect to water content A) Kurtosis decreased with increased water content due to the wider distribution of water-filled voxels in liver material. B) Skewness of the radiodensity increased with increased water content due to the histogram shift toward water (HU ~ 0) over air ~ -1000

8.4.2 Dual-Energy CT Scan

Since HU utilizes pure liquid water as a reference point, we set the CT number of water at both 80 kVp and 140 kVp to 1024 HU, which accounts for the linear transformation found in raw CT values. The CT values of solid liver were found by averaging the CT value of an ROI within the densest part of the liver block. The solid liver ROI was found to have a CT value of 1174 HU at 80 kV and 684 HU at 140 kVp. The value of gas, which was found by averaging the gas pockets formed with the liver blocks, was found to be 1174 HU at 80 kVp and 1124 HU at 140 kVp (**Figure 8.5**). Qualitatively, the results showed reasonable accuracy in decomposing the gas and solid within the desiccated liver block. The gas pockets within the liver were highlighted well while the solid liver showed a range of solid liver densities corresponding to varying degrees of hydration. The inferior portion of the liver chunk was the most dense, showing the most desiccation and least gas pockets (**Figure 8.6)**. Our results seem to confirm this suspicion.

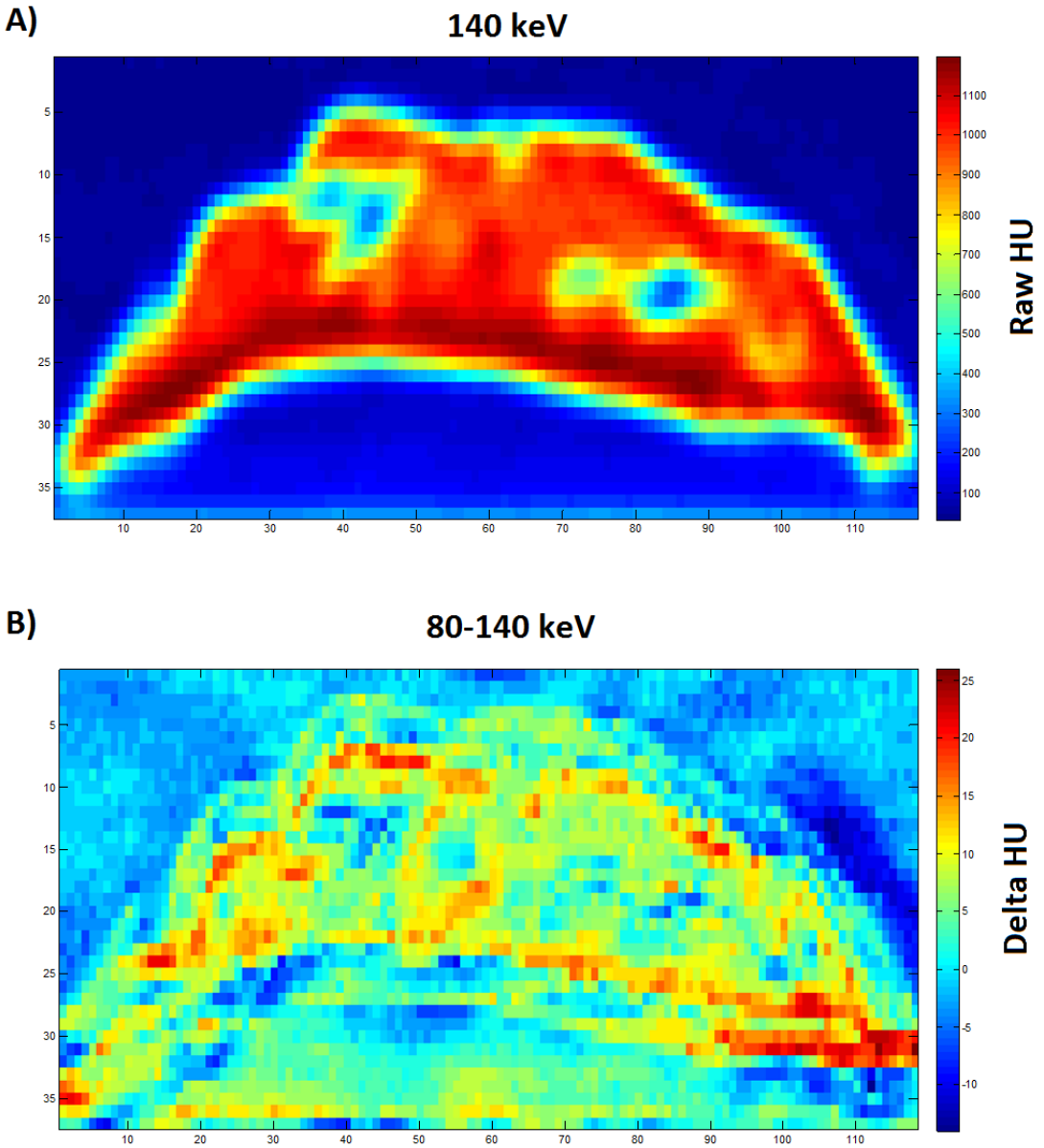

Figure 8.5: Radiodensity map of a completely desiccated liver blocks A) using photons of 140kev and B) The difference in radiodensity when the 80 keV radiodensity map is subtracted from the 140 keV radiodensity map.

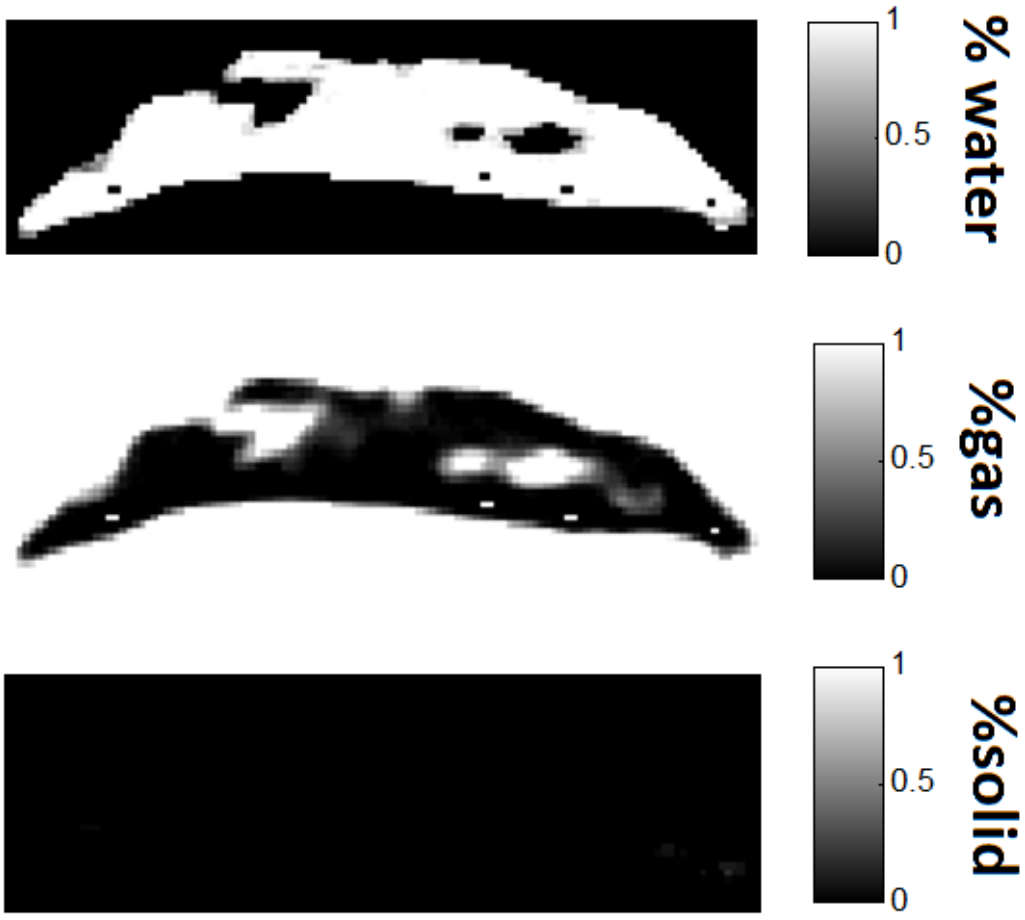

Figure 8.6: Unadjusted data from solving the system of Equation. While the gas mapping is accurate, with the spacings being made of 100% gas, the water mapping results point to the liver block being made of mostly water. Meanwhile, the solid material vector is mostly non-existent

Certain adjustments to the material weighting could be made to highlight water content, although this came at a cost of accurately monitoring the fraction of the other two components (**Figure 8.7**).

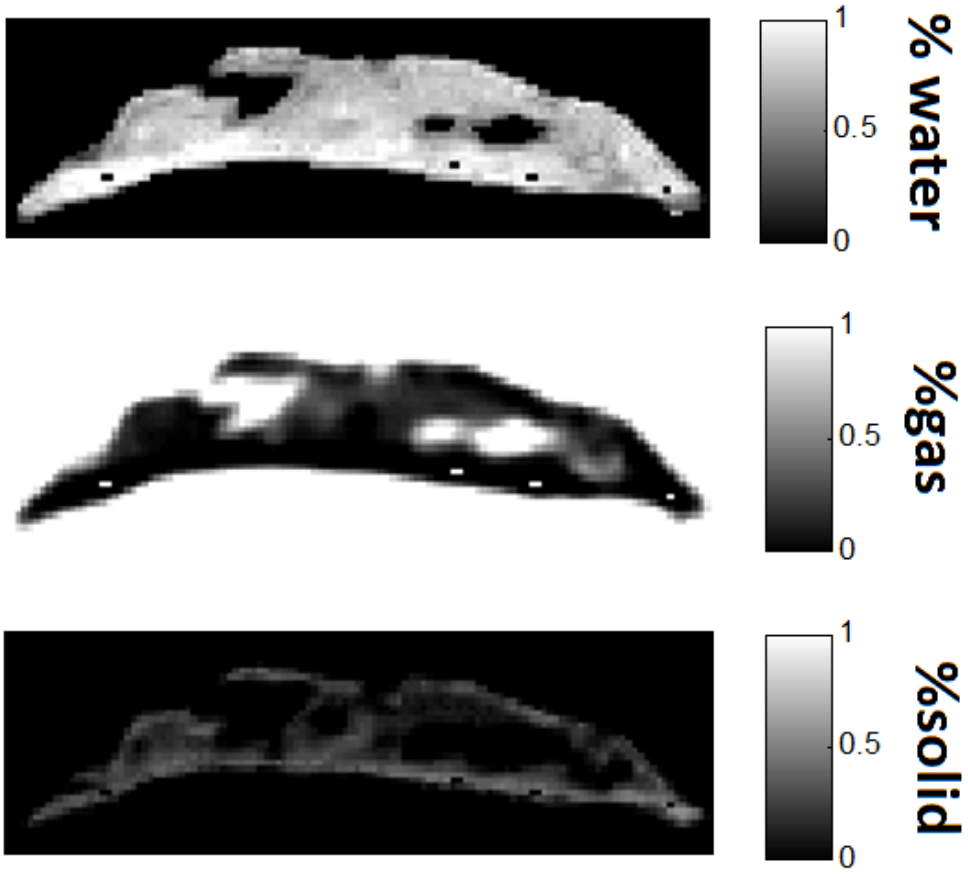

Figure 8.7: Reducing water dimensionality by holding the gas and solid contributions constant led to a slightly more accurate representation of the liver block material

8.5 Discussion

In this study, we investigated the possibility of using conventional and dual-energy CT imaging to make inferences on water content and phase within ex-vivo liver tissue. Liver blocks of different water concentrations were scanned and their distribution of radiodensity across a region of interest was correlated using higher-order statistics to their corresponding water content. Dual-energy CT was utilized to decompose a liver block to its basic constituents liver tissue, liquid water and vapor

within a CT image.

The dehydrated liver chunk demonstrated reasonable correlation between mean HU and skewness when plotted against water content. Ad drop in mean HU corresponded to a decrease in water content. This result was expected due to the fact that as water changes from a liquid to vapor state, the CT number will drop. In most conventional CT scanners, liquid deionized water is set to a CT number of 0 HU and vapor is set to -1000 HU. As liquid water changes to vapor, the CT number will decrease and our results correctly reflect the presence of an evaporation process. A similar trend was seen in the radiodensity skewness, where the distribution of the CT number shifted to the left, or a more negative value. This represents the transition from liquid to vapor and the subsequent shift of the ROI to a more negative radiodensity as the volume of vapor increases. While there was a correlation between standard deviation and kurtosis to the radiodensity distribution, the correspondence was less strong than that of the mean and skewness.

The results of the dual-energy study suggested that while there is potential in decomposing a material into its separate phases, there is a cost in terms of accuracy. Without reducing any of the dimensions, the solution to the system of equation highlights the presence of gas/vapor but has trouble distinguishing between water and solid. In fact, without imposing any additional boundary conditions, the solution of the system of equations point to the liver tissue being comprised mostly of liquid water and almost no tissue. Only by holding the water CT number constant across the two energy levels, a valid assumption since deionized water serves as a reference for all other materials, does the vapor and solid phase of the liver blocks show up accurately. As a result, however, we are left without any information about the changes in water content throughout the liver tissue. Depending on what material a researcher is interested in it is possible to adjust the CT number to

highlight contributions of the solid, liquid or gas to fit their need. As it stands, dual-energy CT currently still seems to be best utilized for two-material decomposition.

Microwave ablation systems are capable of heating tissue to high temperatures associated with water vaporization. Due to the mass transfer and energy released on condensation, much of the physics previously used to characterize radiofrequency or laser ablations are not applicable. Research efforts to account for the change in thermal and electrical properties of tissue due to this water vaporization phenomenon have recently gained traction in improving model accuracy. A critical component in this advance in model development is a quick and reliable method of validation. Previous methods of confirming water content was cumbersome and involved processes that often disrupted the sample. The quick and accurate tracking of vapor formation movement through CT lends itself well to modeling validation, as comparisons can be made on a second-to-second basis. Furthermore, information about water content can be used to reveal changes in tissue dielectric or conductivity parameters. The results of this study showed that while some level of moisture content can be correlated from tissue CT numbers, the method seems to be tissue environment-specific and requires more optimization to increase reliability. The radiodensity of a material is dependent on the material's propensity to absorb x-ray photons by the photoelectric effect or deflected by Compton events, usually defined by a material's effective atomic number in the material. In the conventional CT study, it was apparent that in a highly controlled study, the desiccation process that reduced water content also introduced gas pockets into the liver blocks. These gas pockets made the biggest contribution to the changes seen in the radiodensity histogram. In a more clinical environment, where desiccation may not lead directly to gas pockets in tissue, these changes in radiodensity may behave differently. In the dual-energy study, there was difficulty in separating the desiccated tissue and water,

which have a CT number of 0 and 120, respectively. On a range of radiodensities that stretches over 2000 HU, the difference between water and liver was too small to derive much meaningful information.

There were multiple avenues where the CT study design could potentially be improved to track water more accurately. Radiodensity of tissue is reflective of pressure and temperature changes, which are changing rapidly during a microwave ablation. Monitoring these two variables with temperature and pressure probes in select areas of the tumor block could potentially lead to a more accurate calculation of the true contribution of water vapor to the tissue radiodensity. Another factor that was not accounted for was the issue of contraction, which can have a dramatic effect on the physical location and movement of gas volume. Elucidating this phenomenon will be a critical component in properly localizing water vapor during an ablation zone. Lastly, there was the difficulty in separating the individual contributions of three variables assuming that each pixel was only comprised of a linear combination of materials. The radiodensity of vapor is quite different from solid liver or water, making it a bit easier to decompose a CT number when assuming there is not mixing, as see in our completely dehydrated liver block. However, the lack of separation between radiodensities of tissue and water made it difficult to assess their contribution to the overall attenuation. Potentially adding additional variables such as temperature/pressure and using higher-order functions could lead to a more accurate measure of moisture content.

8.6 Conclusion

In conclusion, the conventional and dual-energy CT showed good correlation to moisture content. Although the results were specific to this particular study design,

some of the post-processing statistical techniques could potentially be utilized in the study of moisture content in tissue during thermal ablations, especially with respect to their changing electrical and thermal properties.

Chapter 9

Modeling and Validation of Microwave Ablations with Internal Vaporization

9.1 Abstract

Numerical simulation of thermal tumor ablation is increasingly being utilized for computer-aided design of treatment devices, analysis of ablation growth, and clinical treatment planning. Simulation models to date have incorporated electromagnetic and thermal modeling, but other thermal physics such as those associated with water vapor formation and mass transfer have been neglected. Such physics are thought to be non-negligible at high heating rates, especially those associated with microwave heating. In this work, a numerical model was created that integrates microwave heating with water-vapor physics by using porous media assumptions in the tissue domain. This model was then validated through intra-procedural computed tomography (CT) of microwave ablations in homogenized ex-vivo bovine liver tissue. Iso-density contours from CT were compared to vapor concentration contours from the numerical model at intermittent time points using the Jaccard Index. In general, there was an improving correlation in ablation size dimensions as the ablation procedure proceeded, with a Jaccard Index of 0.27, 0.49, 0.61, 0.67 and 0.69 at 1, 2, 3, 4, and 5 minute marks. This study demonstrates the feasibility and validity of incorporating water vapor concentration into thermal ablation simulations and validating such models experimentally.

9.2 Introduction

Tumor ablation is an emerging treatment strategy for early-stage solid tumors that are not amenable to surgical resection or which have failed chemotherapy or radiotherapy [139]. Thermal ablation is typically performed using applicators that have a thin, needle-like profile that can be inserted into the target zone under imaging guidance. Once positioned, energy is applied from the distal tip of the applicator to elevate the temperature of the adjacent tissue to cytotoxic temperatures, typically above 50-60°C, in a short period of time.

The most widely utilized ablation modality to date is radiofrequency (RF) ablation, which generates heat using RF electrical current applied directly to the tumor [11]. However, at cytotoxic temperatures, the electrical impedance of the tissue quickly rises due to dehydration and water vaporization, limiting the application of additional RF current. There is now increased interest in the application of microwave energy, which is not limited by the presence of charred or desiccated tissue. Microwave systems are capable of creating larger and more homogenous ablation zones compared to those made in predicate RF ablation systems, even around heat-siphoning vasculature – leading to more complete treatment and potentially decreased risk for tumor recurrence [181].

Numerical simulation of thermal ablations is an area of active research, leveraging computer-aided design to optimize ablation systems and treatment planning. However, numerical techniques used previously to simulate RF ablations cannot be fully applied to microwave ablations. Due to its superior heating efficiency over RF energy, microwave ablation systems are capable of heating tissues to well above 100°C and maintaining those temperatures for several minutes, vaporizing liquid water of the tissue and driving vapor outwards from the antenna. These vapor pock-

ets diffuse through the tissue and re-condense either within tissue or nearby blood vessels [103]. To account for the additional water vapor physics and create accurate modeling predictions, improved computer modeling techniques are required.

Incorporating vapor formation and transport into numerical models has been investigated primarily considering a porous media approach in food materials such as bread and meat [200, 202, 203]. However, those models have not been applied to an interstitial heat source such as a microwave ablation antenna and have not been used to evaluate heating in other biological tissues such as the liver, kidney or bone. Studies incorporating vapor formation into thermal ablation models has been limited to the development of temperature-dependence to tissue dielectric properties and adding the latent heat of water vaporization into the heating model [103, 107, 108, 111]. Successful prediction and measurement of water vaporization during microwave ablation procedures would allow the researchers to validate the model involving water physics, thereby leading to more accurate modeling predictions. In turn, this will help optimize microwave system design and ablation treatment planning.

The purpose of this study was to investigate the possibility of simulating water vapor concentrations and validate the simulation outputs using CT imaging. We numerically modeled this tissue-heating environment, incorporating electromagnetic as well as thermal and mass transfer physics [139, 200, 203]. We then experimentally replicated the computational model setup using a homogenized liver solution and compared the numerical and experimental vapor profiles using similarity indices. The results of this validation study provided an assessment to the possibility of using moisture content as a tool to monitor ablation zone growth.

9.3 Materials and Methods

9.3.1 Numerical Technique

From a computational modeling standpoint, hepatocytes and blood vessels may be considered as a porous skeleton, with water being the major constituent bound to it. As liver tissue is being heated from microwave energy, tissue water undergoes a phase change and can be transported inside the solid matrix or released into the porous space. Therefore, a numerical description of microwave ablation may be developed using established techniques for heat and mass transport in porous media [200].

Geometric Model

An axially-symmetric geometric model was developed for homogenized tissue in a cylindrical glass container (80 mm radius $\times$ 90 mm height) and a microwave antenna inserted into the liver model as shown in **Figure 9.1**.

Governing Equations

Heat and water mass transfer during a microwave ablation procedure were simulated using the finite-element method (FEM) in commercial software (COMSOL Inc, Burlington, MA). Electromagnetic field vectors were calculated by solving Maxwell's equations (not shown for brevity) for an axially-symmetric coaxial microwave antenna geometry inside liver tissue at 2.45 GHz. Electromagnetic power dissipation density Q, a function of electrical conductivity σ (S/m) and electric field intensity magnitude E (V/m) was determined through the equation:

$$Q_h = \frac{\sigma}{2} \parallel \mathbf{E} \parallel^2 \quad [W/m^3] \tag{9.1}$$

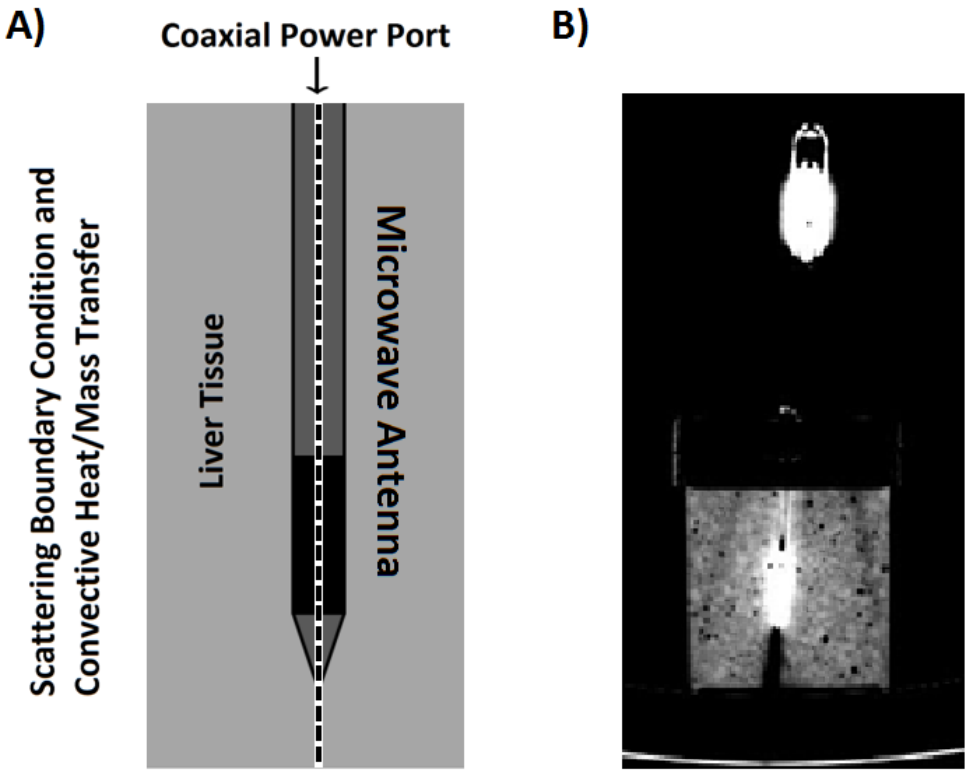

Figure 9.1: Model geometry and experimental validation setup. A) The two-dimensional, axially-symmetric geometry of a clinical microwave antenna inserted within ex-vivo, homogenized bovine liver tissue. The dashed centerline denotes the symmetry axis. B) A cross-section of the experimental setup as seen under computed tomography (CT) imaging.

Energy conservation included convection, diffusion, conduction, phase change of water and microwave heating source, which were described using:

$$\frac{\partial}{\partial t}\left(\sum_{i=s,w,v}\rho_i C_{\rho,i} T\right) + \nabla\left(\sum_{i=w,v}\rho_i C_{\rho,i} u_i T\right) = \nabla(k_{eff}\cdot\nabla T) - \lambda\dot{I} + Q \qquad (9.2)$$

where ρ was the density (kg/m3), C_ρ was the specific heat (kJ/kg), T was the

temperature (K), λ was the latent heat of water vaporization (2,435 kJ/kg), k_{eff} was the effective thermal conductivity calculated as a weighted mean of thermal conductivities of constituent species, solid (s), liquid water (w) and water vapor (v).

The governing equation for water and vapor saturation within the tissue was given by a conservation of mass relation:

$$\frac{\partial c_i}{\partial t} + \nabla \cdot (-D_i \nabla C_i) + u_i \cdot \nabla C_i = \frac{\dot{I}}{M_w} \tag{9.3}$$

where C_i (mol/m^3) was the concentration of species (water or vapor), D_i (m^2/s) was the diffusivity and u_i was the convective (Darcy's) velocity of fluid. The right-hand side of (9.3), with units $(mol/m^3 \cdot s)$ represents the reaction term describing water vaporization or condensation, where M_w (18 g/mol) was the water molecular weight and $\dot{I}$ $(kg/s \cdot m^3)$ was the water vaporization rate. Darcy's law was used to describe the convective flows of liquid water and water vapor caused by pressure gradients within the tissue:

$$u_i = -\frac{k_{in,i} \cdot k_{r,i}}{u_i} \nabla p \quad (m/s) \tag{9.4}$$

where $k_{in,i}$ (m^2) is the intrinsic permeability, $k_{r,i}$ is the relative permeability, $_i$ $(Pa \cdot s)$ is the viscosity, p (Pa) is the vapor pressure.

Darcy's Law was combined with the continuity equation to solve for the pressure and velocity of the water vapor:

$$\frac{\partial}{\partial t}(\rho\phi) + \nabla \cdot (\rho u_i) = \dot{I} \tag{9.5}$$

where ϕ was porosity, defined as the fraction of the domain that is occupied by pores, which can vary from zero for pure solid regions to unity for domains of free flow. The pressure at the domain boundaries was set to be atmospheric to mimic

experimental conditions

Evaporation Rate Determination

In tissue, the liquid and vapor phases of water are assumed to in equilibrium. The equilibrium vapor pressure ($P_{v,eq}, Pa$) at a particular moisture content and temperature was described by the moisture isotherm [204],

$$\ln \frac{P_{v,eq}}{P_{sat(T)}} = -0.0267M^{-1.65} + 0.01e^{1.287M}M^{1.5}\ln[P_{sat}(T)] \tag{9.6}$$

where, P_{sat} (Pa) was the saturated vapor pressure of pure water, and M was the moisture content on dry basis. The phase change of water (vaporization) was described using non-equilibrium evaporation method [205]:

$$\dot{I} = \tau \frac{P_{v,eq} - P_v}{RT} \quad (kg/s \cdot m^3) \tag{9.7}$$

where P_v was the vapor density (kg/m^3), τ was a parameter signifying the rate constant of vaporization, which was of the order of 1 for hygroscopic material estimated in previous literature [205].

Boundary Conditions

For solving Maxwell's equations, a scattering boundary condition was imposed at the outer surface of the homogenized liver sample. Water vapor in the tissue was assumed to be transported by both diffusion and convection. At the tissue-air boundary

$$n_{v,sur} = c_v \cdot v_{n,v} + D_v \cdot \nabla c_v \quad (kg \cdot m^{-2} \cdot s^{-1}) \tag{9.8}$$

where $n_{(v,sur)}$ was the total mass flux through the surface of the tissue, c_v was the vapor concentration on tissue boundaries, $v_{n,v}$ was effective vapor velocity on tissue boundaries and D_v was vapor diffusivity in air. Along with the mass transport of species, the tissue boundaries also lose heat q_n because of the vapor loss, as well as cooling by ambient air

$$q_n = n_{v,sur} \cdot C_{p,v} T + h \cdot (T_{air} - T) \quad (W \cdot m^{-2}) \tag{9.9}$$

where $C_{p,v}$ was the specific heat of water vapor$(kJ/kg \cdot K)$ and h was the convective heat transfer coefficient of vapor at the surface $(W/m^2 \cdot K)$.

Table 1 shows the key input variables and their values. Several of these parameters in the model were adopted from previous studies focused on microwave heating in porous media [200, 202, 203].

Model Assumptions

A number of simplifying assumptions were made to facilitate simulation of the microwave ablation process. Initial uniform water content of 80%, which also accounted for residual fat [206]. The liver architecture was set to 80% porous structure, as estimated from foodstuff literature [207]. No consideration of tissue contraction in the heating zone and movement of gas though the antenna periphery was given [107]. Lastly, the vapor from the boundaries was assumed to be free to move within the homogenized liver sample.

Simulation Strategy and Comparison

The electromagnetic power dissipation rate (9.1) was solved using time-harmonic Maxwell's equations and the remaining heat (9.2), mass (9.3) and continuity (9.4,9.5)

transfer equations were solved using the transient solver. Segregated solvers were used for calculating temperature, water/ vapor velocities, and water/vapor concentrations. For rapid convergence, a boundary layer mesh was created at the antenna-tissue interface. An input power of 50 W was applied for 300 seconds.

As a comparison, a thermal conduction-only model was also created, using the same initial electromagnetic model in the microwave ablation as the heat source. The thermal conduction – only model was compared against the water vapor model using temperature outputs at 5 mm, 10 mm and 20 mm away from the antenna. Comparisons were made at 10 second intervals for the entire ablation period between each model.

9.3.2 Experimental Liver Setup

Samples of ex-vivo bovine liver tissue (n=5) were homogenized in order to eliminate the influence of larger hepatic vessels on the temperature and water-content profile while providing a more uniform testing medium. A clinical microwave ablation antenna (Neuwave Medical Inc, Madison, WI) was placed near the center of the homogenized liver sample at a depth of 6 cm. Ablations were created using a generator output of 90 W at 2.45 GHz for 300 s, which corresponded to a power deposition of approximately 50 W in tissue after accounting for cable and losses. During the ablation, computed tomography (CT) data were acquired over the entire tissue volume every 15 seconds (120 kVp, 200 mA, 512 $\times$ 512, 1 1 helical pitch, 0.625 mm slice thickness; Discovery 750 HD, GE Healthcare, Milwaukee, WI). CT volumes were co-registered using rigid assumptions and the antenna tip as a fiducial marker. CT data were then averaged over all experimental samples at each time point to produce a single composite dataset for comparison to the numerical modeling results.

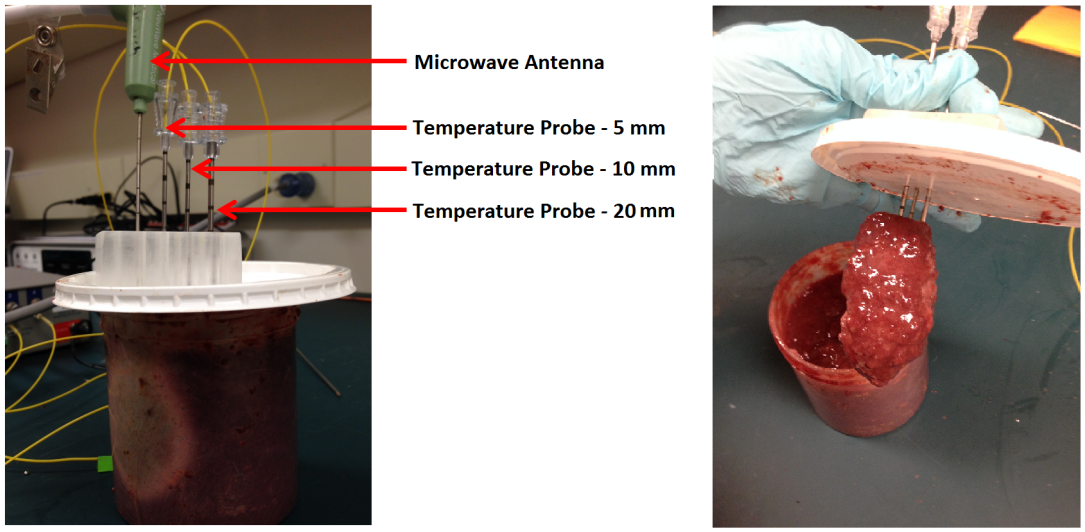

Figure 9.2: Experimental setup for the homogenized liver model. A) Fiber-optic temperature probes were placed 5, 10 and 20 mm away from the microwave antenna. Ablations were created at 100 W for 5 minutes. B) Post-ablation visualization of the homogenized liver. The heating zone near the antenna has desiccated and collapsed upon the microwave antenna and temperature probes.

This homogenized liver ablation setup was then repeated with fiber-optic temperature probes placed 5 mm, 10 mm and 20 mm away from the microwave antenna. The temperature probes were placed flush with the plane of maximal heating. Microwave ablations were created at 90 W for 300 seconds. Mean temperatures at each location were averaged across samples (n=5) and used as a comparison against the numerical models **(Figure 9.2)**.

As a point of comparison against normal tissue, a microwave ablation setup was created using an excised ex-vivo bovine liver block. Fiber-optic temperature probes were placed 5 mm, 10 mm and 20 mm away from a microwave antenna. Ablations were created at 90 W for 150 seconds. Mean temperatures at each location were averaged across samples (n=6) and temperatures were compared against the homogenized liver sample at each spatial and time point.

9.3.3 Parametric Study and Validation

A preliminary study was performed to find a reliable vapor concentration that mapped well to experimental CT Hounsfield units of the vapor map. The vapor map was resized to match the resolution of the CT scans. The area enclosed within simulated vapor concentrations of 1%, 5%, 10% and 50% were compared against CT images thresholded at -200, -400, -600 and -800 HU. Similarity between the simulated and experimental image masks, A and B, respectively, was calculated using the Jaccard index, J [208]:

$$J(A, B) = \frac{A \cap B}{A \cup B} \tag{9.10}$$

where greater Jaccard indices (from 0 to 1) implied more precise correlation between the computational model and experimental data. The vapor concentration and CT threshold pair that yielded the greatest Jaccard index was used to compare simulated and experimental data in later analyses.

9.4 Results

9.4.1 Numerical Simulation and Comparison

Simulation of the fully coupled computational model for 47,635 triangular elements required 30 minutes on a 2.4 GHz Xeon processor work station with 24 GB RAM.

Qualitatively, the numerical model predicted an elongated pattern of vapor movement along the shaft of the antenna for the first two minutes, followed by a movement predominantly outward from the antenna until the end of the ablation procedure. The simulated rate of radial and longitudinal ablation zone growth was greatest at the beginning of the heating cycle, then decreased over time as noted in

previous experimental studies [81, 209].

The temperature output from the numerical model at discrete points 5-20 mm away from the microwave antenna and its comparison to the homogenized liver experiment is summarized in **Figure 9.3A**. The water vapor model 5 mm away from the microwave antenna exceeded 80 °C within the first two minutes of the ablation before leveling off at 90-100 °C. This plateau-effect is consistent with energy being absorbed during the phase transformation from water to vapor [103]. Temperatures simulated at more peripheral locations exhibited a much slower increase to lower levels, as expected. The experimental model with the homogenized liver model matched that of the computational model accurately, but demonstrated a plateau at a higher temperature that was a slightly lower than 100 °C. Temperature comparisons at distances of 10 mm and 20 mm, where the water remained in liquid form, showed excellent correlation between the numerical model and homogenized liver model.

Converse to the homogenized liver model, validation with the ex-vivo liver blocks demonstrated a lack of consistency in temperature measurements at all discrete points, After 1 minute of heating, the temperature at the 10 mm and 20 mm locations were approximately 20 °C higher in the ex-vivo liver blocks compared to the homogenized liver samples. This difference was also seen in the 5 mm location but was minimized as the temperature peaked as the temperature approached 100 °C **(Figure 9.3B)**.

CT Imaging Study

CT-imaging showed trends in water vapor formation and growth inside the homogenized liver solution that reflected simulation results. Water vapor appeared as a gradient from complete liquid water in normal tissue (0 HU) to pure water vapor (-1000 HU), with some variation coming from the liver tissue backdrop. Very little

vapor was observed in the sample periphery, as indicated by the lack of change seen in the radiodensity for liver tissue (50 HU). Significant water vapor generated near the antenna reduced attenuation to levels associated with highly aerated tissue (-800 HU). Towards the end of the heating period, pockets of water vapor were observed migrating to discrete positions away from the ablation zone. These vapor-filled pockets collapsed after the heating source was turned off, marking an almost immediate phase change from water vapor to liquid in the absence of a microwave energy input. This rapid phase change is expected due to the continuous heating rate necessary to overcome the enthalpy of vaporization of liquid water (40.65 kJ/mol), a value five times higher than necessary to simply heat water to boiling temperature.

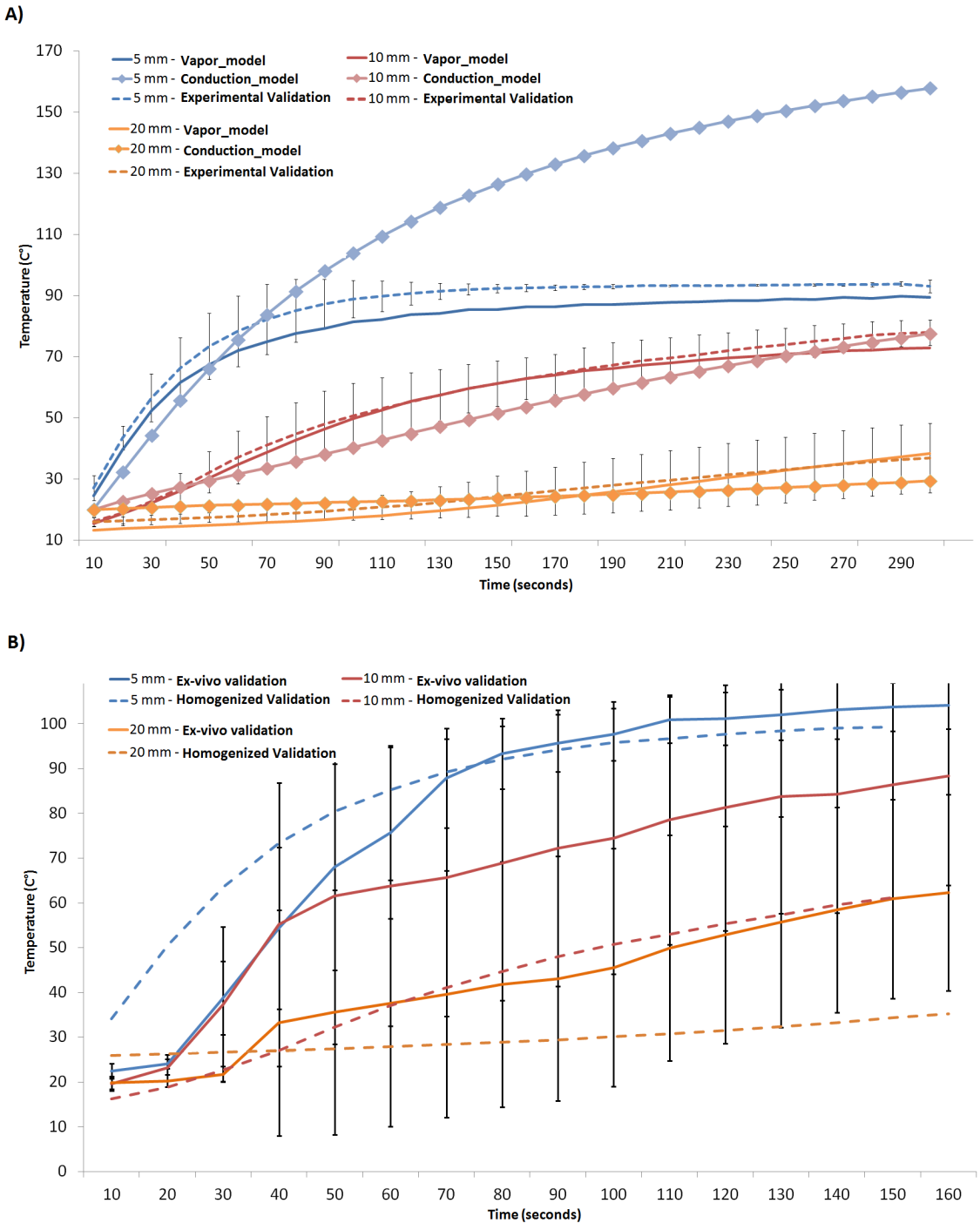

Figure 9.3: A) Temperature comparisons between the water vapor model, the thermal conduction model and the experimental validation at positions 5 mm, 10 mm and 20 mm away from the microwave antenna. B) Temperature comparisons between homogenized liver model and the ex-vivo liver model.

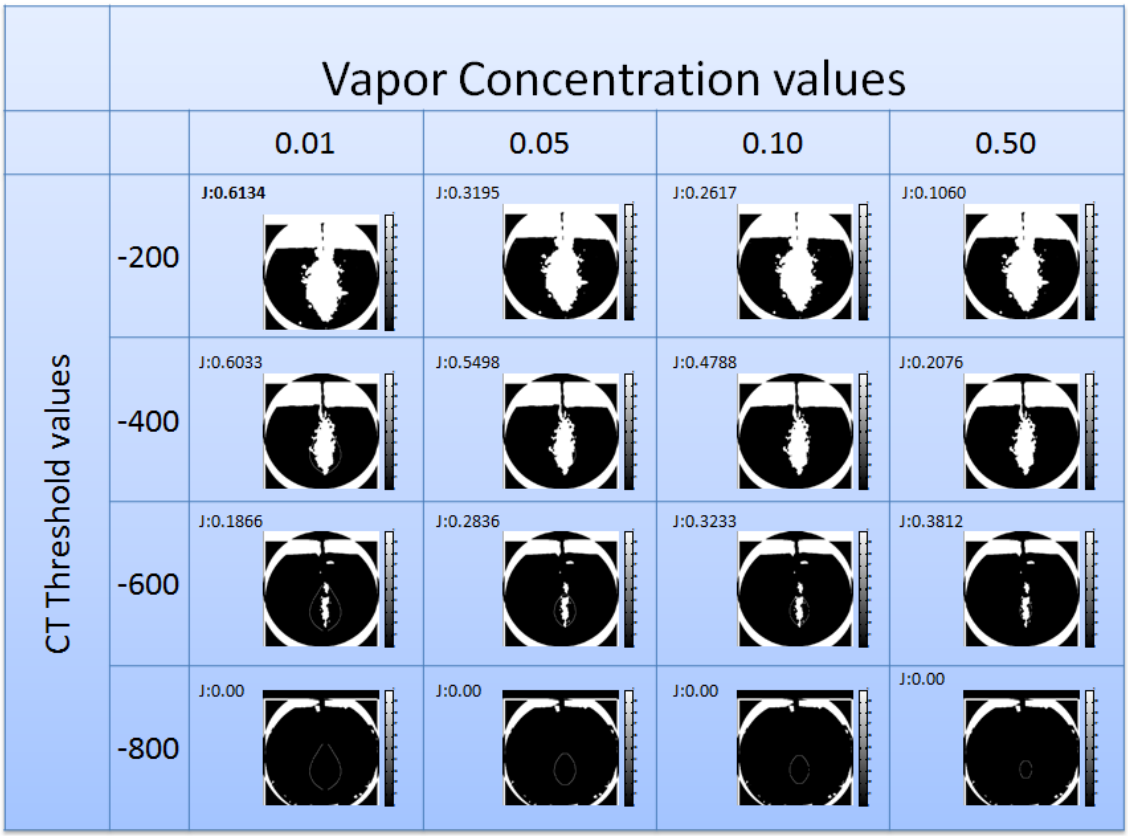

Figure 9.4: Parametric study comparing numerical concentration values against CT threshold values.

Parametric Study and Comparison

The preliminary study showed the highest Jaccard index value of 0.613 between the 1% water vapor threshold in our model and the -200 HU threshold in the experimental CT images. These values were used to define the boundaries on simulated and experimental vapor concentration maps (**Figure 9.4**).

Experimental water vapor cross-sectional profiles were somewhat larger than those of simulations, especially toward the distal portion of the heating zone. In contrast, the proximal portion of the ablation zone exhibited excellent correlation to the modeling data. The 1% vapor contour diameter reached 2.40 cm, 3.20 cm, 3.80 cm, 4.20 cm and 4.60 cm at 1, 2, 3, 4 and 5 minutes respectively (**Figure 9.5A**). These

measurements compared favorably with the corresponding -200 HU threshold map in the experimental data, which showed a diameter of 2.56 cm, 3.41 cm, 4.00 cm, 4.29 cm, and 4.45 cm at 1, 2, 3, 4 and 5 minutes respectively (**Figure 9.5B**). Similarity between the simulated and experimental vapor maps was somewhat limited for early ablation times (Jaccard index: 0.071 ± 0.039 at 15 seconds) but increased to a good correspondence at later time points (Jaccard index: 0.73 ± 0.130 at 300 s; **Figure 9.5C and 9.5D**).

9.5 Discussion

This study demonstrated the feasibility of adding water vapor creation and transport into heat transfer and electromagnetic physics during the simulation of microwave tissue heating. It also demonstrated a CT imaging technique to validate the numerical predictions of water vapor. Overall, good agreement was noted between simulated 1% vapor contours and CT images using a -200 HU threshold.

As ablation devices evolve and become integrated into the standards of care, treatment predictability, precision and efficacy will be expected to improve. One way to improve treatment performance is to utilize computer-aided design and optimization of devices and treatment parameters. However, simulations used to guide the design process require accurate models. Incorporating latent heat of vaporization and taking a porous media approach to account for the physical effects of water vapor have improved modeling precision at higher temperatures associated with microwave ablations in previous studies [103, 107, 108, 111]. However, those empirical models did not account for the formation of water vapor and therefore, were unable to investigate the effects of vapor formation and transport on ablation zone growth. The present study describes a framework based on porous media by

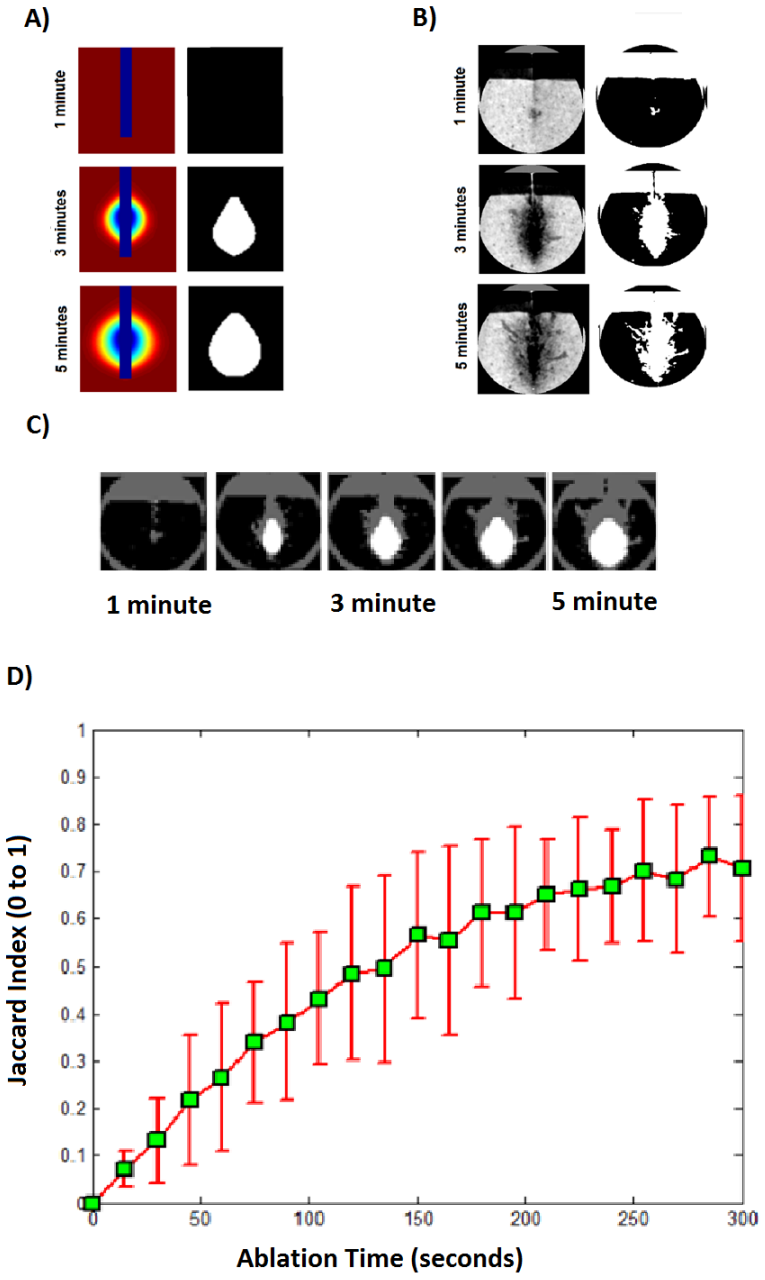

Figure 9.5: A) Computational model of a water vapor map during microwave ablation heating was created and thresholded at 1% vapor to find the outer boundaries of the ablation zone B) CT imaging was used to visualize the boundaries of the water vapor map using the -200 HU threshold. C) The boundaries of the simulated and experimental vapor maps were compared to each other at multiple time points. D) A similarity measure using the Jaccard Index was calculated across each time point in order to validate water vapor model.

which the effects of vapor formation and transport may now be studied. Further investigation into the interplay between the thermal, electrical and mass transport physics during heating will likely improve simulation accuracy and utility in the computer-aided design and treatment planning process.

Experimental validation was a critical component of this study. Previous studies utilized primarily visual inspection of ablation zones in tissue to compare computational and experimental results [81, 158, 209]. Tissue regions that were desiccated or blanched marked boundaries of the ablation zone, with more detailed observations utilizing histological analysis [40, 41, 210]. Likewise, tracking water vapor and moisture content had only been possible through dehydration techniques on post-ablation specimens [206]. Those studies were limited in that the samples could only be observed after the ablation zone had been created; temporal changes that occurred during the ablation procedure could not be observed. In this study, CT imaging was leveraged to successfully capture gas formation and transport in a homogenized liver tissue solution in real-time. CT images could be captured with spatial and temporal resolutions of 0.1875 mm/pixel and 15 seconds/scan, respectively, making it possible to observe high levels of vapor formation in the center of the heating zone and its subsequent outward movement into the tissue. Therefore, vapor concentration can be a measurable variable to track ablation growth over time in both computational and experimental models.

Temperature predictions from the numerical vapor model showed improved accuracy over models that utilized only thermal conduction, as seen in previous studies [111]. In previous numerical studies that did not account for vapor formation, simulated tissue temperatures far exceeded measured values in locations where water vapor was created since the latent heat of vaporization was not considered. Dielectric models designed to incorporate the effects of vapor formation

in temperature dependence have been shown to improve temperature correlation accuracy similar to the vapor model presented here [107]. With the prediction of water content realized in the present study, a numerical model of properties based on temperature and water content would likely improve the generality of simulations. In turn this would increase the applicability of simulations to a wider range of clinical goals.

Mismatches between simulated vapor maps and experimental results were observed, particularly in the beginning of the ablation procedure. Early water vapor formation was much faster in experiments than simulations, leading to a low level of overlap between the two contours and subsequently, a low Jaccard index. This mismatch decreased over time, but the larger cross sectional area of water vapor was consistently greater in experiments than simulations. Assumptions in the computational model likely played a significant factor in this mismatch. Thermal and dielectric properties of liver tissue were often described in its ex-vivo state, with water content comprising of up to 70% of the tissue. When the liver tissue was separated into its various constituents in the heat transfer model, the heat capacity and thermal conductivity were estimated based on water content. Intrinsic permeability and porosity assumptions related to the homogenized liver solution were estimated from foodstuff data as these properties were not readily available for liver tissue. Furthermore, assumed values may have changed during homogenization.

The homogenized liver model demonstrated more consistency and accuracy in validation efforts compared to the ex-vivo liver model. While the temperature measurements in the beginning of the heating were the same, there were significant differences between the two measurements. Ablations in the ex-vivo liver model heated the tissue at a faster rate and to higher temperatures compared to the homogenized liver model. This could be explained by the intact anatomical structures

in the liver, which offer resistance against free water vapor movement. As such, the water vapor remains localized in the tissue and can absorb even more energy. This is supported by the fact that temperature measurements at 5 mm in the ex-vivo liver tissue exceeded 100 °C within 2 minutes. The intact anatomical structure of the liver, which included micro- and macro-vasculature and lobular geometry, also disrupted the heating pattern of the ablation zone, resulting in large differences in temperature measurements between samples. Conversely, the homogenized liver sample showed much more consistency between samples and a more accurate validation of the numerical model could be performed.

The effects of atmospheric pressure and gravity, which contribute to the propensity for vapor to move upwards in the homogenized liver, were also not considered in the numerical model. The seemingly larger volume of vapor formation in the experiments compared to numerical models could also be attributed to more direct water contact with the microwave antenna, since the individual hepatic sinusoids and anatomic structures no longer compartmentalized the fluid. Increased concentration of liquid water volume could potentially lead to increased water vapor formation that was not accounted for in the model. The computational model also did not account for tissue contraction, which had been shown to occur as water vapor dissipates from the heating zone [112]. Contraction for homogenized liver solution during heating, although not characterized yet, could potentially affect porosity and diffusion constants associated with vapor transport. Refinement in model inputs and assumptions is clearly needed. However, despite the large number of simplifying assumptions good overall agreement between the simulation and model were noted.

The trends observed in vapor concentration prediction, temperature modeling and experimental data point to future studies correlating intra-procedural CT imag-

ing of water vapor in tissue to actual ablation sizes. Compared to gross pathology measurements from past microwave ablation studies in ex-vivo tissue, the water vapor sizes in both our model and experimental study had a slightly larger diameter at each time point during the ablation [206, 209]. It is difficult to make direct comparisons due to differences in vapor presence and actual thermal coagulation, as well as multiple physical parameters such as energy delivery, tissue porosity and electrical properties. However, we found that the rate of linear growth in vapor size mapping and the ablation size from gross pathology to be comparable at multiple time points.

9.6 Conclusion

This study demonstrated the potential of incorporating water and water vapor mass transport physics into the simulation of microwave thermal ablations. CT imaging was used as a real-time tool to monitor water vapor during experimental studies, and could therefore be applied to validate the simulation model. The new model may help to improve the accuracy of microwave ablation simulations, allow more arbitrary analysis of ablation inputs with relevant underlying physics, and facilitate the analysis of heat and mass transfer contributing to thermal ablation growth.

Chapter 10

Summary and Recommendations

10.1 Summary

The heating advantages of microwave ablation systems over predecessor technologies have been well established. Creating larger and hotter ablation zones with microwave energy have afforded physicians the ability to treat larger tumors as well as tumors located in the vicinity of blood vessels. However, the high temperatures associated with microwave ablation devices have changed how we model thermal ablations, design ablation devices and optimize ablation treatments. The contribution of this work is as follows:

- The design and optimization of a cooled dual-slot antenna that integrated the cooling component, ceramic and tip into the bare coaxial design.
- The validation study in ex-vivo and in-vivo animal models to confirm the performance of the cooled dual-slot antenna. The validation study required the novel use of intra-procedural CT imaging of the water vapor formation.
- The development and validation of the numerical model integrating fluid flow with microwave heating near a blood vessel inside liver tissue. The design of this model also involved taking measurement of temperature-dependent viscosity of heparinized porcine blood in order to accurately predict the effects of cytotoxic temperatures on blood.
- The design and execution of an in-vivo study of the effects of microwave tumor ablation on the portal vein, hepatic vein and hepatic arteries. The rates of thrombosis inside these vessels were modeled as a logistic function and can be easily adapted to help guide antenna placement.
- The design and execution of experimental studies to elucidate the mechanism of thrombosis inside the hepatic vasculatures. The physical mechanism studies

looked at temperature and pressure changes within vessels during microwave ablation. The biological mechanism studies investigated the differences in pro-thrombotic gene expression between normal, untreated portal and hepatic veins.

- The design and execution of the water moisture study, using single-energy and dual-energy CT to investigate the relationship between water moisture levels in ex-vivo liver tissue and its respective radiodensity.

- The design of the validation study integrating previously-developed water vapor heating models into our own microwave ablation models. The study required the development of a homogenized liver model as well as intra-procedural CT scanning to provide a validation frame for each time point. The study also required a temperature measurement component between the vapor model and the conduction-only model. The homogenized liver model was also compared against ex-vivo liver tissue in order to characterize the differences in heating pattern.

10.2 Future Direction

There is additional work that is needed to continue improving our understanding of how to best utilize the high energy and heat associated with microwave ablation systems to treat patients. The directions can be broadly categorized into the following categories:

10.2.1 Antenna Design

The final cooled dual-slot antenna design was found through a parametric algorithm. While the performance of the dual-slot antenna in terms of aspect ratio and reflection coefficient was superior to monopole antenna designs, the fabrication process was constrained by the tolerance of our manufacturing process. The analysis detailed in Chapter 3 showed that the antenna performance remained robust to various lengths of the inner feeding slot but highly sensitive to the length of the ceramic-steel catheter overlap. Thus, small changes to the ceramic-steel overlap could result in large drops in antenna performance, or even a non-functioning antenna.

Some potentially interesting antenna designs may result from looking at multi-modal antenna designs. For electromagnetic boundary-value problems, there are many field configurations (modes) that satisfy Maxwell's equations. The majority of the solutions associated with our antenna problems were found by solving for Maxwell's equations in the transverse magnetic (TM) mode, where the magnetic field component lies in a plane transverse to a given direction. It would be possible to perform the same analysis using the transverse electric (TE) mode, where the electric field component is transverse to a given direction. Another antenna design optimization path that has already been incorporated in modern day communication systems is using multi-modal transmission systems. Based on the mode wave numbers (eigenvalues), it is possible to deliver energy at more than one range of frequencies. This can be useful when considering the electrical properties of liver tissue and how it changes as water is driven out during the ablation procedure. Some challenges that need to be overcome are how to optimize not only the geometry of the antenna but the total power distribution among the existing modes, which can be complex and expensive to implement.

Lastly, the dual-slot antenna design was derived from a cost function-driven

parametric study, rather than a true optimization approach. Optimization from a quasi-Newtonian, genetic or Bayesian algorithm may lead to other suitable antenna designs. An additional factor to weigh into a successful antenna design may be the integration of an ease-of manufacturing to a particular design. Designs that have more continuous shapes and can be easier to fabricate should be considered in the final antenna design.

10.2.2 Validation Techniques

Validation of antenna designs and numerical models remains an area of controversy. Temperature measurements and gross pathology imaging remain the gold standard for ablation zone validation. Temperature measurements provide excellent temporal resolution but are sensitive to movement during the ablation, which occurs during tissue contraction. Temperature measurements are also limited to the specific point that is being measured, and reveals only a small fraction of the entire heating process. Liver tissue is highly vascularized and lobar, leading to large inconsistencies in ablation zones from sample to sample. Ablations in ex-vivo liver models often result in ablation zones larger than what would be normally seen in human liver tumors due to the absence of the cooling blood flow. On the other hand, ablations in in-vivo liver models result in ablation zones smaller than what is seen in human liver tumors due to the absence of tortuous vasculature and tumor environment.

The homogenized liver model maintains the cellular components of liver, but devoid of the anatomical structures and vasculature. The electrical and thermal properties of the homogenized liver were not validated against ex-vivo or in-vivo liver tissues but are believed to be of similar values. As shown in the Chapter 9, the temperature measurements made inside the homogenized liver sample are much more consistent from sample to sample compared to those made inside ex-vivo

liver tissue. Validation of previous antenna designs utilizing these water vapor markers can provide details on the heating pattern of the ablation zone that were not previously available. However, further characterization of the homogenized ablation zone is needed in order to translate its results into usable data.

As seen in Chapter 5, there are limitations to what can be studied using an agar phantom to experimentally study blood flow near an ablation zone. An ex-vivo flow model using a transplant clinic setup with heparinized blood, may potentially offer a more accurate model for validating ablation zone behavior near vasculature.

10.2.3 Vascular Damage and Associated Risks

In that same vein (pun intended), the precise mechanism by which thermal ablation zones affect nearby blood vessels is unclear. While we have established that hepatic veins are more prone to acting as a heat sink by virtue of being resistant to thrombus formation, there is still much work required to clarify the underlying mechanism. Furthermore, from a practical standpoint, our regression models did not fully predict when thrombus would form in portal veins, despite occurring significantly more often compared what was seen in hepatic veins.

As a logical follow-up study, a retrospective clinical imaging study looking at thrombus formation in portal and hepatic veins near ablation zones would be useful in confirming our in-vivo study trends. Additionally, follow-up imaging extending up to six months after the ablation procedure would reveal the long-term effects of vascular damage. Based on our in-vivo studies, we would expect that delayed portal vein thrombus formation would occur at a similarly high rate compared to hepatic veins.

There are currently few explanations as to why portal veins thrombose more than hepatic veins. One obvious difference lies in the flow pattern, which has

been well documented with Doppler imaging. Hepatic veins, which feed into the inferior vena cava, experience a regularly pulsatile flow pattern, reflective of the cardiac cycle. Portal veins, on the other hand, feed into the highly resistive network of capillaries and sinusoids, resulting in a more continuous, non-pulsatile flow. Our gene expression study also highlights underlying differences in pro- and anti-thrombotic genes between portal and hepatic veins. Validation studies looking at pigs with various pulsatility patterns or genetic deficiencies in endothelial clotting proteins may narrow down the number of potential mechanisms contributing to this phenomenon.

A mechanistic study would be useful in that it may allow physicians to target specific pathways to optimize ablation treatment. As mentioned in Chapter 6 and 7, physicians may want to thrombose vessels to improve ablation zone efficacy near blood vessels and reduce the chance of recurrence. At the same time, however, they do not want to cause damage to larger vessels that supply entire liver lobes. Recognizing the environment that predisposes vessels to thrombosis will be critical in improving ablation treatment performance and associated patient outcomes.

10.2.4 Water Vapor Model and Analysis

The incorporation of water vapor formation and subsequent movement through tissue has offered improved simulation results to our numerical simulations. Previous studies have accounted for water vaporization by adding a latent heat of vaporization term or by incorporating temperature-dependence to the electrical properties of liver tissue. These updated model inputs have led to numerical results that match up closer to experimental validation studies than previous simulations using simple passive thermal conduction. Utilizing the high temperatures associated with microwave to drive water vapor movement through a porous media approach has also

led to similarly accurate temperature mappings. The actual change in dielectric and thermal conductivity during heating potentially lies in a combination of water vapor and temperature dependence. Treating water vapor formation and temperature as separate inputs to thermal and electrical properties of liver could potentially lead to improved simulation accuracy.

While the current water vapor model accounts for the change in energy as water turns into vapor, there is currently no consideration for the phase change occurring when vapor changes back into water. Incorporating this additional energy release, especially near the edge of the ablation zone would better characterize the total damage from water vaporization. Improved model inputs such as the porosity, saturation and pressure would also be useful, although a sensitivity study should also be carried out.

As with all numerical studies, the water vapor model requires validation. The CT-derived vapor maps detailed in Chapter 9 provides only the outer boundary of the vapor zone. A challenge that would need to be overcome is a method of actually quantifying the amount of liquid water and water vapor inside an ablation zone. Conventional methods of desiccation and mass measurements can be time consuming and highly variable to the surrounding environment. A rapid way of deriving water content would be more appropriate option if this study were to be carried out due to the vast number of time points and samples required to make a comparison. Ultimately, an imaging technique that could provide good temporal and spatial resolution would be the ideal method for water vapor validation.

Bibliography

1. Braillon A, Dubois G. Hepatocellular carcinoma and industrial epidemics. World J Gastroenterol WJG. 2011 Jun 28;17(24):2976.

2. El-Serag HB. Hepatocellular carcinoma. N Engl J Med. 2011 Sep 22;365(12):1118–27.

3. Sherman M. Epidemiology of hepatocellular carcinoma. Oncology. 2010 Jul;78 Suppl 1:7–10.

4. Chen C-J, Yang H-I, Iloeje UH, REVEAL-HBV Study Group. Hepatitis B virus DNA levels and outcomes in chronic hepatitis B. Hepatol Baltim Md. 2009 May;49(5 Suppl):S72–84.

5. Beasley RP, Hwang LY. Hepatocellular carcinoma and hepatitis B virus. Semin Liver Dis. 1984 May;4(2):113–21.

6. Donato F, Tagger A, Gelatti U, Parrinello G, Boffetta P, Albertini A, et al. Alcohol and hepatocellular carcinoma: the effect of lifetime intake and hepatitis virus infections in men and women. Am J Epidemiol. 2002 Feb 15;155(4):323–31.

7. Wolk A, Gridley G, Svensson M, Nyrén O, McLaughlin JK, Fraumeni JF, et al. A prospective study of obesity and cancer risk (Sweden). Cancer Causes Control CCC. 2001 Jan;12(1):13–21.

8. Llovet JM, Bruix J. Systematic review of randomized trials for unresectable hepatocellular carcinoma: Chemoembolization improves survival. Hepatol Baltim Md. 2003 Feb;37(2):429–42.

9. Mazzaferro V, Battiston C, Perrone S, Pulvirenti A, Regalia E, Romito R, et al. Radiofrequency ablation of small hepatocellular carcinoma in cirrhotic patients awaiting liver transplantation: a prospective study. Ann Surg. 2004 Nov;240(5):900–9.

10. Weis S, Franke A, Mössner J, Jakobsen JC, Schoppmeyer K. Radiofrequency (thermal) ablation versus no intervention or other interventions for hepatocellular carcinoma. Cochrane Database Syst Rev. 2013 Dec 19;12:CD003046.

11. Ahmed M, Brace CL, Lee FT, Goldberg SN. Principles of and advances in percutaneous ablation. Radiology. 2011 Feb;258(2):351–69.

12. Bruix J, Sala M, Llovet JM. Chemoembolization for hepatocellular carcinoma. Gastroenterology. 2004 Nov;127(5, Supplement 1):S179–S188.

13. Cescon M, Cucchetti A, Ravaioli M, Pinna AD. Hepatocellular carcinoma locoregional therapies for patients in the waiting list. Impact on transplantability and recurrence rate. J Hepatol. 2013 Mar;58(3):609–18.

14. Lammer J, Malagari K, Vogl T, Pilleul F, Denys A, Watkinson A, et al. Prospective randomized study of doxorubicin-eluting-bead embolization in the treatment of hepatocellular carcinoma: results of the PRECISION V study. Cardiovasc Intervent Radiol. 2010 Feb;33(1):41–52.

15. Salem R, Lewandowski RJ, Mulcahy MF, Riaz A, Ryu RK, Ibrahim S, et al. Radioembolization for hepatocellular carcinoma using Yttrium-90 microspheres: a comprehensive report of long-term outcomes. Gastroenterology. 2010 Jan;138(1):52–64.

16. Edwards BK, Noone A-M, Mariotto AB, Simard EP, Boscoe FP, Henley SJ, et al. Annual Report to the Nation on the status of cancer, 1975-2010, featuring prevalence of comorbidity and impact on survival among persons with lung, colorectal, breast, or prostate cancer. Cancer. 2013 Dec 16;

17. Gillams A, Khan Z, Osborn P, Lees W. Survival after radiofrequency ablation in 122 patients with inoperable colorectal lung metastases. Cardiovasc Intervent Radiol. 2013 Jun;36(3):724–30.

18. Choti MA, Sitzmann JV, Tiburi MF, Sumetchotimetha W, Rangsin R, Schulick RD, et al. Trends in long-term survival following liver resection for hepatic colorectal metastases. Ann Surg. 2002 Jun;235(6):759–66.

19. Fong Y, Cohen AM, Fortner JG, Enker WE, Turnbull AD, Coit DG, et al. Liver resection for colorectal metastases. J Clin Oncol Off J Am Soc Clin Oncol. 1997 Mar;15(3):938–46.

20. Rougier P, Milan C, Lazorthes F, Fourtanier G, Partensky C, Baumel H, et al. Prospective study of prognostic factors in patients with unresected hepatic metastases from colorectal cancer. Fondation Française de Cancérologie Digestive. Br J Surg. 1995 Oct;82(10):1397–400.

21. Adam R. Chemotherapy and surgery: new perspectives on the treatment of unresectable liver metastases. Ann Oncol Off J Eur Soc Med Oncol ESMO. 2003;14 Suppl 2:ii13–16.

22. Nordlinger B, Sorbye H, Glimelius B, Poston GJ, Schlag PM, Rougier P, et al. Perioperative chemotherapy with FOLFOX4 and surgery versus surgery alone for resectable liver metastases from colorectal cancer (EORTC Intergroup trial 40983): a randomised controlled trial. Lancet. 2008 Mar 22;371(9617):1007–16.

23. Cho YK, Rhim H, Noh S. Radiofrequency Ablation versus Surgical Resection as Primary Treatment of Hepatocellular Carcinoma Meeting the Milan Criteria: A Systematic Review. J Gastroenterol Hepatol. 2011 Jun 16.

24. Montorsi M, Santambrogio R, Bianchi P, Donadon M, Moroni E, Spinelli A, et al. Survival and recurrences after hepatic resection or radiofrequency for hepatocellular carcinoma in

cirrhotic patients: a multivariate analysis. J Gastrointest Surg Off J Soc Surg Aliment Tract. 2005 Jan;9(1):62–67; discussion 67–68.

25. Vivarelli M, Guglielmi A, Ruzzenente A, Cucchetti A, Bellusci R, Cordiano C, et al. Surgical resection versus percutaneous radiofrequency ablation in the treatment of hepatocellular carcinoma on cirrhotic liver. Ann Surg. 2004 Jul;240(1):102–7.

26. Chen M-S, Li J-Q, Zheng Y, Guo R-P, Liang H-H, Zhang Y-Q, et al. A prospective randomized trial comparing percutaneous local ablative therapy and partial hepatectomy for small hepatocellular carcinoma. Ann Surg. 2006 Mar;243(3):321–8.

27. Huang J, Hernandez-Alejandro R, Croome KP, Yan L, Wu H, Chen Z, et al. Radiofrequency ablation versus surgical resection for hepatocellular carcinoma in Childs A cirrhotics-a retrospective study of 1,061 cases. J Gastrointest Surg Off J Soc Surg Aliment Tract. 2011 Feb;15(2):311–20.

28. Feng K, Yan J, Li X, Xia F, Ma K, Wang S, et al. A randomized controlled trial of radiofrequency ablation and surgical resection in the treatment of small hepatocellular carcinoma. J Hepatol. 2012 Oct;57(4):794–802.

29. Santambrogio R, Opocher E, Zuin M, Selmi C, Bertolini E, Costa M, et al. Surgical resection versus laparoscopic radiofrequency ablation in patients with hepatocellular carcinoma and Child-Pugh class a liver cirrhosis. Ann Surg Oncol. 2009 Dec;16(12):3289–98.

30. Guglielmi A, Ruzzenente A, Valdegamberi A, Pachera S, Campagnaro T, D'Onofrio M, et al. Radiofrequency ablation versus surgical resection for the treatment of hepatocellular carcinoma in cirrhosis. J Gastrointest Surg Off J Soc Surg Aliment Tract. 2008 Jan;12(1):192–8.

31. Lupo L, Panzera P, Giannelli G, Memeo M, Gentile A, Memeo V. Single hepatocellular carcinoma ranging from 3 to 5 cm: radiofrequency ablation or resection? HPB. 2007;9(6):429–34.

32. Hong SN, Lee S-Y, Choi MS, Lee JH, Koh KC, Paik SW, et al. Comparing the outcomes of radiofrequency ablation and surgery in patients with a single small hepatocellular carcinoma and well-preserved hepatic function. J Clin Gastroenterol. 2005 Mar;39(3):247–52.

33. Sato M, Watanabe Y, Ueda S, Iseki S, Abe Y, Sato N, et al. Microwave coagulation therapy for hepatocellular carcinoma. Gastroenterology. 1996 May;110(5):1507–14.

34. Castle S. In vivo microwave-induced porcine kidney thermoablation: results and perspectives from pilot study of a new probe? BJU Int. 2010 Dec;106(11):1825–1826;.

35. Wolf FJ, Grand DJ, Machan JT, Dipetrillo TA, Mayo-Smith WW, Dupuy DE. Microwave ablation of lung malignancies: effectiveness, CT findings, and safety in 50 patients. Radiology. 2008 Jun;247(3):871–9.

36. Lu DSK, Raman SS, Limanond P, Aziz D, Economou J, Busuttil R, et al. Influence of large peritumoral vessels on outcome of radiofrequency ablation of liver tumors. J Vasc Interv Radiol JVIR. 2003 Oct;14(10):1267–74.

37. Yu NC, Raman SS, Kim YJ, Lassman C, Chang X, Lu DSK. Microwave liver ablation: influence of hepatic vein size on heat-sink effect in a porcine model. J Vasc Interv Radiol JVIR. 2008 Jul;19(7):1087–92.

38. Dodd GD 3rd, Dodd NA, Lanctot AC, Glueck DA. Effect of Variation of Portal Venous Blood Flow on Radiofrequency and Microwave Ablations in a Blood-perfused Bovine Liver Model. Radiology. 2013 Jan; 267(1):129-36

39. Livraghi T, Meloni F, Di Stasi M, Rolle E, Solbiati L, Tinelli C, et al. Sustained complete response and complications rates after radiofrequency ablation of very early hepatocellular carcinoma in cirrhosis: Is resection still the treatment of choice? Hepatol Baltim Md. 2008 Jan;47(1):82–9

40. Bhardwaj N, Strickland AD, Ahmad F, Atanesyan L, West K, Lloyd DM. A comparative histological evaluation of the ablations produced by microwave, cryotherapy and radiofrequency in the liver. Pathology (Phila). 2009 Feb;41(2):168–72

41. Bhardwaj N, Dormer J, Ahmad F, Strickland AD, Gravante G, Beckingham I, et al. Heat Shock Protein 70 Expression Following Hepatic Radiofrequency Ablation is Affected by Adjacent Vasculature. J Surg Res; 2010 Oct 23.

42. Brace CL. Temperature-dependent dielectric properties of liver tissue measured during thermal ablation: toward an improved numerical model. Conf Proc Annu Int Conf IEEE Eng Med Biol Soc IEEE Eng Med Biol Soc Conf. 2008;2008:230–3.

43. De Lope CR, Tremosini S, Forner A, Reig M, Bruix J. Management of HCC. J Hepatol. 2012;56 Suppl 1:S75–87.

44. Brace CL. Radiofrequency and microwave ablation of the liver, lung, kidney, and bone: what are the differences? Curr Probl Diagn Radiol. 2009 Jun;38(3):135–43.

45. Pusceddu C, Sotgia B, Fele RM, Melis L. Treatment of Bone Metastases with Microwave Thermal Ablation. J Vasc Interv Radiol. 2013 Feb; 24(2):229-33

46. Tanaka T, Westphal S, Isfort P, Braunschweig T, Penzkofer T, Bruners P, et al. Microwave ablation compared with radiofrequency ablation for breast tissue in an ex vivo bovine udder model. Cardiovasc Intervent Radiol. 2012 Aug;35(4):914–20.

47. Zhou W, Zha X, Liu X, Ding Q, Chen L, Ni Y, et al. US-guided percutaneous microwave coagulation of small breast cancers: a clinical study. Radiology. 2012 May;263(2):364–73.

48. Li X, Fan W, Zhang L, Zhao M, Huang Z, Li W, et al. CT-guided percutaneous microwave ablation of adrenal malignant carcinoma: preliminary results. Cancer. 2011 Nov 15;117(22):5182–8.

49. Carrafiello G, Laganà D, Mangini M, Fontana F, Dionigi G, Boni L, et al. Microwave tumors ablation: principles, clinical applications and review of preliminary experiences. Int J Surg Lond Engl. 2008;6 Suppl 1:S65–69.

50. Fresno-Alba S, DeLlera-Duarte A, Vidal-Roncero H, Usandizaga R, DeSantiago-Garcia J, Zapardiel I. [Endometrial ablation: comparative study between hysteroscopic resection and Novasure system]. Ginecol Obstet México. 2013 Apr;81(4):175–9.

51. Laeseke PF, Winter TC 3rd, Davis CL, Stevens KR, Johnson CD, Fronczak FJ, et al. Postbiopsy bleeding in a porcine model: reduction with radio-frequency ablation--preliminary results. Radiology. 2003 May;227(2):493–9.

52. Gaynor SL, Byrd GD, Diodato MD, Ishii Y, Lee AM, Prasad SM, et al. Dose response curves for microwave ablation in the cardioplegia-arrested porcine heart. Heart Surg Forum. 2005;8(5):E331–6.

53. Rojas-Chapana JA, Correa-Duarte MA, Zhifeng R, Krysztof K, Giersig M. Enhanced Introduction of Gold Nanoparticles into Vital Acidothiobacillus ferrooxidans by Carbon Nanotube-based Microwave Electroporation. Nano Lett. 2004;4:985–8.

54. Ahmed M, Moussa M, Goldberg SN. Synergy in cancer treatment between liposomal chemotherapeutics and thermal ablation. Chem Phys Lipids. 2012 May;165(4):424–37.

55. Wallen CA, Michaelson SM. Proceedings: Microwave-induced hyperthermia as an adjuvant to cancer therapy. J Microw Power. 1976 Jun;11(2):175–6.

56. Brace CL. Microwave tissue ablation: biophysics, technology, and applications. Crit Rev Biomed Eng. 2010;38(1):65–78.

57. CarrafielloÃƒÂ G, LaganÃƒÂ D, Pellegrino C, Fontana F, Mangini M, Nicotera P, et al. Percutaneous imaging-guided ablation therapies in the treatment of symptomatic bone metastases: preliminary experience. Radiol Med. 2009 Jun;114(4):608–25.

58. Durick NA, Laeseke PF, Broderick LS, Lee FT Jr, Sampson LA, Frey TM, et al. Microwave ablation with triaxial antennas tuned for lung: results in an in vivo porcine model. Radiology. 2008 Apr;247(1):80–7.

59. Prakash P, Deng G, Converse MC, Webster JG, Mahvi DM, Ferris MC. Design optimization of a robust sleeve antenna for hepatic microwave ablation. Phys Med Biol. 2008 Feb 21;53(4):1057–69.

60. Dewey WC, Diederich CJ, Dewhirst MW. Hyperthermia classic commentary: “Arrhenius relationships from the molecule and cell to the clinic” by William Dewey, Int. J. Hyperthermia, 10:457-483, 1994. Int J Hyperth Off J Eur Soc Hyperthermic Oncol North Am Hyperth Group. 2009 Feb;25(1):21–4.

61. Berjano EJ. Theoretical modeling for radiofrequency ablation: state-of-the-art and challenges for the future. Biomed Eng Online. 2006;5:24.

62. Pennes HH. Temperature of skeletal muscle in cerebral hemiplegia and paralysis agitans. Arch Neurol Psychiatry. 1949 Oct;62(3):269–79.

63. Pearce JA. Relationship between Arrhenius models of thermal damage and the CEM 43 thermal dose. Int J Hyperthermia. 2009. p. 718104–718104–15.

64. Prakash P. Theoretical Modeling for Hepatic Microwave Ablation. Open Biomed Eng J. 2010 Feb 4;4:27–38.

65. Sapareto SA, Dewey WC. Thermal dose determination in cancer therapy. Int J Radiat Oncol Biol Phys. 1984 Jun;10(6):787–800.

66. Mertyna P, Goldberg W, Yang W, Goldberg SN. Thermal Ablation: A Comparison of Thermal Dose Required for Radiofrequency-, Microwave- and Laser-induced Coagulation in an Ex-vivo Bovine Liver Model. Acad Radiol. 2009 Dec;16(12):1539–48.

67. Xu Y, Qian R. Analysis of thermal injury process based on enzyme deactivation mechanisms. J Biomech Eng. 1995 Nov;117(4):462–5.

68. Feng Y, Oden JT, Rylander MN. A Two-State Cell Damage Model Under Hyperthermic Conditions: Theory and In Vitro Experiments. J Biomech Eng. 2008 Aug;130(4):041016.

69. Brace CL. Dual-slot antennas for microwave tissue heating: parametric design analysis and experimental validation. Med Phys. 2011 Jul;38(7):4232–40.

70. Cavagnaro M, Amabile C, Bernardi P, Pisa S, Tosoratti N. A Minimally Invasive Antenna for Microwave Ablation Therapies: Design, Performances, and Experimental Assessment. Biomed Eng IEEE Trans On. 2011 Apr;58(4):949 –959.

71. Longo I, Gentili GB, Cerretelli M, Tosoratti N. A coaxial antenna with miniaturized choke for minimally invasive interstitial heating. IEEE Trans Biomed Eng. 2003 Jan;50(1):82–8.

72. Hurter W, Reinbold F, Lorenz WJ. A dipole antenna for interstitial microwave hyperthermia. Microw Theory Tech IEEE Trans On. 1991 Jun;39(6):1048 –1054.

73. Schaller G, Erb J, Engelbrecht R. Field simulation of dipole antennas for interstitial microwave hyperthermia. Microw Theory Tech IEEE Trans On. 1996 Jun;44(6):887 –895.

74. Brace CL, van der Weide DW, Lee FT, Laeseke PF, Sampson L. Analysis and experimental validation of a triaxial antenna for microwave tumor ablation. IEEE MTT- Int Microw Symp Dig IEEE MTT- Int Microw Symp. 2004 Jun;3(6-11):1437–40.

75. Lubner MG, Brace CL, Hinshaw JL, Lee FT Jr. Microwave tumor ablation: mechanism of action, clinical results, and devices. J Vasc Interv Radiol JVIR. 2010 Aug;21(8 Suppl):S192–203.

76. Bakker JF, Paulides MM, Westra AH, Schippers H, Van Rhoon GC. Design and test of a 434 MHz multi-channel amplifier system for targeted hyperthermia applicators. Int J Hyperth. 2010;26(2):158–70.

77. Converse M, Bond EJ, Van Veen BD, Hagness SC. A computational study of ultra-wideband versus narrowband microwave hyperthermia for breast cancer treatment. IEEE Trans Microw Theory Tech. 2006;54:2169–80.

78. Jones RP, Kitteringham NR, Terlizzo M, Hancock C, Dunne D, Fenwick SW, et al. Microwave ablation of ex vivo human liver and colorectal liver metastases with a novel 14.5 GHz generator. Int J Hyperth Off J Eur Soc Hyperthermic Oncol North Am Hyperth Group. 2012;28(1):43–54.

79. Ryan TP, Turner PF, Hamilton B. Interstitial microwave transition from hyperthermia to ablation: historical perspectives and current trends in thermal therapy. Int J Hyperth Off J Eur Soc Hyperthermic Oncol North Am Hyperth Group. 2010;26(5):415–33.

80. Liu F-Y, Yu X-L, Liang P, Wang Y, Zhou P, Yu J. Comparison of percutaneous 915 MHz microwave ablation and 2450 MHz microwave ablation in large hepatocellular carcinoma. Int J Hyperth Off J Eur Soc Hyperthermic Oncol North Am Hyperth Group. 2010;26(5):448–55.

81. Sun Y, Wang Y, Ni X, Gao Y, Shao Q, Liu L, et al. Comparison of ablation zone between 915- and 2,450-MHz cooled-shaft microwave antenna: results in in vivo porcine livers. AJR Am J Roentgenol. 2009 Feb;192(2):511–4.

82. Henderson A, James JR. Near-field power transfer effects in small electromagnetic applicators for inducing hyperthermia. Microw Antennas Propag IEE Proc H. 1985 Jun;132(3):189 –197.

83. Brace CL, Laeseke PF, Sampson LA, Frey TM, van der Weide DW, Lee FT. Microwave Ablation with Multiple Simultaneously Powered Small-gauge Triaxial Antennas: Results from an in Vivo Swine Liver Model1. Radiology. 2007 Jul;244(1):151 –156.

84. Laeseke PF, Sampson LA, Lee FTJ, Brace CL. Multiple-antenna microwave ablation: Spatially distributing power improves thermal profiles and reduces invasiveness. J Interv Oncol. 2010;2(2):65–72.

85. Oshima F, Yamakado K, Nakatsuka A, Takaki H, Makita M, Takeda K. Simultaneous microwave ablation using multiple antennas in explanted bovine livers: relationship between ablative zone and antenna. Radiat Med. 2008;26(7):408–14.

86. Wright AS, Lee FTJ, Mahvi DM. Hepatic microwave ablation with multiple antennae results in synergistically larger zones of coagulation necrosis. Ann Surg Oncol. 2003 Apr;10(3):275–83.

87. Yu NC, Lu DSK, Raman SS, Dupuy DE, Simon CJ, Lassman C, et al. Hepatocellular carcinoma: microwave ablation with multiple straight and loop antenna clusters--pilot comparison with pathologic findings. Radiology. 2006 Apr;239(1):269–75.

88. Magin RL, Peterson AF. Noninvasive microwave phased arrays for local hyperthermia: a review. Int J Hyperth. 1989;5(4):429–50.

89. Turner PF. Interstitial equal-phased arrays for EM hyperthermia. IEEE Trans Microw Theory Tech. 1986;34:572–8.

90. Furse CM, Iskander MF. Three-dimensional electromagnetic power deposition in tumors using interstitial antenna arrays. IEEE Trans Biomed Eng. 1989;36(10):977–86.

91. Camart JC, Dubois L, Fabre JJ, Vanloot D, Chive M. 915 MHz microwave interstitial hyperthermia. Part II: Array of phase-monitored antennas. Int J Hyperth Off J Eur Soc Hyperthermic Oncol North Am Hyperth Group. 1993 Jun;9(3):445–54.

92. Trembly BS, Wilson AH, Sullivan MJ, Stein AD, Wong TZ, Strohbehn JW. Control of the SAR pattern withing an interstitial microwave array through variation of antenna driving phase. IEEE Trans Microw Theory Tech. 1986;34:568–71.

93. Clibbon KL, McCowen A. Efficient computation of SAR distributions from interstitial microwave antenna arrays. IEEE Trans Microw Theory Tech. 1994 Apr;42(4):595 –600.

94. Lin J, Hirai S, Chiang C-L, Hsu W-L, Su J-L, Wang Y-J. Computer Simulation and Experimental Studies of SAR Distributions of Interstitial Arrays of Sleeved-Slot Microwave Antennas for Hyperthermia Treatment of Brain Tumors. IEEE Trans Microw Theory Tech. 2000;48:2191–8.

95. Ryan TP, Trembly BS, Roberts DW, Strohbehn JW, Coughlin CT, Hoopes PJ. Brain hyperthermia: I. Interstitial microwave antenna array techniques--the Dartmouth experience. Int J Radiat Oncol Biol Phys. 1994 Jul;29(5):1065–78.

96. James BJ, Strohbehn JW, Mechling JA, Trembly BS. The effect of insertion depth on the theoretical SAR patterns of 915 MHz dipole antenna arrays for hyperthermia. Int J Hyperth Off J Eur Soc Hyperthermic Oncol North Am Hyperth Group. 1989 Dec;5(6):733–47.

97. Mechling JA, Strohbehn JW, France LJ. A theoretical evaluation of the performance of the Dartmouth IMAAH system to heat cylindrical and ellipsoidal tumour models. Int J Hyperth. 1991;7(3):465–83.

98. Stuchly SS, Eidus L, Swarup A, Surowiec. In vitro dielectric properties of human tissues at radiofrequencies. Phys Med Biol. 32(5):615–21.

99. Gabriel S, Lau RW, Gabriel C. The dielectric properties of biological tissues: III. Parametric models for the dielectric spectrum of tissues. Phys Med Biol. 1996;41:2271–93.

100. Schwan HP, Li K. Measurements of materials with high dielectric constant and conductivity at ultrahigh frequencies. AIEE Trans Comm Electron. 1955;74:603–7.

101. Schwan HP, Li K. Capacity and Conductivity of Body Tissues at Ultrahigh Frequencies. Proc IRE. 1953 Dec;41(12):1735 –1740.

102. Lazebnik M, Converse MC, Booske JH, Hagness SC. Ultrawideband temperature-dependent dielectric properties of animal liver tissue in the microwave frequency range. Phys Med Biol. 2006 Apr;51(7):1941–55.

103. Yang D, Converse MC, Mahvi DM, Webster JG. Expanding the bioheat equation to include tissue internal water evaporation during heating. IEEE Trans Biomed Eng. 2007;54(8):1382–8.

104. Schepps JL, Foster KR. The UHF and microwave dielectric properties of normal and tumors tissue: variation in dielectric properties with tissue water content. 1980;25(6):1149–59.

105. Bircan C, Barringer S. Determination of protein denaturation of muscle foods using the dielectric properties. J Food Sci. 2002;67:202–5.

106. Chin L, Sherar M. Changes in the dielectric properties of rat prostate ex vivo at 915 MHz during heating. Int J Hyperth. 2004;20(5):517–27.

107. Ji Z, Brace CL. Expanded modeling of temperature-dependent dielectric properties for microwave thermal ablation. Phys Med Biol. 2011 Aug 21;56(16):5249–64.

108. Lopresto V, Pinto R, Lovisolo GA, Cavagnaro M. Changes in the dielectric properties of ex vivo bovine liver during microwave thermal ablation at 2.45 GHz. Phys Med Biol. 2012 Apr 21;57(8):2309–27.

109. He X, McGee S, Coad JE, Schmidlin F, Iaizzo PA, Swanlund DJ, et al. Investigation of the thermal and tissue injury behaviour in microwave thermal therapy using a porcine kidney model. Int J Hyperth Off J Eur Soc Hyperthermic Oncol North Am Hyperth Group. 2004 Sep;20(6):567–93.

110. Wall MS, Deng XH, Torzilli PA, Doty SB, O'Brien SJ, Warren RF. Thermal modification of collagen. J Shoulder Elb Surg. 1999;8(4):339–44.

111. Ai H, Wu S, Gao H, Zhao L, Yang C, Zeng Y. Temperature distribution analysis of tissue water vaporization during microwave ablation: Experiments and simulations. Int J Hyperthermia. 2012 Nov;28(7):674–85.

112. Brace CL, Diaz TA, Hinshaw JL, Lee FT. Tissue contraction caused by radiofrequency and microwave ablation: a laboratory study in liver and lung. J Vasc Interv Radiol JVIR. 2010 Aug;21(8):1280–6.

113. Bhardwaj N, Dormer J, Ahmad F, Strickland AD, Gravante G, West K, et al. Microwave ablation of the liver: a description of lesion evolution over time and an investigation of the heat sink effect. Pathology (Phila). 2011 Dec;43(7):725–31.

114. Ahmad F, Gravante G, Bhardwaj N, Strickland A, Basit R, West K, et al. Changes in interleukin-1β and 6 after hepatic microwave tissue ablation compared with radiofrequency, cryotherapy and surgical resections. Am J Surg. 2010 Oct;200(4):500–6.

115. Chen MH, Yang W, Yan K, Dai Y, Wu W, Fan ZH, et al. The role of contrast-enhanced ultrasound in planning treatment protocols for hepatocellular carcinoma before radiofrequency ablation. Clin Radiol. 2007;62(8):752–60.

116. Cha CH, Lee FT Jr, Gurney JM, Markhardt BK, Warner TF, Kelcz F, et al. CT versus sonography for monitoring radiofrequency ablation in a porcine liver. AJR Am J Roentgenol. 2000 Sep;175(3):705–11.

117. Limanond P, Zimmerman P, Raman SS, Kadell BM, Lu DSK. Interpretation of CT and MRI after radiofrequency ablation of hepatic malignancies. AJR Am J Roentgenol. 2003 Dec;181(6):1635–40.

118. Terraz S, Cernicanu A, Lepetit-Coiffé M, Viallon M, Salomir R, Mentha G, et al. Radiofrequency ablation of small liver malignancies under magnetic resonance guidance: progress in targeting and preliminary observations with temperature monitoring. Eur Radiol. 2010 Apr;20(4):886–97.

119. Cernicanu A, Lepetit-Coiffe M, Viallon M, Terraz S, Becker CD. New horizons in MR-controlled and monitored radiofrequency ablation of liver tumours. Cancer Imaging. 2007 Nov 5;7(1):160–6.

120. Cernicanu A, Lepetit-Coiffe M, Roland J, Becker CD, Terraz S. Validation of fast MR thermometry at 1.5 T with gradient-echo echo planar imaging sequences: phantom and clinical feasibility studies. NMR Biomed. 2008 Oct;21(8):849–58.

121. Kurumi Y, Tani T, Naka S, Shiomi H, Shimizu T, Abe H, et al. MR-guided microwave ablation for malignancies. Int J Clin Oncol. 2007 Apr;12(2):85–93.

122. Morikawa S, Inubushi T, Kurumi Y, Naka S, Sato K, Tani T, et al. MR-guided microwave thermocoagulation therapy of liver tumors: initial clinical experiences using a 0.5 T open MR system. J Magn Reson Imaging. 2002;16(5):576–83.

123. Meloni MF, Andreano A, Bovo G, Chiarpotto B, Amabile C, Gelsomino S, et al. Acute Portal Venous Injury after Microwave Ablation in an in Vivo Porcine Model: A Rare Possible Complication. J Vasc Interv Radiol JVIR. 2011 May 6

124. Kröger T, Pätz T, Altrogge I, Schenk A, Lehmann KS, Frericks BB, et al. Fast Estimation of the Vascular Cooling in RFA Based on Numerical Simulation. Open Biomed Eng J. 2010;4:16–26.

125. Kröger T, Pannier S, Kaliske M, Altrogge I, Graf W, Preusser T. Optimal applicator placement in hepatic radiofrequency ablation on the basis of rare data. Comput Methods Biomech Biomed Engin. 2010 Jun;13(3):431–40.

126. Altrogge I, Preusser T, Kröger T, Büskens C, Pereira PL, Schmidt D, et al. Multiscale optimization of the probe placement for radiofrequency ablation. Acad Radiol. 2007 Nov;14(11):1310–24.

127. Haemmerich D, Wood BJ. Hepatic radiofrequency ablation at low frequencies preferentially heats tumour tissue. Int J Hyperth. 2006;22(7):563–74.

128. Consiglieri L, dos Santos I, Haemmerich D. Theoretical analysis of the heat convection coefficient in large vessels and the significance for thermal ablative therapies. Phys Med Biol. 2003 Dec 21;48(24):4125–34.

129. Schutt DJ, Haemmerich D. Effects of variation in perfusion rates and of perfusion models in computational models of radio frequency tumor ablation. Med Phys. 2008 Aug;35(8):3462–70.

130. Schramm W, Yang D, Haemmerich D. Contribution of direct heating, thermal conduction and perfusion during radiofrequency and microwave ablation. Conf Proc IEEE Eng Med Biol Soc. 2006;1:5013–6.

131. Chiang J, Hynes K, Brace CL. Flow-dependent vascular heat transfer during microwave thermal ablation. Conf Proc Annu Int Conf IEEE Eng Med Biol Soc IEEE Eng Med Biol Soc Conf. 2012;2012:5582–5.

132. Kojima Y, Suzuki S, Sakaguchi T, Tsuchiya Y, Okamoto K, Kurachi K, et al. Portal vein thrombosis caused by microwave coagulation therapy for hepatocellular carcinoma: report of a case. Surg Today. 2000;30(9):844–8.

133. O'Rourke AP, Haemmerich D, Prakash P, Converse MC, Mahvi DM, Webster JG. Current status of liver tumor ablation devices. Expert Rev Med Devices. 2007 Jul;4(4):523–37.

134. Yoo D-S. The dielectric properties of cancerous tissues in a nude mouse xenograft model. Bioelectromagnetics. 2004;25(7):492–7.

135. Seitel A, Engel M, Sommer CM, Radeleff BA, Essert-Villard C, Baegert C, et al. Computer-assisted trajectory planning for percutaneous needle insertions. Med Phys. 2011 Jun;38(6):3246–59.

136. Villard C, Baegert C, Schreck P, Soler L, Gangi A. Optimal trajectories computation within regions of interest for hepatic RFA planning. Med Image Comput Comput-Assist Interv MICCAI Int Conf Med Image Comput Comput-Assist Interv. 2005;8(Pt 2):49–56.

137. Baegert C, Villard C, Schreck P, Soler L. Multi-criteria trajectory planning for hepatic radiofrequency ablation. Med Image Comput Comput-Assist Interv MICCAI Int Conf Med Image Comput Comput-Assist Interv. 2007;10(Pt 2):676–84.

138. Rieder C, Kröger T, Schumann C, Hahn HK. GPU-based real-time approximation of the ablation zone for radiofrequency ablation. IEEE Trans Vis Comput Graph. 2011 Dec;17(12):1812–21.

139. Brace CL. Microwave tissue ablation: biophysics, technology, and applications. Crit Rev Biomed Eng. 2010;38(1):65–78.

140. Andreano A, Huang Y, Meloni MF, Lee FT, Brace C. Microwaves create larger ablations than radiofrequency when controlled for power in ex vivo tissue. Med Phys. 2010 Jun;37(6):2967–73.

141. Labonte S, Blais A, Legault SR, Ali HO, Roy L. Monopole antennas for microwave catheter ablation. Microw Theory Tech IEEE Trans On. 1996 Oct;44(10):1832 –1840.

142. Brace CL, Laeseke PF, van der Weide DW, Lee FT. Microwave Ablation With a Triaxial Antenna: Results in ex vivo Bovine Liver. IEEE Trans Microw Theory Tech. 2005 Jan;53(1):215–20.

143. Shock SA, Laeseke PF, Sampson LA, Lewis WD, Winter TC 3rd, Fine JP, et al. Hepatic hemorrhage caused by percutaneous tumor ablation: radiofrequency ablation versus cryoablation in a porcine model. Radiology. 2005 Jul;236(1):125–31.

144. Bertram JM, Yang D, Converse MC, Webster JG, Mahvi DM. Antenna design for microwave hepatic ablation using an axisymmetric electromagnetic model. Biomed Eng Online. 2006;5.

145. Yang D, Bertram JM, Converse MC, O'Rourke AP, Webster JG, Hagness SC, et al. A floating sleeve antenna yields localized hepatic microwave ablation. IEEE Trans Biomed Eng. 2006 Mar;53(3):533–7.

146. Geraghty PR, Kee ST, McFarlane G, Razavi MK, Sze DY, Dake MD. CT-guided transthoracic needle aspiration biopsy of pulmonary nodules: needle size and pneumothorax rate. Radiology. 2003 Nov;229(2):475–81.

147. Brace CL. Dual-slot antennas for microwave tissue heating: Parametric analysis and experimental validation. Med Phys. 2011 Jul;38(7):4232–40.

148. Wong R, Frenette C. Updates in the management of hepatocellular carcinoma. Gastroenterol Hepatol. 2011 Jan;7(1):16–24.

149. Abu-Hilal M, Primrose JN, Casaril A, McPhail MJW, Pearce NW, Nicoli N. Surgical resection versus radiofrequency ablation in the treatment of small unifocal hepatocellular carcinoma. J Gastrointest Surg Off J Soc Surg Aliment Tract. 2008 Sep;12(9):1521–6.

150. Ayav A, Germain A, Marchal F, Tierris I, Laurent V, Bazin C, et al. Radiofrequency ablation of unresectable liver tumors: factors associated with incomplete ablation or local recurrence. Am J Surg. 2010 Oct;200(4):435–9.

151. Brace CL. Microwave ablation technology: what every user should know. Curr Probl Diagn Radiol. 2009 Apr;38(2):61–7.

152. Bertram JM, Yang D, Converse MC, Webster JG, Mahvi DM. A review of coaxial-based interstitial antennas for hepatic microwave ablation. Crit Rev Biomed Eng. 2006;34(3):187–213.

153. Deardorff DL, Diederich CJ, Nau WH. Control of interstitial thermal coagulation: comparative evaluation of microwave and ultrasound applicators. Med Phys. 2001 Jan;28(1):104–17.

154. Dong BW, Liang P, Yu XL, Zeng XQ, Wang PJ, Su L, et al. Sonographically guided microwave coagulation treatment of liver cancer: an experimental and clinical study. AJR Am J Roentgenol. 1998 Aug;171(2):449–54.

155. Liang P, Wang Y. Microwave ablation of hepatocellular carcinoma. Oncology. 2007;72 Suppl 1:124–31.

156. Knavel EM, Hinshaw JL, Lubner MG, Andreano A, Warner TF, Lee FT Jr, et al. High-powered gas-cooled microwave ablation: shaft cooling creates an effective stick function without altering the ablation zone. AJR Am J Roentgenol. 2012 Mar;198(3):W260–265.

157. Cavagnaro M, Amabile C, Bernardi P, Pisa S, Tosoratti N. A minimally invasive antenna for microwave ablation therapies: design, performances, and experimental assessment. IEEE Trans Biomed Eng. 2010 Dec 17

158. Hines-Peralta AU, Pirani N, Clegg P, Cronin N, Ryan TP, Liu Z, et al. Microwave ablation: results with a 2.45-GHz applicator in ex vivo bovine and in vivo porcine liver. Radiology. 2006 Apr;239(1):94–102.

159. Committee for the Update of the Guide for the Care and Use of Laboratory Animals; National Research Council. Guide for the Care and Use of Laboratory Animals: Eighth Edition. Washington, D.C.: The National Academies Press; 2010.

160. Coad JE, Kosari K, Humar A, Sielaff TD. Radiofrequency ablation causes “thermal fixation” of hepatocellular carcinoma: a post-liver transplant histopathologic study. Clin Transplant. 2003 Aug;17(4):377–84.

161. Zhou Q, Jin X, Jiao D-C, Zhang F-J, Zhang L, Han X-W, et al. Microwave ablation: results in ex vivo and in vivo porcine livers with 2450-MHz cooled-shaft antenna. Chin Med J (Engl). 2011 Oct;124(20):3386–93.

162. Pisa S, Cavagnaro M, Bernardi P, Lin JC. A 915-MHz antenna for microwave thermal ablation treatment: physical design, computer modeling and experimental measurement. IEEE Trans Biomed Eng. 2001 May;48(5):599–601.

163. Brace CL, Hinshaw JL, Lubner MG. Thermal ablation for the treatment of abdominal tumors. J Vis Exp JoVE. 2011 ;(49).

164. Lu DSK, Raman SS, Vodopich DJ, Wang M, Sayre J, Lassman C. Effect of vessel size on creation of hepatic radiofrequency lesions in pigs: assessment of the “heat sink” effect. AJR Am J Roentgenol. 2002 Jan;178(1):47–51.

165. Determinants of Blood Viscosity. Acta Med Scand. 1966;180(S456):14–6.

166. Késmárky G, Kenyeres P, Rábai M, Tóth K. Plasma viscosity: a forgotten variable. Clin Hemorheol Microcirc. 2008;39(1-4):243–6.

167. Patterson EJ, Scudamore CH, Owen DA, Nagy AG, Buczkowski AK. Radiofrequency ablation of porcine liver in vivo: effects of blood flow and treatment time on lesion size. Ann Surg. 1998 Apr;227(4):559–65.

168. Eckmann DM, Bowers S, Stecker M, Cheung AT. Hematocrit, Volume Expander, Temperature, and Shear Rate Effects on Blood Viscosity. Anesth Analg. 2000 Sep 1;91(3):539–45.

169. De Baere T. Radiofrequency ablation of the liver. AJR Am J Roentgenol. 2001;177(5):1213–5.

170. Bonastre J, De Baere T, Elias D, Evrard S, Rouanet P, Bazin C, et al. Cost of radiofrequency ablation in the treatment of hepatic malignancies. Gastroenterol Clin Biol. 2007;31(10):828–35.

171. Peng Z-W, Liu F-R, Ye S, Xu L, Zhang Y-J, Liang H-H, et al. Radiofrequency ablation versus open hepatic resection for elderly patients (> 65 years) with very early or early hepatocellular carcinoma. Cancer. 2013 Nov 1;119(21):3812-20.

172. Pompili M, Saviano A, de Matthaeis N, Cucchetti A, Ardito F, Federico B, et al. Long-term effectiveness of resection and radiofrequency ablation for single hepatocellular carcinoma ≤3 cm. Results of a multicenter Italian survey. J Hepatol. 2013 Jul;59(1):89–97.

173. Alexander ES, Machan JT, Ng T, Breen LD, DiPetrillo TA, Dupuy DE. Cost and effectiveness of radiofrequency ablation versus limited surgical resection for stage I non-small-cell lung cancer in elderly patients: is less more? J Vasc Interv Radiol JVIR. 2013 Apr;24(4):476–82.

174. Lu DSK, Raman SS, Vodopich DJ, Wang M, Sayre J, Lassman C. Effect of Vessel Size on Creation of Hepatic Radiofrequency Lesions in Pigs: Assessment of the "Heat Sink" Effect. Am J Roentgenol. 2002 Jan 1;178(1):47–51.

175. Nakazawa T, Kokubu S, Shibuya A, Ono K, Watanabe M, Hidaka H, et al. Radiofrequency ablation of hepatocellular carcinoma: correlation between local tumor progression after ablation and ablative margin. AJR Am J Roentgenol. 2007 Feb;188(2):480–8.

176. Liu C-H, Arellano RS, Uppot RN, Samir AE, Gervais DA, Mueller PR. Radiofrequency ablation of hepatic tumours: effect of post-ablation margin on local tumour progression. Eur Radiol. 2010 Apr;20(4):877–85.

177. Dos Santos I, Haemmerich D, Pinheiro C, da Rocha A. Effect of variable heat transfer coefficient on tissue temperature next to a large vessel during radiofrequency tumor ablation. Biomed Eng OnLine. 2008;7(1):21.

178. Haemmerich D, Wright AW, Mahvi DM, Lee FT Jr, Webster JG. Hepatic bipolar radiofrequency ablation creates coagulation zones close to blood vessels: a finite element study. Med Biol Eng Comput. 2003 May;41(3):317–23.

179. Ahmed M, Liu Z, Humphries S, Nahum Goldberg S. Computer modeling of the combined effects of perfusion, electrical conductivity, and thermal conductivity on tissue heating patterns in radiofrequency tumor ablation. Int J Hyperthermia. 2008 Jan;24(7):577–88.

180. Wright AS, Sampson LA, Warner TF, Mahvi DM, Lee FTJ. Radiofrequency versus microwave ablation in a hepatic porcine model. Radiology. 2005 Jul;236(1):132–9.

181. Andreano A, Brace CL. A Comparison of Direct Heating During Radiofrequency and Microwave Ablation in Ex Vivo Liver. Cardiovasc Intervent Radiol. 2013 Apr;36(2):505-11.

182. Carrafiello G, Mangini M, Fontana F, Di Massa A, Ierardi AM, Cotta E, et al. Complications of microwave and radiofrequency lung ablation: personal experience and review of the literature. Radiol Med (Torino). 2012 Mar;117(2):201–13.

183. Swan RZ, Sindram D, Martinie JB, Iannitti DA. Operative microwave ablation for hepatocellular carcinoma: complications, recurrence, and long-term outcomes. J Gastrointest Surg Off J Soc Surg Aliment Tract. 2013 Apr;17(4):719–29.

184. Meloni MF, Andreano A, Lava M, Lazzaroni S, Okolicsanyi S, Sironi S. Segmental portal vein thrombosis after microwave ablation of liver tumors: Report of two cases. Eur J Radiol Extra. 2010 Dec;76(3):e95–e98.

185. DeLong ER, DeLong DM, Clarke-Pearson DL. Comparing the areas under two or more correlated receiver operating characteristic curves: a nonparametric approach. Biometrics. 1988 Sep;44(3):837–45.

186. Kim JH, Yim HJ, Lee KG, Kim SY, Jung ES, Jung YK, et al. Recurrence rates and factors for recurrence after radiofrequency ablation combined with transarterial chemoembolization for hepatocellular carcinoma: a retrospective cohort study. Hepatol Int. 2012 April; 6(2):505-510

187. Di Vece F, Tombesi P, Ermili F, Maraldi C, Sartori S. Coagulation Areas Produced by Cool-Tip Radiofrequency Ablation and Microwave Ablation Using a Device to Decrease Back-Heating Effects: A Prospective Pilot Study. Cardiovasc Intervent Radiol. 2013 Oct 3;

188. Kim AY, Rhim H, Park M, Lee MW, Kim Y-S, Choi D, et al. Venous thrombosis after radiofrequency ablation for hepatocellular carcinoma. AJR Am J Roentgenol. 2011 Dec;197(6):1474–80.

189. Frericks BB, Ritz JP, Albrecht T, Valdeig S, Schenk A, Wolf K-J, et al. Influence of intrahepatic vessels on volume and shape of percutaneous thermal ablation zones: in vivo evaluation in a porcine model. Invest Radiol. 2008 Apr;43(4):211–8.

190. Mohamed AlAmiri A. Fluid-Structure Interaction Analysis of Pulsatile Blood Flow and Heat Transfer in Living Tissues During Thermal Therapy. J Fluids Eng. 2013 Mar 21;135(4):041103–041103.

191. Persoons T, Saenen T, Donose R, Baelmans M. Heat transfer enhancement due to pulsating flow in a microchannel heat sink. 15th International Workshop on Thermal Investigations of ICs and Systems, 2009 THERMINIC 2009. 2009. p. 163–7.

192. Feng K, Yan J, Li X, Xia F, Ma K, Wang S, et al. A randomized controlled trial of radiofrequency ablation and surgical resection in the treatment of small hepatocellular carcinoma. J Hepatol. 2012 Oct;57(4):794–802.

193. Naugler WE, Sonnenberg A. Survival and cost-effectiveness analysis of competing strategies in the management of small hepatocellular carcinoma. Liver Transplant Off Publ Am Assoc Study Liver Dis Int Liver Transplant Soc. 2010 Oct;16(10):1186–94.

194. Wachsberg RH, Angyal EA, Klein KM, Kuo HR, Lambert WC. Echogenicity of hepatic versus portal vein walls revisited with histologic correlation. J Ultrasound Med. 1997 Dec 1;16(12):807–10.

195. Ikeda Y, Handa M, Kawano K, Kamata T, Murata M, Araki Y, et al. The role of von Willebrand factor and fibrinogen in platelet aggregation under varying shear stress. J Clin Invest. 1991 Apr;87(4):1234–40.

196. Grabowski EF, Reininger AJ, Petteruti PG, Tsukurov O, Orkin RW. Shear stress decreases endothelial cell tissue factor activity by augmenting secretion of tissue factor pathway inhibitor. Arterioscler Thromb Vasc Biol. 2001 Jan;21(1):157–62.

197. Gomes N, Legrand C, Lafeve FF-. Shear Stress Induced Release of Von Willebrand Factor and Thrombospondin-1 in Uvec Extracellular Matrix Enhances Breast Tumour Cell Adhesion. Clin Exp Metastasis. 2005 May 1;22(3):215–23.

198. Ahmed M, Moussa M, Goldberg SN. Synergy in cancer treatment between liposomal chemotherapeutics and thermal ablation. Chem Phys Lipids. 2012 May;165(4):424–37.

199. Cha CH, Lee FT Jr, Gurney JM, Markhardt BK, Warner TF, Kelcz F, et al. CT versus sonography for monitoring radiofrequency ablation in a porcine liver. AJR Am J Roentgenol. 2000 Oct;175(3):705–11.

200. Halder A, Datta AK. Surface heat and mass transfer coefficients for multiphase porous media transport models with rapid evaporation. Food Bioprod Process. 2012 Jul;90(3):475–90.

201. Peng Wang, Converse MC, Webster JG, Mahvi DM. “Improved” Calculation of Reflection Coefficient for Coaxial Antennas With Feed Gap Effect. Antennas Propag IEEE Trans On. 2009;57(2):559–63.

202. Welti-Chanes J, Velez-Ruiz JF. Transport Phenomena in Food Processing. CRC Press; 2010.

203. Gülüm Sumnu AKD. Transport and related properties of breads baked using various heating modes. J Food Eng. (4):1382–7.

204. Ratti C, Crapiste G h., Rotstein E. A New Water Sorption Equilibrium Expression for Solid Foods based on Thermodynamic Considerations. J Food Sci. 1989;54(3):738–42.

205. A Halder AD. An Improved, Easily Implementable, Porous Media Based Model for Deep-Fat Frying. Food Bioprod Process. 2007;85(3):220–30.

206. Zhou W, Liang M, Pan H, Liu X, Jiang Y, Wang Y, et al. Comparison of Ablation Zones among Different Tissues Using 2450-MHz Cooled-Shaft Microwave Antenna: Results in Ex Vivo Porcine Models. PLoS ONE. 2013 Aug 12 ;8(8).

207. Boukouvalas CJ, Krokida MK, Maroulis ZB, Marinos-Kouris D. Density and Porosity: Literature Data Compilation for Foodstuffs. Int J Food Prop. 2006;9(4):715–46.

208. Jaccard P. The Distribution of the Flora in the Alpine Zone.1. New Phytol. 1912;11(2):37–50.

209. Chiang J, Hynes KA, Bedoya M, Brace CL. A Dual-Slot Microwave Antenna for More Spherical Ablation Zones: Ex Vivo and in Vivo Validation. Radiology. 2013 Aug; 268(2):382-9.

210. Chiang J, Wang P, Brace CL. Computational modelling of microwave tumour ablations. Int J Hyperth Off J Eur Soc Hyperthermic Oncol North Am Hyperth Group. 2013 Jun;29(4):308–17.